HUNGARIAN GEOPHYSICAL INSTITUTE 'ROLAND EÖTVÖS'
MAGYAR ÁLLAMI EÖTVÖS LORÁND GEOFIZIKAI INTÉZET
ВЕНГЕРСКИЙ ГЕОФИЗИЧЕСКИЙ ИНСТИТУТ ИМ. Л. ЭТВЭША

GEOPHYSICAL TRANSACTIONS
GEOFIZIKAI KÖZLEMÉNYEK
ГЕОФИЗИЧЕСКИЙ БЮЛЛЕТЕНЬ

25

BUDAPEST, 1979

ETO/UDC 550.3(061.6) (439 Budapest) (058)
ISSN 0016–7177

Felelős kiadó: **MÜLLER** PÁL
Technikai szerkesztő: **NAGY** MAGDOLNA
Grafikai szerkesztő: **NÉMETH** LAJOS

Főprint nyomda 78273

CONTENTS

Pintér, A.–Stomfai, R.: Gravitational model calculations 5
Varga, P.: Connection between the inner structure and the static deformation of the Earth caused by external forces 31
Zsellér, P.: Determination of layer pressures using interval velocities 39
Korvin, G.: Some notes on a problem of Treitel and Wang 53
Erkel, A.–Simon, P.–Verő, L.: Measurement and interpretation of the dynamic characteristics of induced polarization decay curves 61
Andrássy, L.: Methodological basis of a ϱ processor for the direct determination of densities in bore-holes 73

TARTALOM

Pintér Anna–Stomfai Róbert: Gravitációs modellszámítások 5
Varga Péter: A Föld külső erők okozta statikus deformációinak kapcsolata a földszerkezettel 31
Zsellér Péter: Rétegnyomás-meghatározás intervallum sebességek felhasználásával ... 39
Korvin Gábor: Megjegyzések Treitel és Wang egy problémájáról 53
Erkel András–Simon Pál–Verő László: Gerjesztett potenciál lecsengési görbék dinamikus jellemzőinek mérése és értelmezése 61
Andrássy László: „ϱ" processzor módszertani alapjai a térfogatsúlyérték fúrólyukban történő közvetlen meghatározására 73

СОДЕРЖАНИЕ

А. Пинтер–Р. Штомфаи: Моделирование для интерпретации аномалий поля силы тяжести 5
П. Варга: Связь статических деформаций Земли, вызываемых внешними силами, с строением Земли 31
П. Желлер: Определение пластового давления с использованием интервальных скоростей 39
Г. Корвин: Замечания к одной из проблем Треителя и Ванга 53
А. Эркел–П. Шимон–Л. Верǫ: Получение и интерпретация динамических характеристик кривых затухания возбужденной поляризации 61
Л. Андраши: Методические основы процессора «ϱ» для прямого определения объемного веса в скважинах 73

Magyar Állami Eötvös Loránd Geofizikai Intézet
GEOFIZIKAI KÖZLEMÉNYEK
25

GRAVITATIONAL MODEL CALCULATIONS

A. PINTÉR*–R. STOMFAI*

1. Introduction

The terms "regional" and "residual anomalies" are as old as gravimetry itself. Following the classical works of Peters et al. in the late 1940'es and 1950'es, the computation and interpretation of the anomalies of the *vertical derivative* have also become widespread. In present-day practice it is customary to denote the derivatives and the results of low-cut filtering as residual anomalies as well. Some authors prefer the term *filtered anomaly*, obtained by low-cut or high-cut filters. Filtered or derivated anomalies are sometimes referred to as *transformed anomalies*. The same term can also be used for a downward or upward continued anomaly map, or to a contour map, if it had been derived from a gravity anomaly map.

The term *filtered anomaly* will only refer, in what follows, to the particular computation by which the anomaly map had been constructed. It does not express the character of the map or its geological meaning.

Generally, any practiced interpreter can tell, whether a certain map—obtained by some low-cut filter matrix—is more similar to a residual or to a derivative anomaly map. Otherwise, there is not too much chance to give any meaningful geological interpretation to the map.

Residual anomalies have clear-cut geological meaning. If a slowly changing gravitational effect exists, which distorts the gravity field of the body explored it can be eliminated by an appropriate low-cut filter. The result will be, at least theoretically, a residual anomaly map. In reality, of course, the residual anomalies (their shape and magnitude) strongly depend on the particular procedures by which they have been determined.

If there is a significant difference between the dimensions of the explored body and that of the regional one, i.e. if there is a visible *frequency* difference between their effects on the Bouguer anomaly map, then their separation is in principle unambiguous. Otherwise, the separation of the two effects is uncertain; i.e. we either "cut off" some of the effects of the explored body or we spare some distortions from the regional effect.

Any kind of formal separation can be performed by filter-matrices, to separate a Bouguer anomaly map to *formal* regional and *formal* residual anomalies. There are no exact rules for the selection of the filter parameters, they only depend on the experience of the interpreting geophysicist.

Vertical-derivative-like anomaly maps do not have such clear-cut geological meaning as the residual maps, even though they reveal much more about the shape of the body

* Hungarian Geophysical Institute 'Roland Eötvös', Budapest
Manuscript received 13. 5. 1978

to an experienced interpreter than a Bouguer anomaly map. As a rule, vertical-derivative-like anomaly maps are rather complex, many times they have to undergo further transformations to be applicable for geological interpretation.

It will be illustrated by a series of model-experiments that the anomaly maps transformed by the low-cut filter-matrices of MESKÓ (1965, 1966) frequently become vertical-derivative-like, at least for grid-sizes applied in field practice. It will also be shown that there exists a suitable linear combination of the Bouguer- and vertical-derivative-like anomalies which approximates sufficiently well the shape of the body (PINTÉR and STOMFAI, 1974). If independent auxiliary depth data (from bore-holes, seismics etc.) are available, a realistic contour map of the basement can be obtained by such a procedure.

2. Gravitational Model Calculations—Basic Ideas

Let us compute the gravity effect Δg and its vertical derivatives of a *two-dimensional* body, and—starting out from these Δg values—the anomalies $m(s, \varkappa)$ calculated by means of the low-cut filters of MESKÓ. Grid-size s and the parameter $\varkappa$ is continously changed (Fig. 1.). (Here s denotes sampling distance, $\varkappa$ is a constant characterizing the fall-off of the weight function of the filter, $m(s, \varkappa)$ refers to anomalies obtained by low-cut filters.)

The effect of the polyhedral two-dimensional body shown in Fig. 1 can be obtained as a sum of the effects of faults. Since the effect of a single fault can be described by an analytical formula, the same holds true for their sum (or difference). So, we can compute by a single program the Δg, g_z, g_{zz} values on the surface along arbitrarily densely spaced grid-points (at every 1 m, e.g.).

Low-cut filtering of the Δg curve has been performed by the matrices $m(s, \varkappa)$, by letting s assume values from 25 m to 300 m, and for any given s taking $\varkappa = 3$, 4 and 6. (In practice the MESKÓ filters with $\varkappa = 3$, 4 and 6 proved to be the most efficient.)

It can be observed on Fig. 1 that (for any $\varkappa$) the transformed anomalies gradually become first-, then second-vertical-derivative-like, as s decreases. Extrapolating what has been observed on the Figure we can state that for increasing values of s the regional anomalies approach a straight line, i.e. a constant value. If the value of s, that is to say the size of the matrix, is too large compared to the dimensions of the anomalies, the regional anomaly reduces to a single average constant, while the residual anomaly will be equal to the Δg map minus this constant. By gradually changing (decreasing or increasing) the parameter s, we can obtain any possible transition between the Δg anomaly and the second-vertical-derivative-like anomaly.

Another interesting fact which is evident on the Figure is that the depth of the anomalous body is related to the Δg curve, while the changes of its shape are more evident on the vertical-derivative- (first of all the second-vertical-derivative)- like curves.

It can also be observed that for derivative-like anomalies (i.e. for sufficiently small values of s) the variation of $\varkappa$ influences first of all the amplitudes of the resulting curves, the locations of their zero lines and extreme values do not change.

The presented model is, of course, an oversimplification of the actual geological conditions: the body itself had been assumed two-dimensional, the density contrast between the anomalous body and the overlying medium was a constant $\Delta\sigma = 0.4$ g/cm^3 and any disturbing effects due to other, regional or local bodies had been neglected.

To approach the more complicated conditions as our next step the Δg, g_z, g_{zz} and $m(s, \varkappa)$ values, corresponding to 3-dimensional bodies of arbitrary shape were computed.

Density contrast $\Delta\sigma$ was kept constant, as above, and regional or local disturbing effects were neglected.

The main difficulty in this task is that the Δg, g_z, or g_{zz} effects due to three-dimensional bodies of an arbitrary shape cannot be expressed analytically. Such bodies must be

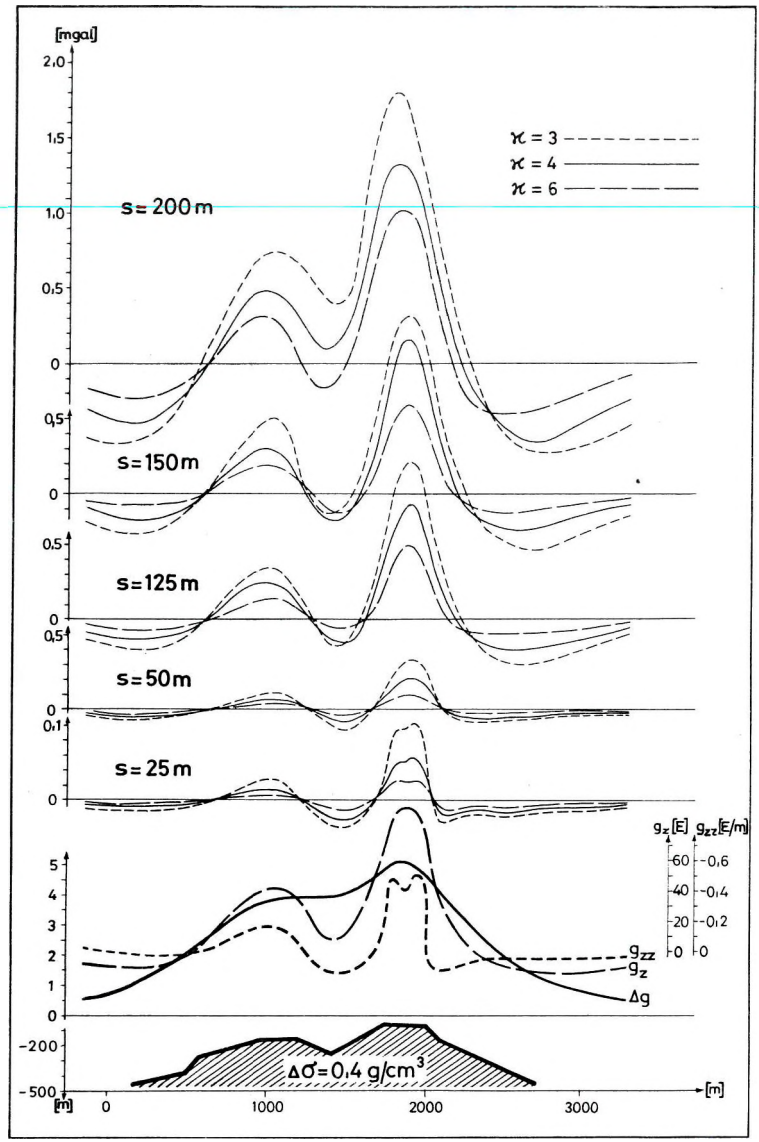

Fig. 1 Δg, g_z, g_{zz} and $m(s, \varkappa)$ anomalies due to a two-dimensional model

1. ábra. Kétdimenziós modell Δg, g_z, g_{zz} és $m(s, \varkappa)$ anomáliái

Рис. 1. Аномалии Δg, g_z, g_{zz}, и m (s, k), вызванные двумерной моделью

dissected to appropriate elementary parts of simple geometry, and the effects of these elementary mass-units should be summed at the points of the plane representing the surface. The computation is the more accurate, the smaller the gridsize on the surface and the more distant mass-units are taken into account in the sums. The computational facilities, of course, set a natural limit to the over-refinement of the calculations. We hope, however, that the results to be presented will still be applicable in practice.

Depth contours of the three-dimensional model were read out along the points of a grid of size s. Parameter s has been kept fixed throughout the experiments. It would have been easy, of course, to use larger s-values, by simply leaving out some of the samples, but since we have not been concerned with the filtering out of regional effects, this had no geophysical meaning. On the other hand, an s value smaller than by which the depth contours had been sampled could only have been obtained by formal interpolation.

In the model experiments the shape and depth of the anomalous body were changed within rather wide limits, while—as already mentioned—s was kept unchanged. For each model we computed the corresponding Δg, g_z, g_{zz} effects and the transformed anomalies $m(3)$, $m(4)$, $m(6)$ obtained by the respective low-cut type filter-matrices ($s = \text{const}$, $\varkappa = 3$, $\varkappa = 4$ and $\varkappa = 6$).

Naturally, the computed Δg values correspond to the usual Bouguer anomaly maps, while the $m(s, \varkappa)$ anomalies to the transformed anomalies obtained by low-cut filters from the Bouguer-anomaly map.

As well known, the quantities g_z, g_{zz} can not be directly measured in practice. The model experiments, however, will reveal the interconnection between the g_z and g_{zz} values and the anomalies $m(s, \varkappa)$.

We have already seen that the Δg curves—exempted from regional effects—are related to the depth of the anomalous body, while the characteristic variations of the shape of this body is reflected by the vertical-derivative-like (first of all, second-vertical-derivative-like) anomalies. On the basis of this idea a new interpretation method was elaborated to unite the informations contained in these anomaly maps about the depth and topography of the anomalous bodies. The gist of the method is to find a linear combination of the different anomaly maps by appropriately chosen weight factors so that the resulting map should as closely approximate the relief of the anomalous body as possible. As auxiliary conditions for the determination of the weight factors seismic (or any other, independent) depth data are used. In our practice this interpretation method has been termed in the last few years *optimized depth calculation.*

3. Gravitational Model Calculations—Details

Fig. 2 presents a vertical cross-section of the three-dimensional body used in the model. From the horizontal surface down to the boundary of the body there is an homogeneous medium of density σ_1. The body itself is also homogeneous of density σ_2, and $\sigma_2 > \sigma_1$. Since there are no vertical faults or overthrusts on the upper boundary of the body, its depth is a continuous and unique function of the surface coordinates.

The horizontal dimensions of the model were taken as 80×80 km. The relief of the model, i.e. its upper boundary had been represented by depth contour-lines of 10 m steps, and these depth values were sampled along the points of a rectangular grid of 500×500 m size. The accuracy of depth determination is about ± 10 m, even at steeper parts of the model.

The gravitational anomalies due to the model were determined for three different

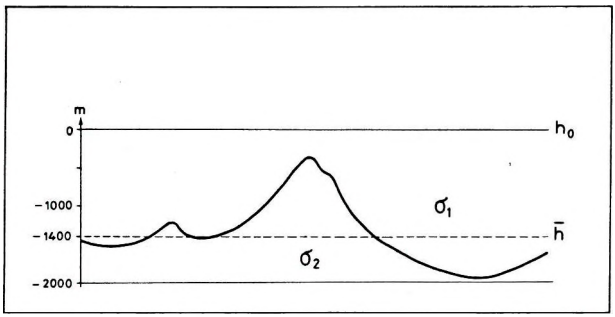

Fig. 2 A vertical cross section of the three-dimensional Model **A**
2. ábra. A háromdimenziós **A** modell egy függőleges metszete
Рис. 2. Вертикальное поперечное сечение трехмерной модели **A**

cases. First (Model **A**, Fig. 2) the deepest point on the body's boundary was 2000 m, its average depth 1400 m. Model **B** was placed deeper by 2000 m. Next, as it seemed rather arbitrary that the peaks of the model were steeper than its troughs, the mirror image of the basement of Model **A** was taken related to the horizontal plane at 1400 m depth, and used this as Model **C**.

To compute the Δg anomalies at the surface due to the respective models, numerical integration had to be used. The mass units of the numerical integration were vertical prisms of cross-section a^2 and density σ. The mass contained in such a prism was supposed to be compressed to a vertical *thread* and, the effects due to these *material threads* or *sticks* have been summarized. There is a very simple formula for the gravitational effect of such a stick:

$$\Delta g = \frac{f\sigma a^2}{r} \tag{1}$$

where r is the distance of the uppermost point of the stick from the point where the effect is observed. Since in numerical integration the effect of neighbourhood within 5000 m has been taken into account, the Δg values were computed over an area of 70×70 km^2.

By using vertical sticks as mass units the vertical derivatives of the field strength are given by:

$$g_z = f\sigma a^2 \frac{h}{r^3} \tag{2}$$

$$g_{zz} = f\sigma a^2 \left(3\frac{h^2}{r^2} - 1\right)\frac{1}{r^3} \tag{3}$$

where h is the depth of the mass unit, σ is its density. (In our computations this density was 0.1 g/cm^3.)

The experiments were performed with bodies of different depths. The anomalous body, e.g. of Fig. 2, extends from an upper boundary of variable depth down to a plane at a constant depth of 2000 m. It would be straight-forward to use variable-length mass elements for the computations, starting from the upper, and reaching down to the lower boundary. From the computational point of view, however, it is much more simple to use stick-like mass elements reaching down to infinite depths. This way, of course, a constant term is added to the computed effect at each point, which should be subtracted from the final results.

At the first stage of the model experiments, however, when we were mainly concerned with the connection between gravitational and depth data, we were only interested in the *relative* variation of the gravitational quantities from point to point, i.e. addition or subtraction of a constant term had no meaning whatever. Further, we did always assign rigorous dimensions to the computed physical quantities (plotted on maps of Fig. 4), but these dimensions have no relevance in the interpretation.

When we want to determine the relationship between depth and the gravitational quantities, we will simply deal with linear combinations of different sets of numerical values and will not keep in mind the physical dimensions of these numbers. The weight factors of linear combinations have dimensions of their own, but these are not even marked as only their numerical values have any relevance.

The maps used for the model experiments cover an area of 80×80 km^2, and are consisting of 160×160 points along a rectangular grid. But Δg values could be computed for 140×140 points only (a 10 points wide rim is cut off). After filtering a further 10 points wide rim falls off, i.e. the filtered maps will consist of 120×120 points. The contour map of this latter area is shown in Fig. 3. It is divided into 4×4 equal squares and further experiments will be performed on these 16 maps, each consisting of 30×30 points. Derivatives have only been computed for these 16 sub-areas. A series of maps referring to the same sub-area is shown in Fig. 4/1–4/11.*

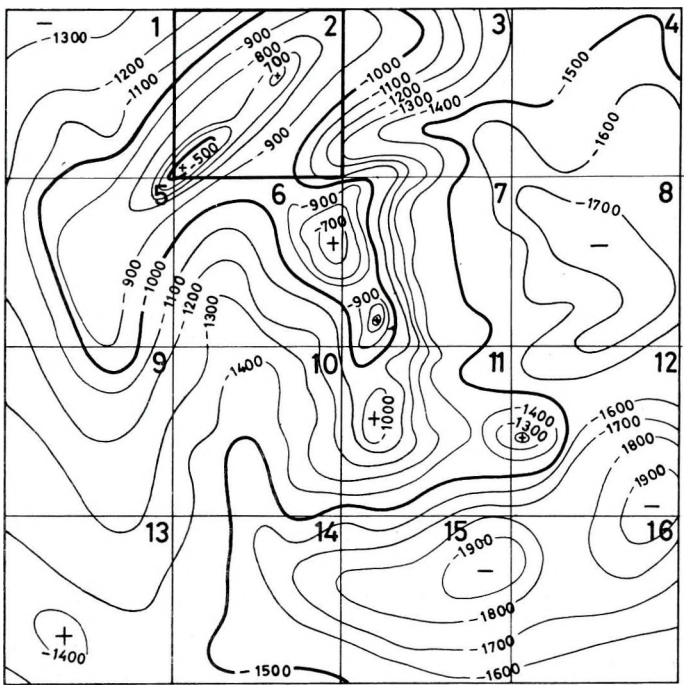

Fig. 3 Contour-map of Model **A**, with the 16 sub-areas
3. ábra. Az **A** modell domborzati térképe
Рис. 3. Карта изолиний для модели **A** с 16 участками

* Figs. 4/1–4/11 are to be found in the folder of the back cover

To understand the basic ideas of optimized depth calculations let us recall two-dimensional gravity calculations (along a profile).

Suppose, e.g., that there is a fault in the deeper, high density material. Fig. 5 shows the Δg anomaly above the fault, together with the anomaly-curve m obtained by low-cut filtering.

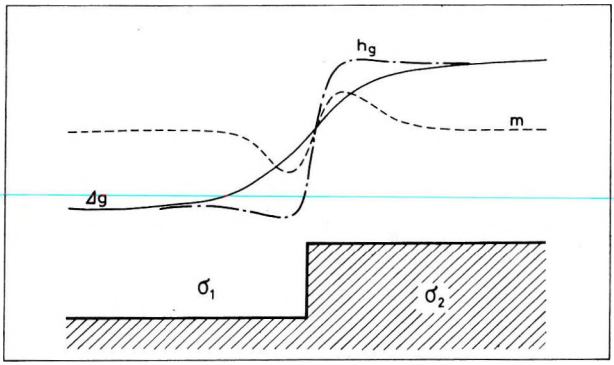

Fig. 5 Illustration of the *optimization principle*
5. ábra. Az „optimalizációs" kísérlet szemléltetése
Рис. 5. Иллюстрация принципа оптимации

the Δg anomaly above the fault, together with the anomalycurve m obtained by low-cut filtering.

The Δg curve smoothes out the exact location of the fault but gives indication of its height. On the other hand, the filtered curve m reflects fairly well its exact location but does not tell too much about the height of the fault. It is an evident idea to try to construct a new curve from these two, which would better indicate the fault than either the Δg or the filtered m curve. By approximating the (exact) depth curve h_g by a linear combination:

$$h_g \approx k_g \Delta g + k_m m \tag{4}$$

there exists a pair of coefficients k_g, k_m for which this approximation is optimal. To compute these coefficients, we sample the depth values at possibly uniform steps in a sufficiently large vicinity of the fault, and read out the Δg and m curves at the same points. Thus we arrive at three sets of data:

$$\begin{aligned} &h_1, \quad h_2, \quad \ldots, h_i, \quad \ldots, h_n \\ &\Delta g_1, \Delta g_2, \ldots, \Delta g_i, \ldots, \Delta g_n \\ &m_1, \quad m_2, \quad \ldots, m_i, \quad \ldots, m_n \end{aligned} \tag{5}$$

Since both the Δg and h curves contain a constant term which has no influence whatever on the shape of these curves let us denote the mean values of these curves by $\bar{h}$ and $\overline{\Delta g}$ and use, in what follows, the (similarly denoted) new values instead of the original ones:

$$\begin{aligned} h_1 &= h_1 - \bar{h} \\ &\vdots \quad \vdots \\ h_n &= h_n - \bar{h} \\ \Delta g_1 &= \Delta g_1 - \overline{\Delta g} \\ &\vdots \quad \vdots \end{aligned} \tag{6}$$

Then, by the least mean squares principle, those coefficients k_g, k_m will be adopted as optimum which minimize the mean square error:

$$\sum_{i=1}^{n} [(k_g \Delta g_i + k_m m_i) - h_i]^2. \tag{7}$$

Next, the gravitational depth:

$$h_{g,i} = k_g \Delta g_i + k_m m_i \tag{8}$$

and the deviation:

$$\Delta h_i = h_{g,i} - h_i \tag{9}$$

is computed with the optimum coefficients for every sampling point.

As usually, the accuracy of the approximation is measured by the standard deviation:

$$D = \sqrt{\frac{\sum \Delta h_i^2}{n}} \tag{10}$$

Of course, if we use a greater number of gravity anomaly curves of substantially different character the approximation would improve and the deviation (10) decrease.

As we have seen, the approximate depth values computed by Eq. (8) differ from the real depths by a constant term. In some of the formulae which follow this constant will be included, if it is neglected it means we do not need it for the subsequent considerations.

All what have been said above about optimized depth-calculations along profiles can be applied without any change to three-dimensional models. The optimization method studied on models, however, can only be used for practical interpretation if the depth data (e.g. seismic, geoelectric or bore-hole data) coincide with the gravitationally explorable body. If so, the above procedure should be performed for each point, and also the deviation, Δh_i between the given and the gravitationally computed depths data determined. Where the deviations are small, the gravity results prove the correctness of the other geophysical methods. Any significant deviation, however, requires a methodological or geological explanation.

It should be realized that seismic or geoelectric measurements are performed at certain points or along selected lines of the surface, thus the correlation of the results of different methods can be examined along these profiles only. If a fair correlation was achieved by means of optimally chosen coefficients k_g, k_m, between the computed gravitational depths and the seismic depth data along profiles, we could hope that this correlation would also hold true in the neighbourhood of the profiles, i.e. that these same coefficients could be used to get gravitational depth data at places where there had not been seismic measurements. This implies that the relatively inexpensive gravity method could fill in the gaps between the more expensive seismic profiles. There is a theoretical implication as well: having obtained the optimal coefficients k_g, k_m, we can determine a unique map-transforming matrix which yields the gravitational depth values directly from the anomaly map.

It should be emphasized, that this matrix is not identical to any of the various matrices named as optimal or sub-optimal in existing literature. Nevertheless, this matrix is certainly optimal in a sense that by its use we can optimally fit the measured anomaly values to the independently obtained depth data.

In other similar experiments, instead of the filtered anomalies the vertical derivatives have been used, together with Δg. As will be shown in the next section, depth values com-

puted from the Δg and $m(s, \varkappa)$ values, and those computed from Δg, g_z and g_{zz}, agree quite well. This fact should be emphasized, since a prerequisite of the use of filtered gravity data for practical depth computations is that the filtered anomaly maps should be similar to the derivative map.

4. Discussion of the Results of the Model Computations

We computed the gravitational effect Δg, the first and second vertical derivatives g_z and g_{zz} and the transformed anomalies $m(3)$, $m(4)$, $m(6)$ (obtained by the low-cut filter

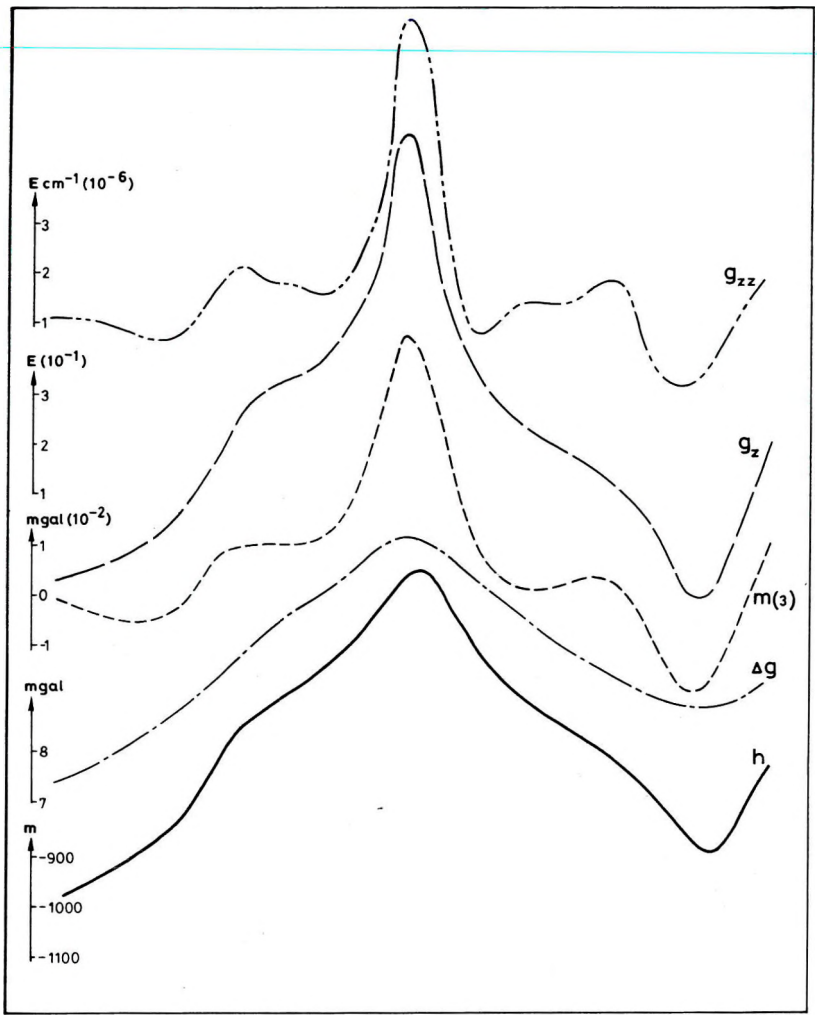

Fig. 6 Results of computations along the diagonal of the second sub-area of Model **A**
6. ábra. Az **A** modell 2. részterületének egy átlója mentén végzett számítások eredményei
Рис. 6. Результаты вычислений по диагонали второго участка модели **A**

matrices $m(s=500, \varkappa=3, 4, 6)$) corresponding to the three models of different depth and topography, described in section 3. Each model had been given by 160×160 depth values.

The computed results are represented as maps. Detailed results for a section of the map of Model **A** are shown in Figs. 4/1.–4/6.

It has been found from the figures that in any particular sub-area with the s value applied there was a striking similarity between the vertical derivatives (above all the second-vertical-derivative anomalies) and the anomalies obtained by low-cut filter matrices (Figs. 4/4, 4/5 and Fig. 6). As it has been mentioned already, the s value (sampling distance) used in the model computations agreed with the generally applied station interval in the field practice of Hungary: i.e. for bodies deeper than -1000 m, $s=500$ m, for bodies between -300 and -1000 m, $s=250$ m. Consequently, it is expected that the filters applied to the transformation of *actual* measured data would also result in vertical-derivative-like maps.

Let us consider the series of maps in Figs. 7/1, 2, 3, presenting a detail of an actual anomaly map series. The map of Fig. 7/3 has got a striking resemblance to a derivative map. The belts of asymmetric maxima and minima along the zero lines of the anomaly map (profile A–Á) do not correspond to local horsts, and grabens, rather, they represent typical derivative-like anomalies referring to the strike of a fault.

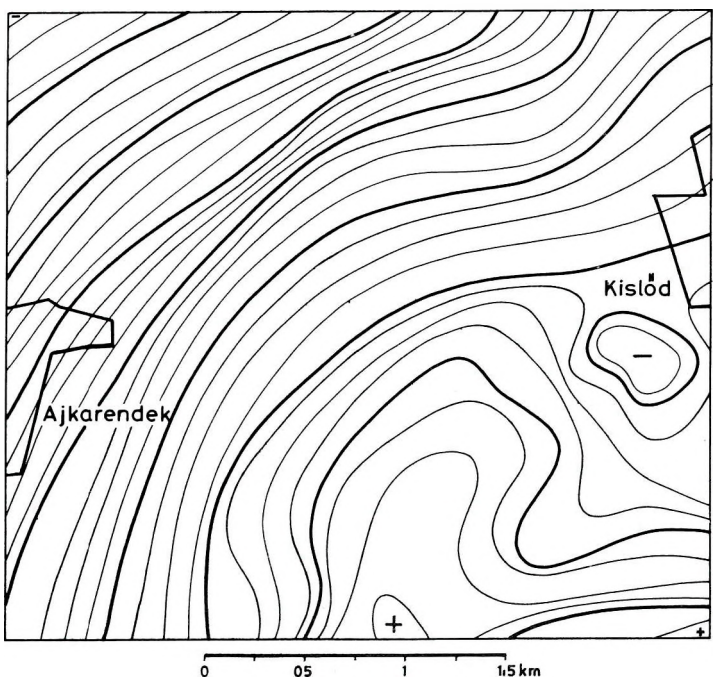

Fig. 7/1 Bouguer anomaly map of the Ajkarendek–Kislőd area (grid density appr. 6 station/km^2)

7/1. ábra. Ajkarendek–Kislőd környékének Bouguer-anomália térképe (a gravitációs ponthálózat sűrűsége kb. 6 áll/km^2)

Рис. 7/1. Карта аномалий Буге района Айкарендек–Кишлёд (плотность сети – прибл. 6 станций/km^2)

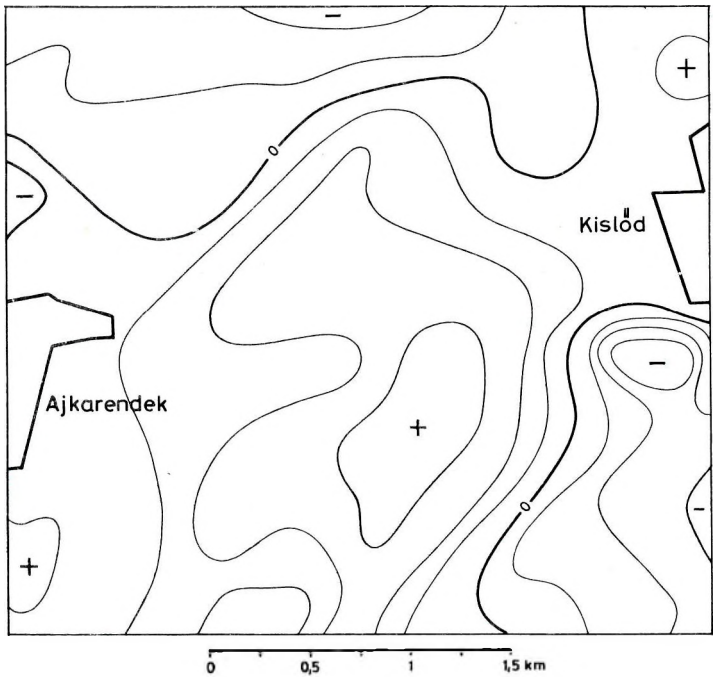

Fig. 7/2 Residual (?) derivative-like (?) filtered anomaly map of the Ajkarendek–Kislőd area

7/2. ábra. Ajkarendek–Kislőd környékének maradék (?) derivált(?) jellegű szűrt anomáliatérképe

Рис. 7/2. Профильтрованная карта остаточных (?) аномалий характера производных (?) для района Айкарендек–Кишлёд

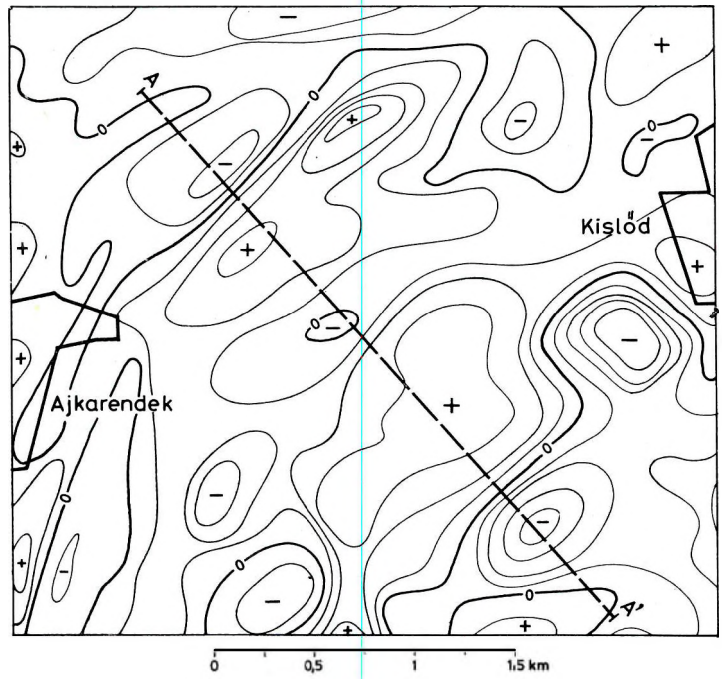

Fig. 7/3 Vertical-derivative-like filtered anomaly map of the Ajkarendek–Kislőd area

7/3. ábra. Ajkarendek–Kislőd környékének vertikális derivált jellegű szűrt anomália-térképe

Рис. 7/3. Карта аномалий характера вертикальных производных района Айкарендек–Кишлёд

The similarity of transformed anomaly maps, obtained by low-cut filter matrices, to the derivative anomalies leads us to assume that they are in a similar relationship with the shape of the anomalous bodies as the vertical derivatives.

Let the relief of the anomalous body be given by the depth values h_i. On the strength of Eq. (7) the connection between gravity anomalies and basement topography can be written for both derivatives and filtered anomalies in the same form:

$$\sum_{i=1}^{n} (k'_g \Delta g_i + k'_z g_{z,i} + k'_{zz} g_{zz,i} - h_i)^2 = \min, \tag{11}$$

$$\sum_{i=1}^{n} (k_g \Delta g_i + k_3 m(3)_i + k_4 m(4)_i + k_6 m(6)_i - h_i)^2 = \min. \tag{12}$$

Computations have been performed for all 16 sub-areas of Models **A, B, C** (i.e. for a total of 48 sub-areas). Each sub-area consisted of 30×30 points ($n = 900$). Computational results for Model **A** are compiled in Tables I and II. Depth values estimated by the respective formulae

$$h'_{g,i} = k'_g \Delta g_i + k'_z g_{z,i} + k'_{zz} g_{zz,i} \tag{13}$$

and

$$h_{g,i} = k_g \Delta g_i + k_3 m(3)_i + k_4 m(4)_i + k_6 m(6)_i \tag{14}$$

and the depth deviations

$$\Delta h' = h'_{g,i} - h_i \tag{15}$$

$$\Delta h = h_{g,i} - h_i \tag{16}$$

for two sub-areas of Model **A** are shown in Figs. 4/8, 9, 10, 11.

The computed depth values are deviations from the average depth of the particular sub-area. To obtain real depth values, this average should be added to the computed values:

$$h'_{g,i} = k'_g \Delta g_i + k'_z g_{z,i} + k'_{zz} g_{zz,i} + \bar{h} \tag{17}$$

and

$$h_{g,i} = k_g \Delta g_i + k_3 m(3)_i + k_4 m(4)_i + k_6 m(6)_i + \bar{h} \tag{18}$$

If, in practical cases, we want to extend the results of the calculations performed *along* seismic profiles to a part of the Bouguer map *between* profiles, we—of course—have to subtract the average value of the Bouguer anomalies along the profiles from the Bouguer map.

The data compiled in the Tables show that both kinds of depth values, computed either via the vertical derivatives or via the derivative-like transformed anomalies, agree fairly well with the real depths of the model: the standard deviations of both $\Delta h'$ or Δh (D' and D) are very small, of the order of 10–20 m.

Along some profiles of Model **A** we have tried to approximate h_g by the Δg map alone. From the condition

$$\sum_{i=1}^{n} (k \Delta g_i - h_i)^2 = \min. \tag{19}$$

we get the approximate values of

$$h_{g,i} \approx k \Delta g_i. \tag{20}$$

Table I (Model A)

	$\bar{h}$	$\bar{h}/s$	k'_g	k'_z	k'_{zz}	D'
1	−1130	2.25	2.6	1.6	0.1	7
2	− 860	1.70	2.5	1.7	0.0	10
3	−1250	2.50	2.8	0.5	0.5	14
4	−1550	3.10	3.2	−1.4	1.0	4
5	− 970	1.90	2.5	1.7	0.2	5
6	−1070	2.15	2.9	0.6	0.2	9
7	−1290	2.60	2.7	1.3	0.2	14
8	−1670	3.35	4.1	−5.5	1.5	4
9	−1230	2.45	3.0	−0.6	0.5	3
10	−1390	2.75	2.9	0.6	0.7	5
11	−1345	2.70	2.7	1.8	0.3	11
12	−1645	3.30	3.0	0.9	0.6	8
13	−1400	2.80	3.5	−2.6	1.0	3
14	−1545	3.10	3.7	−4.0	1.4	4
15	−1745	3.50	4.8	−9.5	2.1	5
16	−1700	3.40	3.9	−5.2	1.7	4

1	2	3	4
5	6	7	8
9	10	11	12
13	14	15	16

$\bar{h}, s$ (meter)
k'_g (meter/10^{-2} mgal)
k'_z (meter/10^{-1} E)
k'_{zz} (meter/10^{-7} E cm^{-1})
D' (meter)
$\Delta\sigma$ (0.1 g/cm^3)

But it was found that the scatter of the error $\Delta h_i = h_{g,i} - h_i$ is generally larger by 50% than when derivative-like transformed anomalies have also been involved in the computations. As an example, Table III/a shows the averaged results of computations performed along 10 different profiles. Consequently, it is necessary to incorporate the derivative-like transformed anomalies into the quantitative determination of the relief of the anomalous body.

The respective deviations D' and D of $\Delta h'_i$ and Δh_i are nearly equal on all the 48 subareas (Fig. 8.), although the scatter of the $\Delta h'_i$ values is somewhat smaller. This proves that, for any fixed s, the transformed anomalies obtained by low-cut filter matrices have essentially the same role in mapping the relief of the model as the vertical derivatives.

The depth errors are practically independent of the average depth of the area (Fig. 9). The relatively larger scatters in case of Model B are due to the relatively smaller solid angles.

Indeed, from among the approximations and neglections adopted in the calculations, that is the most important, that depth-data beyond a distance of 5000 m have not been taken into account at all. While for Models A and C the computed errors prove that this neglecting has been justified, in case of Model B—due to its maximum depth of −4000 m—the solid angle corresponding to a neighbourhood of 5000 m seems to be too small.

Table II (Model **A**)

	$\bar{h}$	$\bar{h}/s$	k_g	k_3	k_4	k_6	D	k_m^*	k_m/k_g
1	−1130	2.25	3.0	−1.6	6.4	4.8	8	4.8	1.6
2	−860	1.70	2.9	1.7	−4.5	12.5	10	3.5	1.2
3	−1250	2.50	3.0	−10.4	23.0	11.3	15	10.2	3.4
4	−1550	3.10	3.2	3.6	9.1	3.4	6	11.4	3.5
5	−970	1.90	2.9	−1.9	7.6	6.2	6	5.9	2.0
6	−1070	2.15	3.0	−3.5	7.7	7.5	10	4.8	1.6
7	−1290	2.60	3.1	−2.7	7.0	12.8	15	6.6	2.1
8	−1670	3.35	3.1	3.7	11.8	4.8	7	13.8	4.4
9	−1230	2.45	3.0	2.4	7.0	1.0	4	6.3	2.1
10	−1390	2.75	3.1	−3.7	16.0	7.5	7	10.5	3.4
11	−1345	2.70	3.3	−1.5	6.0	13.8	12	8.1	2.6
12	−1645	3.30	3.0	1.5	8.1	7.9	10	10.3	3.1
13	−1400	2.80	3.1	7.2	3.0	−1.7	4	8.5	2.8
14	−1545	3.10	3.2	4.2	8.5	3.3	6	11,5	3.6
15	−1745	3.50	3.2	1.1	16.3	5.4	9	14.6	4.6
16	−1700	3.40	3.2	9.8	6.6	−2.7	6	13.4	4.2

1	2	3	4
5	6	7	8
9	10	11	12
13	14	15	16

$^*k_m = k_3 + 0.7k_4 + 0.4k_6$.
$\bar{h}$, s (meter)
k_g, k_3, k_4, k_6, k_m (meter/10^{-2} mgal)
D (meter)
$\Delta\sigma$ (0.1 g/cm^3)

Table III

a)		D	%
1	$h_g = 3.4\Delta g$	29	100
2	$h_g = 1.5\Delta g + 7.3g_z$	12	41
3	$h_g = 2.9\Delta g + 0.6g_{zz}$	11	38
4	$h_g = 2.5\Delta g + 1.8g_z + 0.5g_{zz}$	10	34
5	$(h_g = 1.3g_z + 0.1g_{zz}$	17	58)
6	$h_g = 2.9\Delta g + 10.6m(3)$	14	48
7	$h_g = 2.9\Delta g + 15.0m(4)$	14	48
8	$h_g = 2.9\Delta g + 25.8m(6)$	14	48
9	$h_g = 2.9\Delta g + 1.5m(3) + 9.1m(4) + 7.7m(6)$	11	38
b)	if: $m(4) \sim 0.7m(3)$ and $m(6) \sim 0.4m(3)$ then: $k_{m_4} \sim 0.7k_{m_4} \sim 0.4k_{m_6}$ i.e.:		
7	$h_g \sim 2.9\Delta g + 10.5m(3)$		
8	$h_g \sim 2.9\Delta g + 10.3m(3)$		
9	$h_g \sim 2.9\Delta g + 10.9m(3)$		

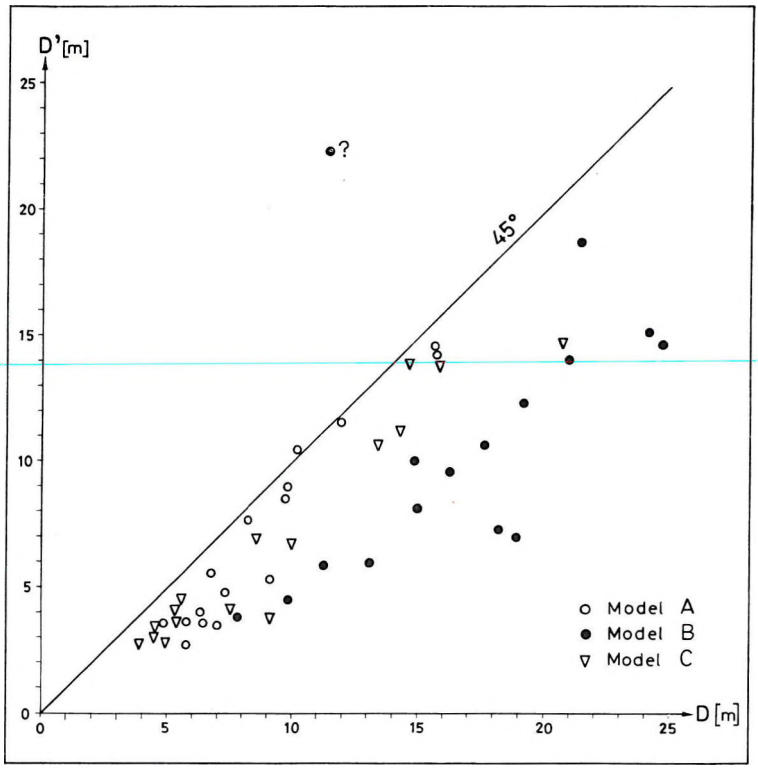

Fig. 8 Standard deviations of the depth calculations from both the Δg—vertical derivatives (D') and the Δg—filtered anomalies (D)

8. ábra. A Δg és a vertikális deriváltak, valamint a Δg és a szűrt anomáliák bevonásával végzett mélységszámítások szórásai

Рис. 8. Среднеквадратичные отклонения подсчитанных глубин от вертикальных производных Δg, (D') и от профильтрованных аномалий Δg, (D)

The areal distribution of the errors obey the same rules for all three models: the more varied the topography, the greater the scatter (Fig. 10). At such locations a more accurate depth calculation can be expected from reduced sampling distances only.

A series of experiments have been performed along several profiles to investigate the effect of incorporating of one or more derivatives or filtered anomalies into the depth computations. The results are compiled in Table III. It can be stated that, for a given s, the result of depth transformation is practically independent of the particular kind of the derivative-like transformed anomaly combined with the Δg map. In practice, for a given s, it seems to be sufficient to combine a single derivative-like filtered anomaly with Δg. If we use a greater number of derivative-like (s = const, $\varkappa$) anomalies, their corresponding coefficients will be seemingly random (Fig. 11), although a closer scruting reveals that they do obey some rules.

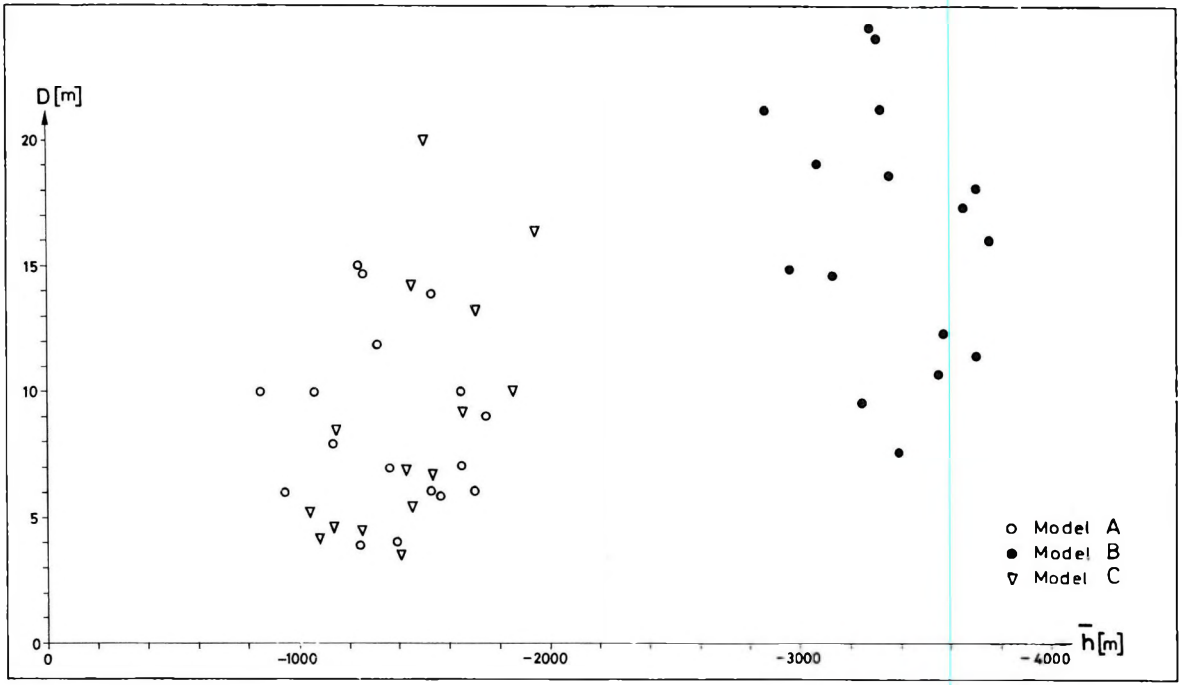

Fig. 9 Standard deviations of the depth values, computed from the Δg and the filtered anomalies, as a function of average depth

9. ábra. A Δg és a szűrt anomáliák segítségével meghatározott mélységértékek szórása az átlagmélységek függvényében

Рис. 9. Среднеквадратичные отклонения величин глубин, подсчитанные по Δg и по профильтрованным аномалиям, в зависимости от средних глубин

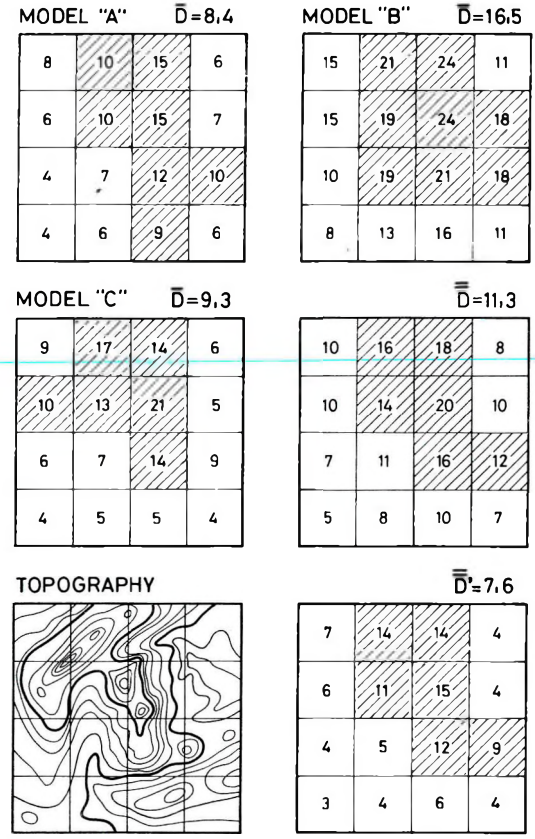

Fig. 10 Areal distribution of the errors of gravitationally computed depth values for models **A, B,** and **C.** $\bar{D}$ means the average of the standard deviations of depth values computed from Δg and $m(s, \varkappa)$ data for each model, $\bar{\bar{D}}$ means the average of the three models. For comparison $\bar{\bar{D}}'$, computed from depth calculations applying Δg, g_z and g_{zz} anomalies is given as well. The areal distribution of $\bar{\bar{D}}$ and $\bar{\bar{D}}'$ is similar: values above average (shaded) coincide with sharp topography.

10. ábra. A gravitációs mélységértékek szórásának területi eloszlása az **A, B** és **C** modellnél. $\bar{D}$ jelenti a Δg és az $m(s, \varkappa)$ adatokból számított mélységek szórásait az egyes modelleknél, $\bar{\bar{D}}$ a három modell átlagszórását. Összehasonlításul a Δg, g_z és g_{zz}-ből számított D'-t is közöljük. A D és a D' területi eloszlása hasonló jellegű, az átlagnál nagyobb szórást (vonalkázott terület) ott tapasztalunk, ahol a topográfia a legváltozatosabb

Рис. 10. Территориальное распределение погрешностей глубин, подсчитанных по гравиметрическим данным, для моделей **A, B** и **C.** $\bar{D}$ означает среднюю величину среднеквадратичных отклонений глубин, подсчитанных по данным Δg и $m(s, k)$, для каждой из моделей; $\bar{\bar{D}}$ – среднюю для трех моделей величину. Для сопоставления приведены также величины $\bar{\bar{D}}'$, подсчитанные по вычислениям глубин с использованием аномалий Δg, g_z и g_{zz}. Территориальное распределение $\bar{\bar{D}}$ и $\bar{\bar{D}}'$ оказывается подобным: величины, превышающие среднюю (штриховка), совпадают с резко расчлененной топографией

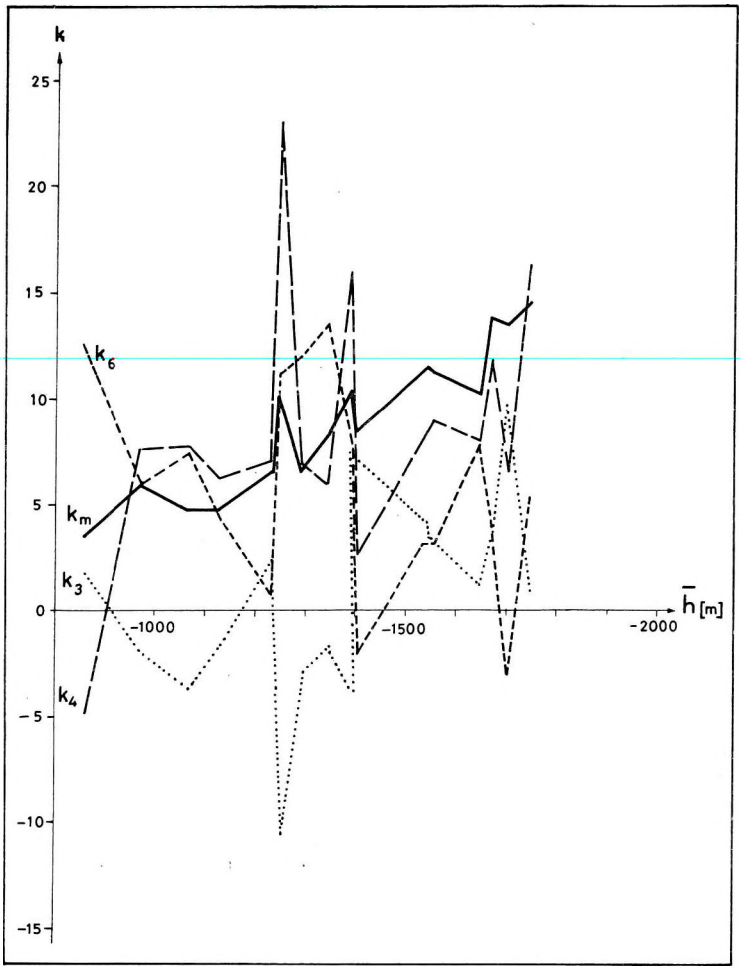

Fig. 11 Behaviour of the coefficients corresponding to different kinds of filtered maps, for the 16 sub-areas of Model **A**, as a function of average depth.

$$k_m = k_3 + 0.7k_4 + 0.4k_6$$

11. ábra. A különböző $\varkappa$ paraméterű szűrt anomáliák szorzóinak alakulása mélység számításánál az **A** modell 16 részterületén (a részterületek átlagmélységének függvényében)

$$k_m = k_3 + 0{,}7k_4 + 0{,}4k_6$$

Рис. 11. Зависимость коэффициентов, соответствующих различным видам профильтрованных карт, для 16 участков модели **A**, от глубины

$$K_m = K_3 + 0{,}07K_4 + 0{,}04K_6$$

Indeed, for any given s, the "amplitudes" of the derivative-like filtered anomalies $m(\varkappa)$ decrease as $\varkappa$ increases. Taking the $m(3)$ amplitudes as 100%, the $m(4)$ anomalies will be around 70%, the $m(6)$ anomalies some 40%. (This can be checked on the maxima of Figs. 1, 4/5, 4/6, 4/7, or by direct calculations.) This means that the coefficients k_4 and k_6 will be proportionally larger. By reducing the coefficients k_4 and k_6 by the appropriate factors we get back almost exactly the value of k_3 (Table III/b). Applying this to the areal results compiled in Table II, i.e. by reducing the k_4 and k_6 weights in that Table to their 70% and 40% fractions, and summing these new coefficients $\left(k_m = k_3 + \frac{k_4 \cdot 70}{100} + \frac{k_6 \cdot 40}{100}\right)$ we obtain a single weight factor k_m which can be applied for the combination of the single derivative-like transformed anomaly $m(s = \text{const}, \varkappa = 3)$ with the Δg map.

Now let us plot k_m and k_g as a function of depth (Fig. 12). It is apparent that both values grow with increasing depth. Of course, the actual values of both coefficients depend on the density contrast $\Delta\sigma$ as well. To be able to draw conclusions which are independent of $\Delta\sigma$ and of the distance unit, let us plot the ratio k_m/k_g as a function of distance, where distance is measured in s units (Fig. 13).

Fig. 13 shows an approximately linear relationship in the range of $s = 0.5 - 4.0$. The relatively large scatter of Model **B** might be due to the small solid angles used in the computations. By means of the linear section we can construct a preliminary depth map in practical cases, if the two-layer model is approximately valid. More exactly, let us express the average depth of the anomalous body (i.e. of the basement) in terms of s, where s is the parameter of the $m(s, 3)$ filter.

If, say $s = 250$ m, and the average depth of the basin floor from the surface is 600 m, we will put $h = 2.45$ s. According to Fig. 13 the corresponding k_m/k_g ratio is 2.5. If, say $k_g = 1$ then $k_m = 2.5$. Let us multiply each point of our $m(250, 3)$ map by $k_m = 2.5$ and add it to the original Bouguer anomaly map. Thus, we obtain a corrected Bouguer anomaly map ($B_k = B + k_m \cdot m$).

If there are available bore-hole, seismic, or geoelectric data, we can construct a $B_k = f(h)$ function to transform the B_k map to depth-dimension. This last step is advisable only if there is no sufficient amount of depth-data for the accurate determination of k_g, k_B and k_m.

If we have an abundance of seismic and geoelectric depth data for the exploration site, there is a possibility for a more accurate determination of the constants k_B and k_m. Such a case is presented in Table IV, for some of the peripheral or inner basins of the Transdanubian Central Range. The computed k_m/k_B ratios as a function of average depth, expressed in s units, are plotted in Fig. 13 as full squares. There is a very good agreement between the results obtained from the model experiments and from actual field measurements.

Calculations were carried out to determine the number of data necessary for a sufficiently accurate determination of the k coefficients. For sub-area 2 of Model **A** we have determined these constants from $n = 900$ points, then—along certain profiles—from 90 points, along a diagonal from 30 points, afterwards from each second diagonal point (i.e. from 15–15 points), and finally from 8–8 points (Table V.). It can be seen that the constants can be determined fairly accurately, even from very few points. In practical cases, of course, the correlation conditions are not that simple and it is advisable to use several hundred points in the least squares fit.

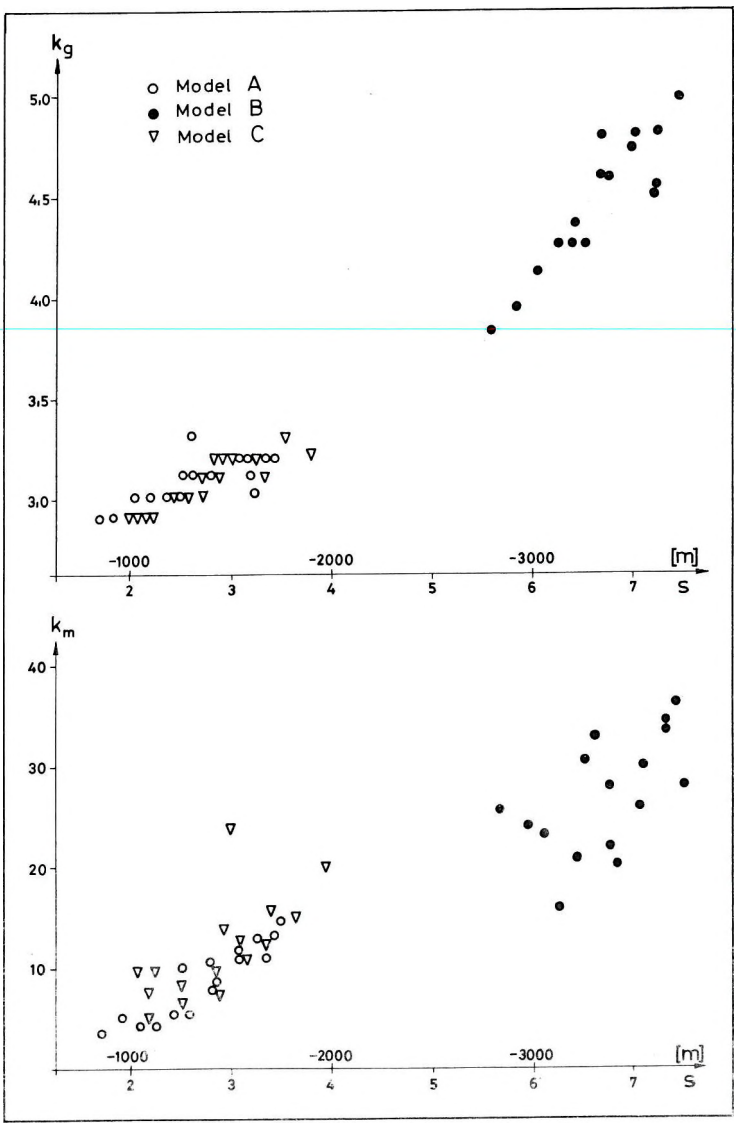

Fig. 12 The values of k_g and k_m as a function of depth
12. ábra. A k_g és a k_m értékek a mélység függvényében
Рис. 12. Зависимость величин k_g и k_m от глубины.

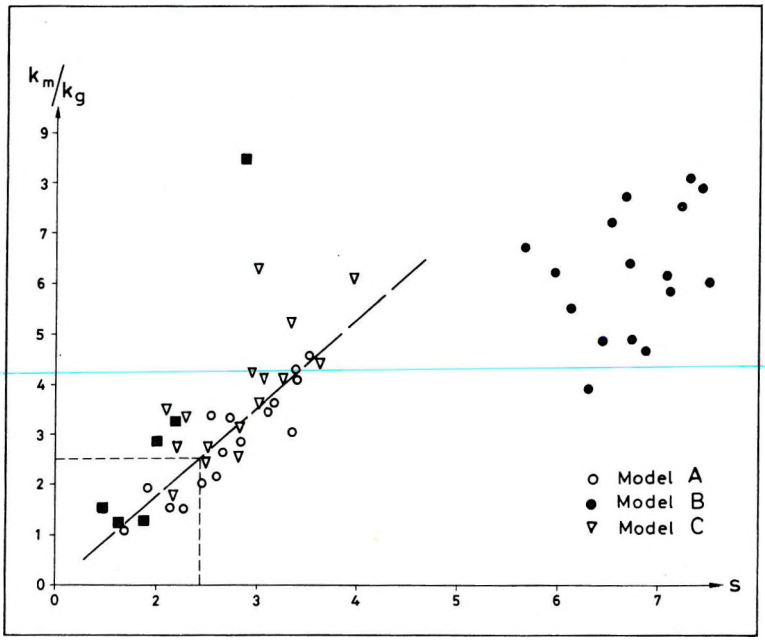

Fig. 13 The ratio k_m/k_g as a function of average depth. Depth values are expressed in s units. Full squares represent values computed from data measured on different areas of Hungary.

13. ábra. A k_m/k_g értékek az átlagmélységfüggvényben (méretarányától és $\Delta\sigma$-tól független diagram, amely alkalmas a modellszámítási és gyakorlati eredmények összevetésére)

Рис. 13. Зависимость отношения k_m/k_g от средней глубины. Глубины выражены в единицах s. Квадраты представляют собой величины, подсчитанные по данным, полученным в различных районах Венгрии.

Table IV.

Average values for Model A
Az A modell átlagértéke

		k_m/k_g	h/s ($s=500$)
$\Delta\sigma=0.1$	$h_g=3.08(\Delta g-\overline{\Delta g})+9.01m(3)-1360$	2.89	2.72
0.2	$=1.54$ 4.50		
0.3	$=1.02$ 3.00		
0.4	$=0.77$ 2.25		
0.5	$=0.62$ 1.80		
0.6	$=0.51$ 1.50		
0.7	$=0.44$ 1.28		
0.8	$=0.38$ 1.12		

Values computed from field results
Mérési adatokból számított értékek

KOCS–SZEND	$h_g=0.49(B-\overline{B})+0.53m(3)-400$			1.08	1.60 ($s=250$)
TARJÁN–SZOMOR	$=0.64$	$+0.70$	-450	1.09	1.80
MAGYARPOLÁNY	$=0.64$	$+0.88$	-350	1.38	1.40
CSOLNOK	$=0.29$	$+0.90$	-550	3.10	2.20
BAKONYSÁRKÁNY	$=0.52$	$+1.42$	-475	2.73	1.90
KISBÉR	$=0.36$	$+2.99$	-700	8.30	2.80

Table V

n	$\overline{\Delta g}$	h	m	k_g	k_m	D	k_m/k_g
900	892	−860	0.80	2.9	3.5	10	1.2
90	870	−900	0.65	2.9	4.0	11	1.3
30	831	−947	0.53	2.9	4.3	13	1.5
15	826	−952	0.13	2.9	4.1	13	1.4
15	835	−942	0.93	2.9	4.8	11	1.6
8	827	−951	3.6	3.4	−1.4	14	–
8	815	−963	−0.25	2.9	4.8	10	1.6

$\Delta\sigma$ (0.1 g/cm^3)
Δg (10^{-2} mgal)
h (meter)
m (10^{-2} mgal)
k (10^{-2} mgal/m)
D (meter)

In case of the model experiments the Δh maps (Figs. 4/10, 4/11) reflect the error of depth calculation only. Large Δh values occur at those places, where the relief abruptly changes. It should be anticipated that these errors would increase for a more appropriate (smaller) s value. Certainly, the exact solution in case of $\varkappa = 3$, $s = 1$, 0.5 and 0.25 should be sought in the form:

$$\sum_{i=1}^{n} [k_g \Delta g_i + k_1 m(1;3)_i + k_2 m(0.5;3)_i + k_3 m(0.25;3)_i - h_i]^2 = \min. \qquad (19)$$

These experiments will definitely add to our understanding of the optimal sampling distance and filtersize.

In practical cases the Δh errors do not depend on the accuracy of depth computations alone. The Δh values characterize—besides the accuracy of the original Bouguer anomalies and of the depth data applied—the changes in the geological build-up. This means that it is advisable to exclude any other inaccuracies influencing the Δh errors, to be able to predict changes in the geological set up. To achieve this, practical calculations should be performed in several stages. First, accepting the *a priori* depth-data, we determine the coefficients k_B and k_m, and, by means of these, the errors Δh_i. By analysing the areal distribution of the Δh_i values, we try to separate the technical errors from those of possible geological significance. In some cases even the seismic (geoelectric) interpretation should be reviewed. If the areal distribution of the Δh_i-s is inhomogeneous, we might decide to determine separate weight factors for certain sub-areas.

That is, the final values of k_B and k_m are obtained as follows: after a thorough check-up of the input data and, if necessary, by dividing the site into sub-areas, we leave out those points for which $\Delta h_i > 150$ m; then we make a further approximation and leave out points for which $\Delta h_i > 100$ m; then, after a final approximation, we leave out points for which $\Delta h_i > 50$ m. Using the final values of k_B and k_m we compute again the depths h_{gi}, and the deviations Δh_i, for *all* points. If the computational and measurement errors are indeed negligible, the areal distribution of the Δh_i values obtained will have a definite geological meaning.

Finally, we should assign a place to our new method between the more familiar map transformations. The depth-transformation, as defined above, can be considered in a sense as a special kind of *downward continuation,* where the appropriate constants of continuation are not fixed, but are always taylored to the actual exploration task. Or we can try the frequency-domain terminology: frequencies necessary for the solution of the geological task are picked from the Bouguer map, get amplified and then fed back. But no matter what point of view we adopt, the sampling distance retains its crucial role. In the present practice the sampling distance s used in map transformations is determined by the average station interval. Generally we do not apply matrices with s values substantially smaller than the average separation of stations because otherwise the map transformation would largely depend on interpolated values.

Since, due to the well known features of the gravity field, the positive anomalies have a stronger effect than the negative ones it would be a straightforward generalization of the presented method to determine separate weight factors for the positive and negative $m(s, \varkappa)$ anomalies.

5. Conclusions

1. A new method has been elaborated for the calculation of the gravity effect of arbitrarily complex geological models.
2. Applying a series of low-cut filter-matrices to a Bouguer anomaly map with gradually decreasing sampling distances, we obtain, in turn, a residual anomaly map being almost identical to the Bouguer map, then a more realistic residual anomaly map, and, finally, vertical derivative-like maps. By appropriate filters we can produce any formal transition *between* geologically interpretable maps. (Up to now, there is no unbiassed criterium for the appropriate choice of the sampling distance (parameter s), except the obvious rule of thumb that it certainly should be less than the explored depth.)
3. For sufficiently small s values the gravity anomalies obtained via low-cut filtering are similar to the vertical-derivative anomalies.
4. Vertical-derivative-like anomalies bear information on the shape of the anomalous bodies, while the regional-free Bouguer anomalies are related to the depth of these bodies. There exists a suitable linear combination of the Bouguer and vertical-derivative-like anomalies which—under suitable geological conditions—yields a directly interpretable contour-map.
5. During the calculations of depth maps each point of the gravity maps (i.e. both the Bouguer and the filtered, vertical-derivative-like maps) get a quantitative meaning.
6. By means of model experiments we obtained empirical formulae for the preparation of preliminary depth maps, if the average depth of the area is known.
7. In order to construct more accurate depth maps, the transformation constants should be determined for each particular area. For this purpose we need a relatively few, but accurate (bore-hole or geophysical) depth data.
8. The model experiments have proved that the accuracy of depth calculation is influenced first of all by the complexity of the relief of the anomalous body, rather than by its average depth.
9. Any significant deviation between gravitationally computed and geophysically-geologically obtained depth values has a definite geological meaning.
10. The depth computation as presented in this paper has been optimally tailored to present-day field practice, interpretation and computational methods.

11. The method of depth calculation presented can be considered as a special kind of downward continuation, where the transformation constants are not fixed in advance but are always adjusted to the actual exploration task.
12. The model experiments presented ask for further research, of both theoretical and practical nature.

REFERENCES

JUNG, K. 1961: Schwerekraftverfahren in der angewandten Geophysik. Akademische Verlagsgesellschaft, Leipzig

MESKÓ, A. 1965: Some notes concerning the frequency analysis for gravity interpretation. Geophys. Prosp. Vol. XIII, No. 3

MESKÓ, A. 1966: Two-dimensional filtering and the second derivative method. Geophysics Vol. XXXI, No. 3

HAÁZ, I. B. 1969: Contributions to the calculations of the gravitational attraction of a right rectangular prism. Geofizikai Közlemények (Geophysical Transactions) Vol. XVIII, No. 4. (in Hungarian)

SZABADVÁRY, L.,–HOFFER, E.,–NYITRAI, T.,–RÁNER, G.,–SZ. PINTÉR, A., 1973: Methodical problems of integrated geophysical measurements. Magyar Geofizika Vol. XIV, No. 5–6. (in Hungarian)

SZ. PINTÉR, A.,–STOMFAI, R., 1974: An attempt to determine a local matrix transforming the Bouguer-anomaly map into a depth chart. Magyar Geofizika Vol. XV. No. 5–6. (in Hungarian)

PINTÉR ANNA—STOMFAI RÓBERT

GRAVITÁCIÓS MODELLSZÁMÍTÁSOK

A gravitációs térképekre alkalmazott szűrők matematikai tulajdonságaival az irodalom kimerítően foglalkozik. A jelen cikkben ismertetett gravitációs modellkísérlet célja az volt, hogy — elfogadva egy, az irodalomban javasolt szűrési eljárást — a szűrt anomáliák földtani értelmezési lehetőségeire keressünk módot.

Eredményeinket a következőkben foglalhatjuk össze:

1. Kidolgoztunk olyan háromdimenziós hatásszámítási eljárást, amelyeknek segítségével elvileg tetszés szerinti bonyolultságú földtani modell gravitációs hatása kiszámítható.
2. A Bouguer-anomália térképből az alulvágó szűrőmátrixokkal a mintavételi távolság fokozatos csökkentésével a Bouguer-anomália térképtől alig eltérő maradékanomália térkép, majd reális maradék anomália térkép, s végül vertikális derivált jellegű térképek állíthatók elő. A reális, földtanilag értékelhető térképek között minden formális átmenet előállítható. (A mintavételi távolság (*s* érték) megválasztására nincs objektív kritérium. Némi támpontot jelent az, hogy a mintavételi távolságnak a kutatási mélységnél feltétlenül kisebbnek kell lennie.)
3. Az alulvágó szűrőmátrixokkal számított gravitációs anomáliák elegendően kicsiny *s* érték mellett vertikális derivált jellegű anomáliák.
4. A vertikális derivált jellegű anomáliák a ható alakjának leképzésénél játszanak szerepet — míg a regionális hatástól mentes Bouguer-anomáliák a ható mélységével vannak szorosabb kapcsolatban. A Bouguer és a vertikális derivált jellegű anomáliák alkalmas kombinációjával a földtani kutatás szempontjából közvetlenül értelmezhető mélységtérképet állíthatunk elő, kedvező földtani fölépítésű területen.

5. A mélységtérkép számításakor minden egyes (tehát a gyakorlatban sok ezer) Bouguer-, és minden egyes vertikális derivált jellegű szűrt anomáliaérték kvantitatív értelmet kap. Ezt eddig egyetlen eljárás sem biztosította.
6. A modellkísérletek alapján előzetes mélységtérkép készítéséhez — a terület várható átlagmélységének függvényében — előzetes transzformáló konstansokat adhatunk.
7. Pontosabb mélységtérkép előállításához alkalmas transzformáció konstansait minden egyes területre (területrészre) külön kell megállapítani. Ehhez viszonylag kevés, de megbízható (fúrási vagy geofizikai) mélységadat szükséges.
8. A modellkísérletek szerint a mélységszámítás megbízhatósága gyakorlatilag nem annyira a terület átlagmélységétől, hanem sokkal inkább a ható (aljzat) domborzat bonyolultságától függ.
9. A gravitációs adatokból számított mélységek és az egyéb, földtani-geofizikai mélységértékek közötti eltérésekből az aljzatra vagy a fedőre vonatkozó földtani többletinformációt nyerhetünk.
10. A mélységszámítási eljárást a gyakorlatban alkalmazott mérési, kiértékelési és számítási technikához optimalizáltuk.
11. Az ismertetett mélységszámítási eljárás olyan analitikus lefelé folytatásként értelmezhető, amelynél a lefelé folytatáshoz szükséges konstansokat nem egyszer s mindenkorra rögzítjük, hanem magukból a mérési adatokból esetenként határozzuk meg.
12. A modellkísérletek a gyakorlati kutatások számára és a modellezés továbbfolytatásához is konkrét és egyértelmű irányt mutatnak.

А. ПИНТЕР–Р. ШТОМФАИ

МОДЕЛИРОВАНИЕ ДЛЯ ИНТЕРПРЕТАЦИИ АНОМАЛИЙ ПОЛЯ СИЛЫ ТЯЖЕСТИ

Математические особенности фильтров, применяемых при построении карт аномалий поля силы тяжести подробно описаны в литературе. Целью рассматриваемых в настоящей работе модельных исследований было нейти возможность геологической интерпретации профильтрованных аномалий, исходя из рекомендуемого в литературе способа фильтрации.

Полученные при этом результаты сводятся к следующему.

1. Разработан метод решения обратной задачи для трехмерного тела, позволяющий вычислить гравитационный эффект геологической модели в принципе с любой степенью сложности.
2. По картам аномалий Буге, с использованием матриц фильтров левого среза, при постепенном уменьшении шага выборок, можно получить карту остаточных аномалий, почти не различающуюся от карт аномалий Буге, затем – карту реальных остаточных аномалий, и наконец – карты характера вертикальных производных. Между реальными, геологически интерпретируемыми картами можно создать всякие формальные переходы (для выбора шага выборок (величины s) нет объективного критерия. При этом в определенной мере можно руководствоваться тем, что шаг выборок должен быть обязательно меньшим по сравнению с глубиной исследования).
3. Аномалии поля силы тяжести, вычисленные с использованием матриц фильтров левого среза, представляют собой – при довольно низких величинах s – аномалии характера вертикальных производных.
4. Аномалии характера вертикальных производных играют роль при определении формы возмущающего тела, в то время, как аномалии Буге, свободные от влияния регионального поля, связаны более тесно с глубиной залегания этого тела. В районах с благоприятным геологическим строением, при соответствующем комбинировании аномалий Буге с аномалиями характера вертикальных производных, можно получить прямо интерпретируемые для геологических целей карты глубин.

5. При вычислении карты глубин каждая из величин аномалий Буге (а их на практике много тысяч) и каждая из величин профильтрованных аномалий характера вертикальной производной, получает количественное значение. Ни один из применявшихся до сих пор методов не дал такой возможности.
6. По модельным исследованиям, для построения предварительной карты глубин, можно задать предварительные постоянные преобразования, в зависимости от ожидаемой средней глубины, характерной для изучаемого района.
7. Постоянные преобразования для построения более точной карты глубин дольжны быть отдельно определены для каждого района (участка). Для этого необходимо иметь сравнительно небольшое количество, но достоверных (буровых или геофизических) данных о глубинах.
8. Работы по моделированию показывают, что достоверность вычисления глубин зависит практически не настолько от средней глубины, а скорее всего от сложности рельефа возмущающего тела (основания).
9. Разницы между глубинами, подсчитанными по гравиметрическим данным и прочим геолого-геофизическими величинами глубин, дают дополнительную информацию о геологическом строении основания или покрова.
10. Оптимальный вариант метода был выбран с учетом применяемых на практике методов наблюдений, интерпретации и техники вычислений.
11. Описанный выше метод вычисления глубин может рассматриваться как аналитическое продолжение поля в нижнее полупространство, при котором необходимые постоянные определяются не раз и на всегда, а в каждом случае, исходя из данных наблюдений.
12. Проведенное моделирование позволяет конкретно и однозначно определить направление проведения производственных разведочных работ, а также продолжения работ по моделированию.

Magyar Állami Eötvös Loránd Geofizikai Intézet
GEOFIZIKAI KÖZLEMÉNYEK
25

CONNECTION BETWEEN THE INNER STRUCTURE AND THE STATIC DEFORMATIONS OF THE EARTH CAUSED BY EXTERNAL FORCES

P. VARGA*

The load numbers have been determined from the system of differential equations of MOLODENSKIY (1953) describing static deformations. As in our earlier paper (VARGA 1974) we transformed the system of equations to the form

$$A = r^2\mu\left(T' + H - \frac{2}{r}T\right) \tag{1}$$

$$B = (\lambda + 2\mu)H' + \lambda\left[\frac{2}{r}H - \frac{n(n+1)}{r^2}\cdot T\right] \tag{2}$$

$$C = r^2(R' - 4\pi f\varrho H) \tag{3}$$

$$-A' = \varrho r^2(R + W'H) + Br^2 + 2\mu[H - (n^2+n-1)T - H'r^2] \tag{4}$$

$$-B' = \varrho\left[\frac{c}{r^2} - 4W'\frac{H}{r} + \frac{n(n+1)}{r^2}\cdot TW'\right] + \\ + \frac{2\mu}{r}\left[2H' - \frac{2H}{r} + \frac{n(n+1)}{r^2}T\right] - \frac{n(n+1)}{r^4}\cdot A \tag{5}$$

$$C' = n\cdot(n+1)\cdot(R - 4\pi f\varrho T) \tag{6}$$

where

$\mu = \mu(r)$; $\lambda = \lambda(r)$	Lamé parameters
$\varrho = \varrho(r)$	density
$W = W(r)$	geopotential
f	gravitational constant
n	order of deformation
$R = R_n(r)$, $H = H_n(r)$, $T = T_n(r)$	functions describing the Love numbers of the respective order corresponding to deformations on the surface
A, B, C	auxiliary functions as defined in Eqs. (1)–(3)

Dash-denoted derivatives are taken with respect to the distance from the centre of the Earth.

From among the six boundary conditions which are necessary for the solution of the system of differential equations three are given on the surface of the Earth. The first

* Geophysical Institute 'Roland Eötvös', Budapest
Manuscript received 27. 2. 1978

expresses the continuity of the derivative of the mass potential function, the second states that there are no tangential stress components along the surface of the Earth, while the last condition determines the normal load, N, acting on the surface:

$$R' - (2n+1)W + \frac{n+1}{\bar{a}} R - 4\pi f \varrho H = 0 \tag{7}$$

$$\mu\left(T' - \frac{2}{\bar{a}} T + H \right) = 0 \tag{8}$$

$$(\lambda + 2\mu) H' + \lambda\left(\frac{2}{\bar{a}} H - \frac{n(n+1)}{\bar{a}^2} T \right) = N$$

$\bar{a}$ is the average Earth-radius in the above equations. Using the results of MOLODENSKIY (1953) and assuming the hydrostatic nature of the normal load, i.e. that

$$N = -\varrho g_0 h$$

(where g_0 is the acceleration of gravity on the surface of the Earth and h is the height of the water-column), we get the third boundary condition:

$$(\lambda + 2\mu) \cdot H' + \lambda\left(\frac{2}{\bar{a}} \cdot H - \frac{n(n+1)}{\bar{a}^2} \cdot T \right) = -\frac{2n+1}{4\pi f} g_0^2. \tag{9}$$

The second group of boundary conditions are obtained from the conditions referring to the core-mantle boundary ($r = b$). Assuming that the loading effect is negligible at this depth, the core is incompressible and elastic, and further, that the density distribution is fluid-like, we obtain the followings:

$$\mu_e\left(T' - \frac{2}{b} T + H \right) - \mu_i\left(\frac{2n+1}{b} \cdot T - \frac{3}{n} \cdot H \right) = 0 \tag{10}$$

$$(\lambda_e + 2\mu_e) \cdot H' + \lambda_e\left(\frac{2}{b} H - \frac{n(n+1)}{b^2} T \right) +$$

$$+ \varrho_i (R + W'H) - \mu_i \left[\frac{2n^2 + n + 3}{n \cdot b} \cdot H - \frac{3(n+1)}{b^2} \cdot T \right] = 0 \tag{11}$$

$$R' - R \cdot \gamma - \frac{n}{b} R + 4\pi f (\varrho_i - \varrho_e) H = 0 \tag{12}$$

index e in Eqs. (10)–(12) denotes the physical parameters of the mantle, while index i refers to the core. γ characterizes the density distribution within the core, and can be determined from the differential equation (MOLODENSKIY, 1953) shown below:

$$\gamma' + \gamma^2 + \frac{2(n+1)}{r} \gamma + 4\pi f \frac{\varrho'}{W'} = 0. \tag{13}$$

The system of differential equations (1)–(6) subject to boundary conditions (7)–(12) has been solved by using the fourth order RUNGA-KUTTA method, with a relative Earth-radius step of 0.005, within the limits of the surface and the core-mantle boundary.

The aim of the calculations was to clarify the following questions:

1. What is the effect of the location and the physical state of the core-mantle boundary upon the load numbers?
2. To what extent does mantle structure influence the load numbers?
3. How surface conditions effect the load numbers?

As it is well known, from the simple combinations of the load numbers

$$k'_n = R_n(\bar{a}) - 1; \quad h'_n = H_n(\bar{a}) \quad \text{and} \quad l'_n = T_n(\bar{a})$$

the quantities δ'_n and γ'_n necessary for the describing of gravitational changes and inclinations are deduced the following way:

$$\delta'_n = \frac{h'_n - \frac{n+1}{2} k'_n}{2n+1}; \quad \gamma'_n = \frac{k'_n - h'_n}{2n+1}. \tag{14}$$

The dependence of δ'_n and γ'_n on the Earth's structure might be very important in solving practical problems, as in the equations describing gravitational changes and deflections of the vertical (PERTSEV, 1967)

$$\Delta g = \sum_{n=0}^{\infty} \delta'_n H_n(\Psi) \tag{15}$$

$$\Delta \xi = \frac{\partial}{\partial \Theta} \sum_{n=0}^{\infty} \gamma'_n H_n(\Psi) \tag{16}$$

δ'_n and γ'_n bear information on the inner structure of the Earth. In Eqs. (15) and (16) Ψ is the central angle; $H_n(\Psi)$ is the n-th harmonic in the expansion of the Earth's tide of height H on the spherical segment.

Computations were performed for the following five Earth models:

1. BULLEN's A model
2. MOLODENSKIY's (1953) model assuming homogeneity of the mantle and the following density distribution:
$$\frac{\varrho'}{g} = \frac{\varrho^2}{\lambda}.$$
3. BULLARD's (1957) model, with a somewhat displaced transient C layer in the mantle. (In BULLEN's model the relative boundaries of the C layer are 0.93 and 0.84, in the present model they are 0.94 and 0.80.) This model will be marked in the Tables as BULLARD 1.
4. Same as the BULLEN A model, but the near-surface density is decreased from 3.31 g/cm^3 to 3.20 g/cm^3. This model will be marked as BULLARD 2. (BULLARD 1957)
5. The density on the surface is significantly increased, with respect to the BULLEN A model: from 3.32 g/cm^3 to 3.70 g/cm^3. This model will be called BULLARD 3.

In the calculations GUTENBERG's velocity data were used. Since the phenomena described by means of the load numbers are expressed in infinite series form (Eqs. 15 and 16), it has been investigated how many terms of these series should be taken into account in cases of different spherical segments and different central angles Ψ. It had been found earlier (VARGA 1977) that for a $1^\circ \times 1^\circ$ segment some 3000 terms, while for a $0.1^\circ \times 0.1^\circ$ segment approximately 10^4 terms are needed.

Table I shows the values of the load numbers for the five Earth-models described above, while core-mantle boundary is being kept at 0.545 Earth radius. Due to the rapid decrease of the value of l'_n, this load number is not presented in Table I beyond $n=200$. Comparing the numerical values it is apparent that for all values of n the MOLODENSKIY model for homogeneous mantle deviates only slightly from the generally accepted BULLEN A model. The deviation is somewhat more significant in the case of the BULLARD 1 model, the displacement of layer C, however does not influence the value of the load numbers considerably. The same holds true in respect of the BULLARD 2 model. There is a significant deviation in the case of the BULLARD 3 model, and increasing with growing n. As a summary, it can be stated that the values of h'_n, k'_n and l'_n depend only slightly on the mantle structure, while the effect of the changes in surface density is reflected by these load numbers for higher values of n.

The dependence of he load numbers on the assumed physical conditions of the core-mantle boundary can be analysed by the boundary equations (10)–(12):

- the density distribution within the core can exert its influence by the factor γ appearing in Eq. (12). PERTSEV (1976) has shown that for $n \geqq 9$ this effect can be neglected;
- using relative boundaries of 0.55 and 0.54 in the computations, it was shown that the variation of the depth of core-mantle boundary affects significantly the results at small values of n, for $n \geqq 40$ however, this effect becomes negligible;
- the effect of the shear modulus within the core has been studied by taking $\mu_i = 10^{10}$ dyn/cm^2 and $\mu_i = 10^{11}$ dyn/cm^2 in Eq. (11). It was found that its effect—similarly to that of the core-mantle boundary—is considerable for small values of n but for $n \geqq 40$ it becomes negligible.

Thus, for increasing values of n the differences between the different models gradually increase. The dependence of the load numbers on the near-surface structural elements grows with increasing values of n and at the same time the effect of the physical characteristics of the core-mantle boundary decreases.

Table II presents the series of equations describing the values of δ'_n (of Eq. 14) derived from the load numbers for the different models by approximating the empirical values in the form of $\delta'_n = a \cdot n^b$. The statistical significance of this approximation is characterized by the coefficients of determinacy (r^2). A comparison of the equations also proves that the gravitational changes due to deformations do depend on the structure of the Earth.

Since the deformations due to loading, described by Eqs. (15) and (16), do not depend upon the individual values of δ'_n and γ'_n, but on their sum, by using the above described equations we have determined for the different Earth models the total gravity changes for $1^\circ \times 1^\circ$ segments by assuming a load corresponding to a water column of 1 cm height. Results are shown in Table III. It can be concluded that the deformations are not independent of the Earth's inner structure, first of all because of the ever increasing effect of the near-surface conditions at greater values of n. The effect due to the unknown features of the near-surface structures becomes even more pronounced in more detailed calculations (i.e. in case of segments smaller than $1^\circ \times 1^\circ$) due to the already mentioned slow convergence of the series (15), (16).

According to the above described ideas the exact study of deformations due to the tides of world oceans needs besides the set of accurate cotidal maps, describing the areal distribution of sea tides, the best possible approximation of the Earth's structure. The effect of this factor is even more important in the near-ocean regions, since in such areas segments less than $1^\circ \times 1^\circ$ should be used for the integral description of the total effects.

*

n	BULLEN A	MOLODENSKIY (1953)	BULLARD 1	BULLARD 2	BULLARD 3
2	$k' = -0.31260$	-0.31291	-0.30502	-0.31088	-0.31050
	$h' = -0.99680$	-1.00454	-0.98143	-0.98822	-0.99200
3	$k' = -0.19986$	-0.19990	-0.20308	-0.20063	-0.20061
	$h' = -1.04690$	-1.03192	-1.05201	-1.04134	-1.04130
4	$k' = -0.13575$	-0.13764	-0.14469	-0.13563	-0.14304
	$h' = -1.04040$	-1.05589	-1.07205	-1.04330	-1.04715
5	$k' = -0.10604$	-0.10844	-0.10803	-0.13903	-0.11220
	$h' = -1.06571$	-1.08208	-1.06605	-1.03296	-1.06031
6	$k' = -0.08649$	-0.08963	-0.09467	-0.08441	-0.08435
	$h' = -1.08600$	-1.10312	-1.12100	-1.07820	-1.10971
7	$k' = -0.08354$	-0.07980	-0.08670	-0.08201	-0.08141
	$h' = -1.18382$	-1.14434	-1.19211	-1.17263	-1.16852
8	$k' = -0.07991$	-0.07828	-0.08041	-0.07817	-0.08221
	$h' = -1.26666$	-1.24100	-1.25227	-1.26489	-1.20671
9	$k' = -0.07320$	-0.07490	-0.07432	-0.07216	-0.07671
	$h' = -1.30793$	-1.30787	-1.29742	-1.31248	-1.30103
10	$k' = -0.06952$	-0.06912	-0.07021	-0.06877	-0.07391
	$h' = -1.36561$	-1.33927	-1.35104	-1.37326	-1.30762
15	$k' = -0.05251$	-0.06357	-0.05953	-0.05250	-0.06071
	$h' = -1.52073$	-1.69121	-1.62567	-1.52072	-1.51472
20	$k' = -0.04750$	-0.05277	-0.04675	-0.05314	-0.05631
	$h' = -1.73885$	-1.83111	-1.69121	-1.87827	-1.76240
25	$k' = -0.04231$	-0.04438	-0.04401	-0.04415	-0.04415
	$h' = -2.01319$	-2.11173	-2.09419	-2.10071	-2.10100
50	$k' = -0.02341$	-0.02464	-0.02458	-0.02465	-0.02785
	$h' = -2.25200$	-2.37042	-2.36461	-2.36652	-2.67922
100	$k' = -0.01297$	-0.01371	-0.01375	-0.01374	-0.01623
	$h' = -2.68621$	-2.83931	-2.84761	-2.84561	-3.36121
200	$k' = -0.00705$	-0.00749	-0.00756	-0.00753	-0.00934
	$h' = -3.06792$	-3.25672	-3.29150	-3.27801	-4.02641
500	$k' = -0.00345$	-0.00366	-0.00373	-0.00371	-0.00483
	$h' = -3.69261$	-3.92586	-3.99971	-3.97083	-5.16921
1,000	$k' = -0.001978$	-0.00210	-0.00216	-0.00214	-0.00289
	$h' = -4.12433$	-4.39300	-4.50571	-4.46194	-6.04410
5,000	$k' = -0.000447$	-0.00048	-0.00050	-0.00049	-0.00078
	$h' = -4.62752$	-5.01870	-5.26519	-5.16882	-8.16821
10,000	$k' = -0.000246$	-0.00026	-0.00028	-0.00027	-0.00046
	$h' = -5.09842$	-5.56001	-5.88921	-5.75871	-9.65031
2	$l' = 0.02738$	0.02609	0.02771	0.02507	0.02723
3	$l' = 0.07343$	0.07218	0.07342	0.07280	0.07282
4	$l' = 0.06109$	0.06177	0.06613	0.06007	0.06313
5	$l' = 0.04781$	0.04901	0.04882	0.05140	0.04986
6	$l' = 0.03546$	0.03724	0.04172	0.03998	0.04340
7	$l' = 0.03557$	0.03050	0.03831	0.03709	0.03791
8	$l' = 0.03451$	0.03183	0.03473	0.03245	0.03352
9	$l' = 0.02974$	0.03032	0.03061	0.02828	0.02911
10	$l' = 0.02773$	0.02614	0.02840	0.02650	0.02904
15	$l' = 0.01922$	0.02889	0.02490	0.02331	0.02292
20	$l' = 0.01645$	0.02279	0.01573	0.01598	0.02430

n	BULLEN A	MOLODENSKIY (1953)	BULLARD 1	BULLARD 2	BULLARD 3
25	$l' = 0.01094$	0.01321			
50	$l' = 0.00206$	0.00277			
100	$l' = 0.00071$	0.00078			

Table I. Load numbers for different Earth models
I. táblázat. Terhelési számok különböző modellek esetében

Bullen A model
$\delta'_n = 0.5849 \cdot n^{-0.8674}$
$r^2 = 0.9989$

Molodenskiy model
$\delta'_n = 0.5964 \cdot n^{-0.8601}$
$r^2 = 0.9980$

Bullard 1. model
$\delta'_n = 0.5658 \cdot n^{-0.8484}$
$r^2 = 0.9990$

Bullard 2. model
$\delta'_n = 0.5779 \cdot n^{-0.8531}$
$r^2 = 0.9990$

Bullard 3. model
$\delta'_n = 0.4694 \cdot n^{-0.7756}$
$r^2 = 0.9994$

Table II. Equations approximating the values of δ'_n describing gravitational changes due to the deformations and the corresponding coefficients of determinacy (r^2)
II. táblázat. A deformáció keltette gravitációs változásokat leíró δ'_n értékeket közelítő egyenletek és a megfelelő determináltsági együtthatók (r^2)

Table III

Model	n	$\Psi = 2°$	$\Psi = 4°$	$\Psi = 8°$	$\Psi = 10°$
Bullen A	3000	−0.0011096	−0.0005075	−0.0002316	−0.0001785
Molodenskiy	3000	−0.0011485	−0.0005226	−0.0002373	−0.0001826
Bullard 1.	3000	−0.0011160	−0.0005036	−0.0002270	−0.0001741
Bullard 2.	3000	−0.0011290	−0.0005112	−0.00023109	−0.0001775
Bullard 3.	3000	−0.0010722	−0.0004594	−0.0001972	−0.0001489
Bullard 3.	4000	−0.0010721	−0.0004601	−0.0001970	−0.0001491

Table III. Gravitational effect in microgals due to the deformation caused by the pressure of a water column of $H = 1$ cm height exerted upon a spherical segment of $1° \times 1°$, as a function of the central angle Ψ.
III. táblázat. $H = 1$ cm magasságú vízoszlop $1° \times 1°$ szferikus szegmensre gyakorolt nyomása okozta deformáció következtében fellépő gravitációs hatás microgalban Ψ centrális távolság függvényében

MOLODENSKIY, JR. (1977) has found theoretically a simple analytical relationship between the load number k'_n and the LOVE numbers k_n, h_n. According to him:

$$k'_n = k_n - h_n.$$

We have checked the validity of this formula for the BULLEN A model, in order to get an indirect estimation of the reliability of our calculations. The results of the two calculations have shown a fair agreement. The deviations increase with growing order of n, their average value being one tenth per cent.

References

BULLARD, E. C., 1957: The density within the Earth. Verhandel. Ned. Geol. Mijubouwk. Genoot., Geol. Ser. 18.

VARGA, P., 1974: Dependence of the Love numbers upon the inner structure of the Earth and comparison of theoretical models with results of measurements. Pageoph, vol. 112, Birkhäuser Verlag, Basel

VARGA, P., 1977: Analysis of periodical gravitational variations of non-lunisolar origin. Paper presented at the 8th International Symposium on Earth Tides, Bonn

MOLODENSKIY, M. S., 1953: Elastic tides, free oscillation and some questions of the structure of the Earth. Transactions of the Institute of Geophysics of the Academy of Sciences of the USSR. Issue No. 19. (146.) (in Russian)

MOLODENSKIY JR., S. M., 1977: About connection of Love number with loading coefficients. Physics of the Earth (Fizika Zemli) No 3. (in Russian)

PERTSEV, B. P., 1967: Estimation of the influence of the oceanic tides on Earth tide in points situated far from the oceans. From "Earth tides and internal structure of the Earth", Nauka, Moscow (in Russian)

PERTSEV, B. P., 1976: Influence of the near zone tides on the Earth tide observations. Physics of the Earth (Fizika Zemli) No. 1. (in Russian)

VARGA PÉTER

A FÖLD KÜLSŐ ERŐK OKOZTA STATIKUS DEFORMÁCIÓINAK KAPCSOLATA A FÖLDSZERKEZETTEL

Öt különböző földmodell, valamint változó határfeltételek esetében meghatároztuk a terhelések következtében fellépő deformációkat leíró terhelési számok h'_n, k'_n és l'_n értékeit és ezeknek a gravitációs és horizontális komponensek esetében érvényes kombinációit $n=2$-től $n=10000$-ig. Az elvégzett számítások célja: megvizsgálni azt, hogy radiálisan inhomogén Földet feltételezve, az egyes bolygószerkezeti elemek, milyen mértékben befolyásolják a fellépő rugalmas deformációkat jellemző terhelési számok értékét. Megállapítottuk, hogy a terhelési számok nagyságrendjének növekedésével az egyes földmodellek között eltérések jelentkeznek, így például a felszínhez közelebb fekvő hatók szerepe növekszik. A deformációk számításához felhasznált földmodelltől függően a számítások eredménye bizonyos mértékig változik, azaz a Föld statikus deformációinak nagysága bolygónk szerkezetével kapcsolatot mutat.

П. ВАРГА

СВЯЗЬ СТАТИЧЕСКИХ ДЕФОРМАЦИЙ ЗЕМЛИ, ВЫЗЫВАЕМЫХ ВНЕШНИМИ СИЛАМИ, С СТРОЕНИЕМ ЗЕМЛИ

Для пяти различных моделей строения Земли и при переменных граничных условиях были определены величины h_n, k_n и l_n нагрузки, описывающие деформации, возникающие на воздействие нагрузок, а также их комбинации, действительны для гравитационных и горизонтальных составляющих, от $n = 2$ до $n = 10\,000$.

Целью проведенных вычислений было изучение степени влияния отдельных элементов строения планеты на величины факторов нагрузки, характерных для возникающих упругих деформаций, исходя из предположении о радиально неоднородном строении Земли. Обнаружено, что с увеличением порядка величин нагрузок, появляются различия между отдельными моделями, так напр., увеличивается значение роли возмущающих тел, залегающих ближе к поверхности. В зависимости от модели, использованной для вычисления деформации, результаты вычислений в определенной мере изменяются, т. е. величина статических деформаций Земли связана с строением нашей планеты.

Magyar Állami Eötvös Loránd Geofizikai Intézet
GEOFIZIKAI KÖZLEMÉNYEK
25

DETERMINATION OF LAYER PRESSURES USING INTERVAL VELOCITIES

P. ZSELLÉR*

1. Introduction

It is advantageous at the planning of well-drillings to know in advance the expected changes in layer pressures. The delineation of the so-called "abnormal pressure" zones is especially important. In these zones the pressure of pore liquid is greater than the hydrostatic pressure.

Without going deeply in discussing the formation of abnormal pressures let us examine which physical parameters change in the abnormal pressure zones.

During the normal sedimentation and compaction process the surplus liquid is squeezed out from the layers, and the compacted rock granules support the grains above them. The pressure of liquid at a given depth depends only on the height of liquid column and on the density of the liquid. This pressure is equal to the hydrostatic pressure.

Occasionally at certain places sediments of small grain-size and of low permeability are deposited. This layer might trap the pore-liquid into the underlying incompletely compacted layers. As time passes by these layers are sinking deeper and deeper; the top-layers are loading them more and more while the trapped liquid does not allow this layer to be compressed.

In cases like this the weight of the overlying layers does not load the rock grains but the trapped liquid. Thus the pressure built up in the liquid will be greater than hydrostatic pressure. A fraction of the pressure due to the overlying layers must also be added to the hydrostatic pressure. This is called the abnormal pressure.

The physical parameters of rocks in zones of abnormal pressure differ from those in normal surroundings. As the trapped liquid does not allow the layer to be compressed the rock matrix will be less compact, i.e. more porous.

This is the physical basis of predicting the presence of abnormal pressure zones. From among the numerous methods only those will be dealt with which are based on the relationship between porosity and wave velocity.

In bore-hole technology acoustic well-logging curves have been used since long to predict abnormal pressures. Let us examine layers consisting of identical rock grains at various depths. The wave velocity in layers is described by Wyllie's formula:

$$\frac{1}{V} = \frac{\Phi}{V_f} + \frac{1-\Phi}{V_{ma}},$$

where

Φ is porosity,

* Geophysical Prospecting Enterprise of the Hungarian Oil and Gas Trust, Budapest
Manuscript received 16. 4. 1977

V_f is the wave velocity in the pore-liquid,
V_{ma} is the wave velocity in the rock matrix.

The wave velocity in the matrix depends on the elastic constants of the material and on the stress conditions. Velocity changes with depth.

It can be shown exprerimentally that in rocks of identical type—for example in marls—the wave velocity increases exponentially with depth. This is proved by several well-known examples described in the literature.

In other words, if the logarithm of the velocities for rocks of identical type is plotted as a function of depth, the values should lie along a straight line (Fig. 1). This straight line is called the normal *compaction trend* of the given rock type. The slope of the line depends on the compaction conditions of the region.

Porosity systematically increases in zones of abnormal pressure, leading to a decrease in wave velocity. Thus, in zones of abnormal pressure, the observed velocities do not fit the normal compaction trend, velocities are systematically shifted towards smaller values. From the degree of this shift the magnitude of abnormal pressure may be deduced.

In well-logging practice the presence of a sealing layer above the abnormal pressure zone—being itself partially under abnormal pressure—is used for the detection of the latter. By taking repeated well-logging readings during drilling this transitional zone can be recognized.

Instead of frequent well-logging it is more convenient to use seismic velocity analysis, but the poor resolution of the seismic reflection method may cause some concern. At well-logging, using different types of logs, layers of identical rock types can be identified. In practice shales or marls are used to predict abnormal pressures.

It cannot be expected from seismics to provide velocity information for each layer, only for selected depth intervals. The so-called interval velocity gives the average velocity of the wave passing through the depth interval.

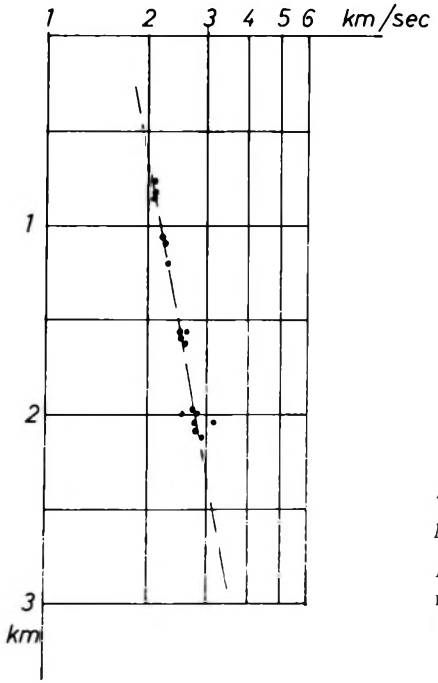

Fig. 1 Wave velocities in shales

1. ábra. Hullámterjedési sebességek márgás rétegekben

Рис. 1. Скорости распространения упругих колебаний в мергельных пластах

This is why in case of seismically determined velocities one cannot speak of the compaction trend of a certain rock type—for example of shales. However—as it will be shown in the next sections—the change in velocity caused by abnormal pressures can be recognized on the interval velocity curves.

In what follows we first introduce a method for seismic velocity determination. Then, an example will be presented to illustrate the application of interval velocities to predict abnormal pressures.

2. Description of the Velocity Analysis

The velocities are determined from multiple coverage reflection data. In order to use this method the following supplementary input data are required:

(i) exact static corrections,

(ii) an approximate stacking velocity function.

First the static and dynamic corrections are carried out and the input traces are sorted, according to common depth points.

The second step is to select the appropriate time windows. This is accomplished by producing first a reference trace at each depth point by stacking the *CDP* traces. It is supposed that only those parts of the section are worth for any further study where there are good reflections even on the rough stacking section processed by the preliminary velocity function. As next step, the local maxima of the reference trace are picked. The time values corresponding to these local maxima will be denoted by t_0 in the further examinations.

Each *CDP* trace is examined to see how similar they are to the reference trace around the selected t_0 values. For comparison the following coherence function is used:

$$M(\tau) = \frac{\sum_{t=t_0-DT}^{t_0+DT} |x(t)+y(t+\tau)|}{\sum_{t=t_0-DT}^{t_0+DT} |x(t)| + \sum_{t=t_0-DT}^{t_0+DT} |y(t)|}.$$

This function differs from the well-known semblance function, only in using the average of absolute values instead of energies; thus accelerating the calculation process.

At the same time it is determined how much the respective trace should be shifted in time with respect to the reference trace to achieve maximum similarity.

The procedure at a *CDP* point of a six-fold coverage profile is shown in Fig. 2. In the calculation of the $M(\tau)$ function the sampling interval $\Delta\tau$ was selected as twice the original. The exact location of the maximum of $M(\tau)$ was determined by fitting a parabola to the largest value of the sampled function, and two of its neighbouring points. The peak of the parabola is considered as the maximum of the $M(\tau)$ function. Detailed illustration of the method is shown in Fig. 3.

To the time-shift thus obtained a weight, characterizing its reliability is assigned. This is determined from the maximum value of $M(\tau)$. The following should be considered when determining this weight:

$M_{\max}=1$, if $x(t)=y(t)$

$M_{\max}=0$, if $x(t)=-y(t)$

$M_{\max}=0.5$, if $x(t)$ and $y(t)$ are uncorrelated (the case $x(t)\equiv 0$ and $y(t)\equiv 0$ is exluded).

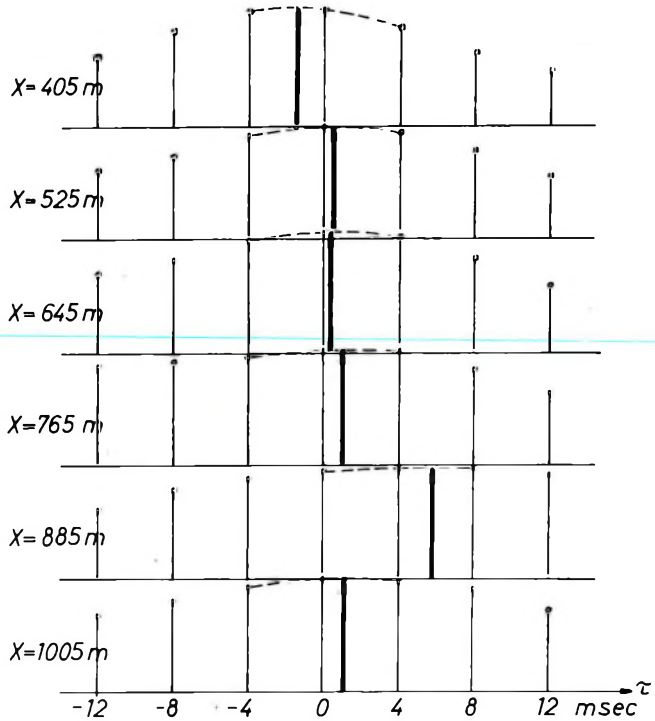

Fig. 2 $M(\tau)$ similarity graphs of traces belonging to a common depth point. Values of x denote shotpoint–geophone distances. Arrows show the values of maxima of the graphs

2. ábra. Egy közös mélységponthoz tartozó csatornák $M(\tau)$ hasonlósági függvényei. Az x értékek a csatornák robbantópont–geofonpont távolságát jelentik. A nyilak a függvények maximális értékét jelzik

Рис. 2. Функции подобия $M(\tau)$ трасс, относящихся к общей глубинной точке. Величиных соответствуют расстоянию от пункта взрыва до сейсмоприемника. Стрелками отмечены максимальные величины функций

Next, we compute the sum of the weights at each point. Those will be considered as reflection-like points for which the sum of the weights exceeds a given threshold.

At reflection-like points the *RNMO* values should be determined. It is carried out by fitting a parabola to the previously defined shift values, as a function of offset, using the least squares method.

The respective shift values are taken into account in proportion to the corresponding weights.

Having fitted the parabola, the *RNMO* and t_0 values of the reflection can be obtained. The corrected *NMO* function will be:

$$NMO(t_0) = RNMO(t_0) + \overline{NMO}[t_0 + RNMO(t_0)]$$

where $\overline{NMO}$ is the preliminary dynamic correction function.

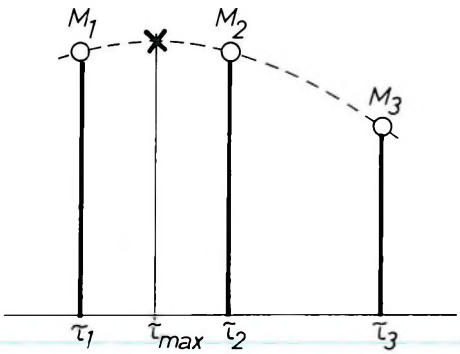

$$\tau_{max} = \tau_2 + \frac{\tau_2 - \tau_1}{2} \cdot \frac{M_1 - M_3}{M_1 + M_3 - 2M_2}$$

Fig. 3 Fitting a parabola through three points. The differences between τ_1, τ_2, τ_3 are constant ($\Delta\tau$)

3. ábra. Három ponton átmenő parabola illesztése τ_1, τ_2, τ_3 között egyforma $\Delta\tau$ különbség van

Рис. 3. Согласование параболы, проходящей через три точки. Разность $\Delta\tau$ между τ_1, τ_2, τ_3 одинакова

Next the *CDP* summation along the *RNMO* curve is carried out at the calculated t_0 points. The sum obtained will be considered as the amplitude of the corresponding reflection. Thus, the following three values are assigned to each reflection-like point: t_0, *NMO* and the amplitude.

Figure 4 shows a 600% stacking section, the corresponding reflection-like points are shown in Fig. 5. Shading of the points is proportional to their amplitude. On the right-hand side of the figure there are histograms of stacking velocities of the reflections observed on the section versus t_0.

The next step is to select those reflection-like points which could be interconnected into seismic horizons. The following criteria were observed at selecting these points:

(i) Reflection-like points should fit into some appropriate stacking velocity function. This function should not have rapid changes either in time or along the section.

(ii) Reflection-like points should be observable through consecutive *CDP* traces. More precisely, for any reflection-like point there should exist a pair of points at the neighbouring *CDP* traces such that the deviation in their t_0, *NMO* and amplitude values should not be greater than some fixed threshold. These points then may be connected into seismic horizons.

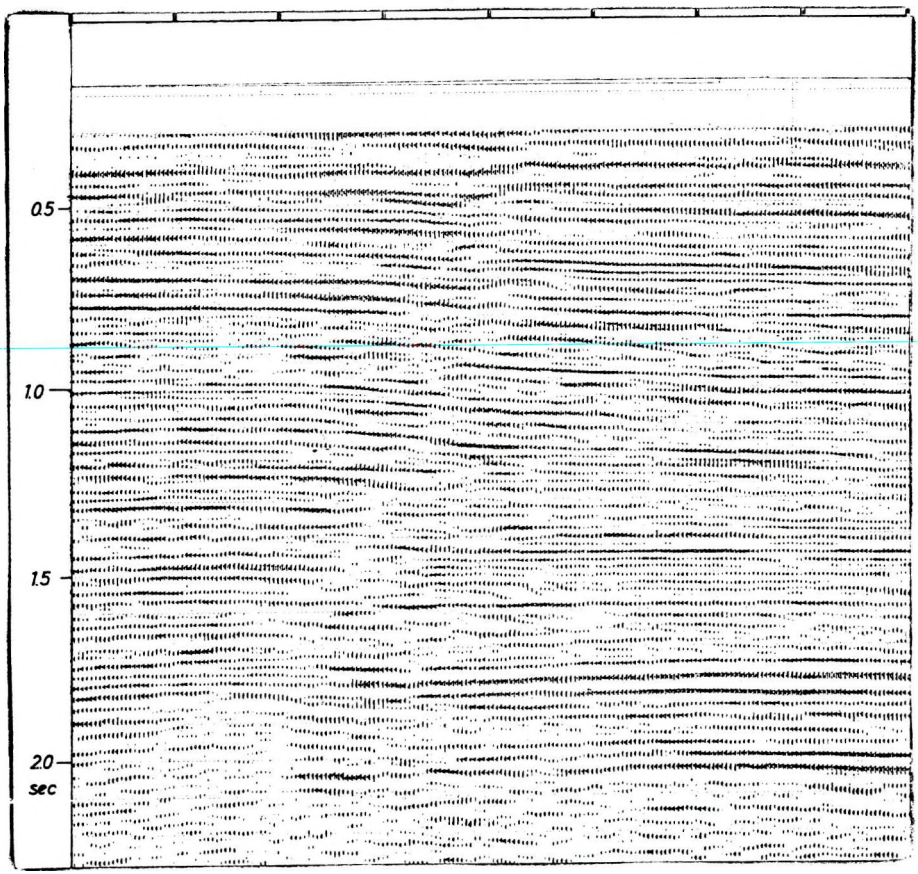

Fig. 4 600%-coverage time section

4. ábra. 600%-os fedésű időszelvény

Рис. 4. Временный разрез с перекрытием в 600%

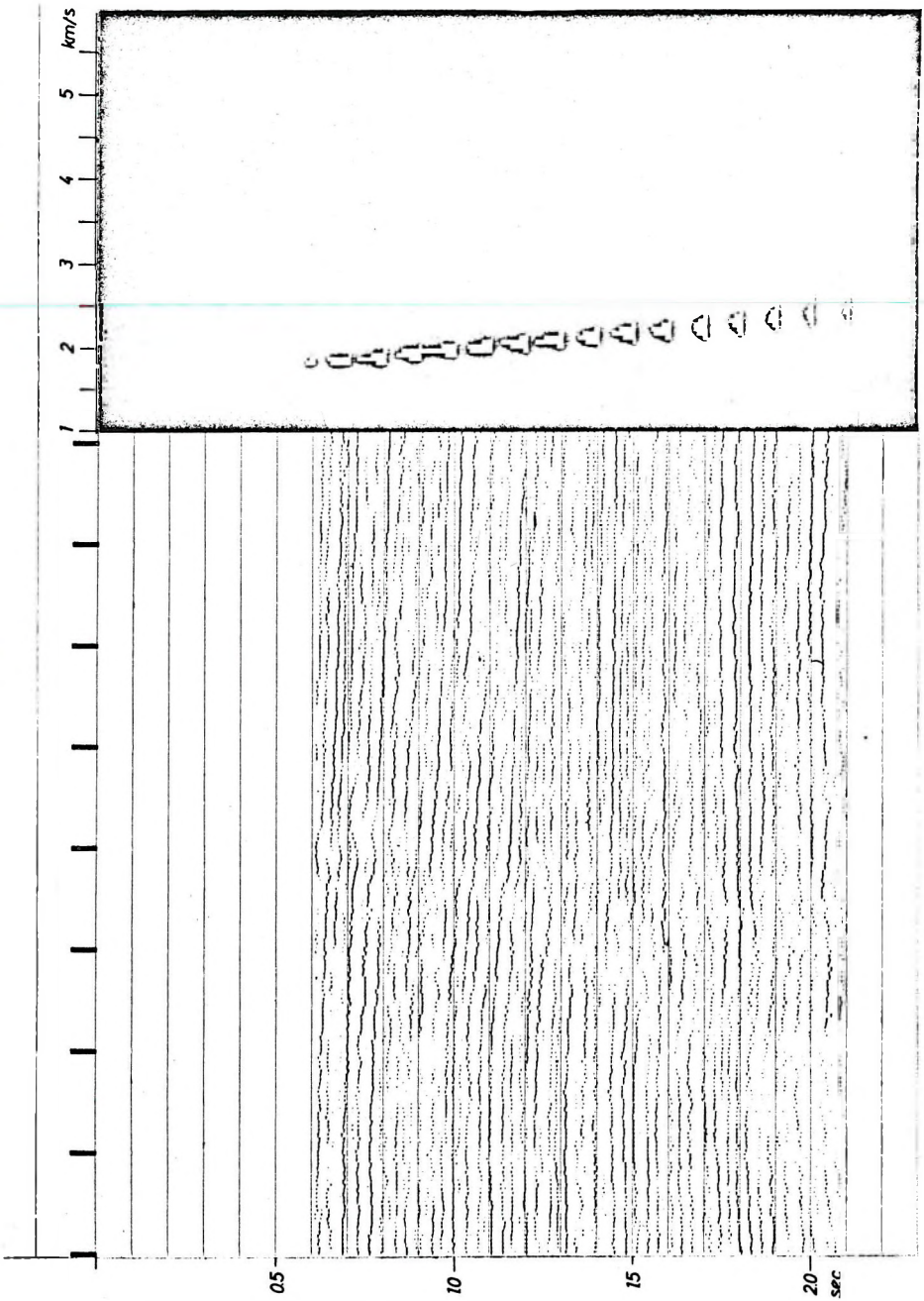

Fig. 5 Reflection-like points of the section shown in Fig. 4. On the right-hand side of the figure are histograms of the stacking velocity values

5. ábra. A 4. ábrán látható időszelvény reflexiószerű pontjai; az ábra jobb oldalán a stacking-sebesség értékek előfordulási gyakorisága látható

Рис. 5. Пункты характера отражения на временном разрезе, представленном на рис. 4. В правой части рисунка указана повторяемость величин скоростей по накоплению

(iii) Between the subsequent horizons we can determine the interval velocity. The calculated interval velocities should match the velocity trend of the area.

Figure 6 shows the stacking velocities corresponding to the reflections chained into horizons. Each velocity value is produced by joining 8 points. The interval velocities of the same section are shown on Fig. 7.

The main advantage of the described velocity analysis is its speed of calculation. By carefully preselecting the areas of investigations, eight or ten times less computer time is required than for the traditional velocity determination methods. This enables mass application of this method which is indespensable at investigations of layer pressures.

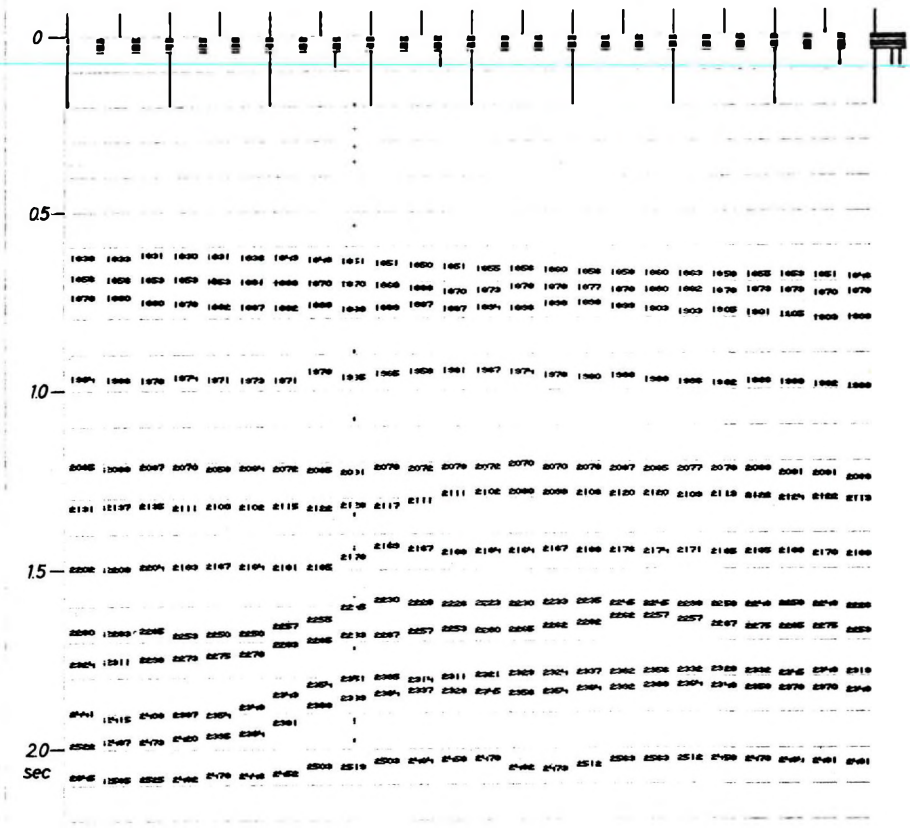

Fig. 6 Stacking velocity section. Velocity values written along the horizons represent the averages of 8 consecutive depth points

6. ábra. Stacking-sebesség szelvény; a horizontok mentén kiírt sebességértékek 8–8 mélységpont átlagából készültek

Рис. 6. График скоростей по накоплению; величины скоростей, указанные на горизонтах, получены по осреднению данных для 8 глубинных точек

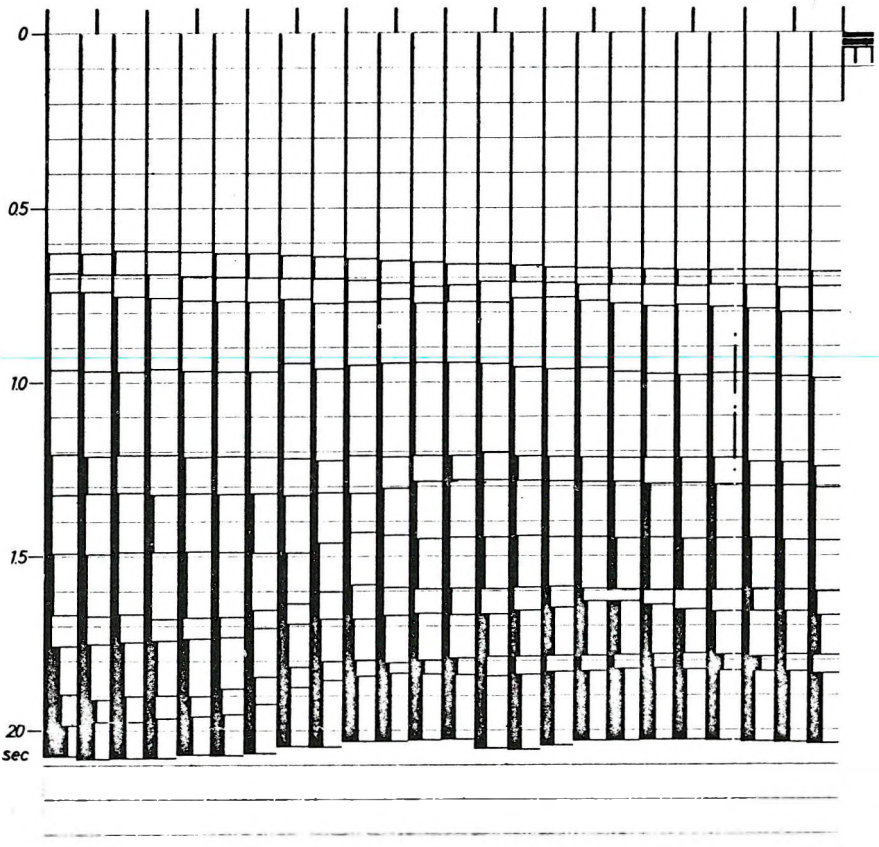

Fig. 7 Interval velocity section

7. ábra. Intervallum-sebesség szelvény

Рис. 7. График интервальных скоростей

3. Example for Predicting Anomalous Layer Pressures

As it has been already discussed, the following tasks must be solved: determination of the interval velocity function versus depth, plotting in semi-logarithmic scale and determination of the normal compaction trend. Next this plot should be examined whether any deviation from the trend exists. The magnitude of abnormal pressure can be calculated from the extent of the deviation.

In our example the interval-velocity function was calculated by horizontal averaging in order to increase reliability (Fig. 7).

In well-logging, instead of interval velocity its reciprocal, the interval transit time is used. Therefore in the followings we also switch over to the use of interval transit times. The averaged transit time curve is shown on Fig. 8.

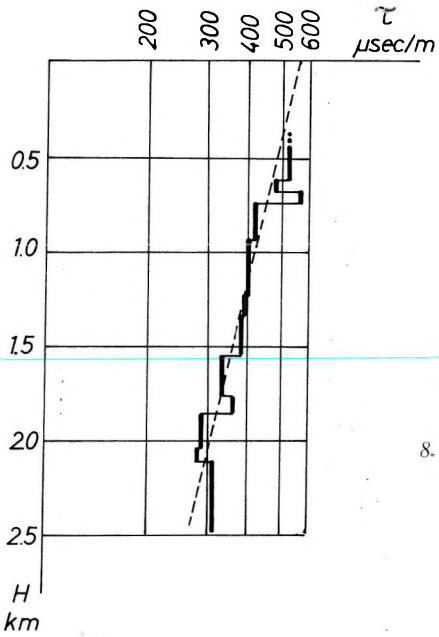

Fig. 8 Interval transit time graph for the section shown in the previous figures. Dashed line represents the normal compaction trend characterizing the area of investigation

8. ábra. Az előző ábrákon látható szelvény intervallum-áthaladási idő-függvénye; a szaggatott vonal a területre jellemző kompakciós trend

Рис. 8. Функция кривой, представленной на предыдущих рисунках от времени перехода через интервалы; пунктиром отмечен тренд компакции, характерный для района

The next task is to determine the normal compaction trend. As it was already mentioned it is not possible to separate the individual layers by the seismic method, so it cannot be stated about any point of the graph that it represents the velocity of a certain rock type.

According to the published values of rock velocities it can be taken for granted that from among the sedimentary rocks:

— the wave velocity is the lowest in shales and marls;
— the highest in carbonates;
— the velocity of sandstones is inbetween that of the shales and carbonates.

Wave velocities as measured by the seismic method always relate to a whole series of layers. It can be assumed that the velocity is proportional to the shale—sand—carbonate content in the corresponding depth range. Thus, in case of the graph shown in Fig. 8, the normal compaction trend of the shales is best approximated if the straight line is fitted to the points of lowest velocities.

For determining the seismic velocity function the straight line should be fitted to the velocity curve as closely as possible. This trend is represented by a dashed line in Fig. 8.

Naturally a normal compaction trend drawn from a single velocity curve would be unreliable. In our example results of previous investigations being at disposal were utilized as well. Unfortunately, this simple method of drawing the compaction trend is burdened by a lot of biased errors. Further investigations in this field will decrease the number of such errors.

It can be seen from Fig. 8. that the velocity curve deviates from the inscribed straight line at the shallowest and greatest depths. As for shallow depths, this can be explained by noticing that the compaction is not of the same degree as in case of the older layers. The deviation observed at a depth of 2500 m is believed to be due to abnormal pressure.

Let us draw an auxiliary straight line fitting to the velocities corresponding to the depths of about 2500 meters. The two straight lines are shown in Fig. 9. From the difference of the two lines the amount of abnormal pressure can be estimated. This estimation is based on the so-called method of equivalent depths, shortly described as follows.

As an example, let us try to estimate the pressure at a depth H_2, shown in Fig. 9. The depth corresponding to that velocity on the normal compaction trend which is equal to the velocity on the abnormal pressure line of depth H_2, will be denoted as H_1. It may be assumed that the velocities are the same because the stresses acting upon the rock matrices are nearly the same.

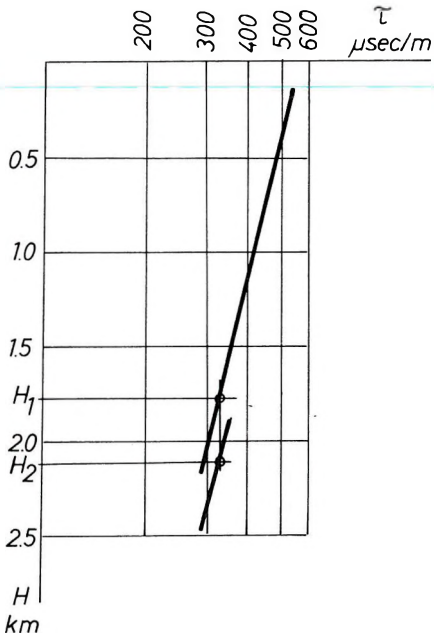

Fig. 9 Deviation between the normal compaction trend and the trend characterizing the zone of abnormal pressures

9. ábra. A normál kompakciós trend és a túlnyomásos rétegre jellemző trend eltérése

Рис. 9. Отклонение нормального тренда компации от тренда, характерного для пласта с передавлением

The pressure exerted by the overlying sediments is balanced by the stresses in the rock matrix and the pressure of the pore-liquid:

$$S = \sigma_{\text{matrix}} + p_{\text{liquid}},$$

where

S is the pressure exerted by the overlying sediments;
σ_{matrix} is the stress in the rock-matrix;
p_{liquid} is the pressure of the pore-liquid.

The pressure of the pore-liquid at depth H_1 is equal to the hydrostatic pressure. Consequently, the following equation holds true:

$$\sigma_{\text{matrix}}(H_1) = [S'(H_1) - p'(H_1)]H_1,$$

where dashes represent the gradients with respect to depth.

The pressure at depth H_2 is

$$p(H_2) = p'(H_2)H_2 = S'(H_2)H_2 - \sigma_{\text{matrix}}(H_2).$$

If we assume that $\sigma_{\text{matrix}}(H_1) = \sigma_{\text{matrix}}(H_2)$:

$$p'(H_2) = S'(H_2) - [S'(H_1) - p'(H_1)]\frac{H_1}{H_2},$$

where

$p'(H_1)$ is the hydrostatic gradient at depth H_1 characteristic to the are;
$S'(H)$ is the pressure gradient in the overlying sediments.

If the above-mentioned factors are known, the pressure can be calculated as:

$$p(H_2) = \left\{S'(H_2) - [S'(H_1) - p'(H_1)]\frac{H_1}{H_2}\right\}H_2.$$

Instead of using pressures or pressure gradients in the above formulae some prefer to use the equivalent mud density. This expresses that the hydrostatic pressure of what density mud would balance the pressure of the pore-liquid at a given depth.

The solid line shown in Fig. 10 is the equivalent mud density curve calculated from the given velocity function. For comparison purposes the actual mud densities used in neighbouring drillings were also plotted (as dashed areas).

The pressure values obtained by seismics clearly indicate the place of pressure change. As seismic measurements precede drilling activities in time, the information thus obtained may be used at the planning of drillings. These preliminary informations, supplemented for example by monitoring the drilling velocity, may greatly increase the safety of balanced drillings.

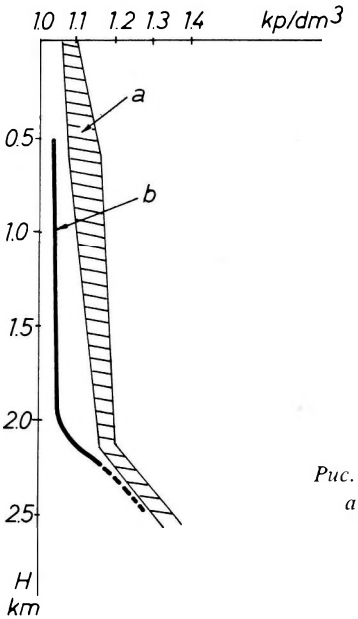

Fig. 10 Comparison of mud densities from actual drillings of the area (*a*) and the equivalent mud density graph obtained from velocity analysis (*b*)

10. ábra. Iszapfajsúlyok összehasonlítása. *a)* a terület fúrásaiban használt iszapfajsúlyok, *b)* a sebességvizsgálatokból meghatározott ekvivalens iszapfajsúly-függvény

Рис. 10. Сопоставление удельных весов глинистого раствора; *а)* удельный вес глинистого раствора, применявшегося в екважинах района; *б)* эквивалентная кривая удельного веса глинистого раствора, определенного по анализу скоростей

BIBLIOGRAPHY

MATTHEWS, W. R.–MCCLENDON, R. T.–SOUCEK, C. H.: New Prediction Method Spots Abnormal Pressures. World Oil. April, 1973.

REINOLDS, E. B.–TIMKO, D. J.–ZAINER, A. M.: Potential Hazards of Acoustic-log Shale Pressure Plots. Journal of Petroleum Technology, September, 1973.

AUD, B. W.: Abnormal Pressure Zones Can be Predicted by Seismic Data. World Oil, August, 1974.

ZSELLÉR PÉTER

RÉTEGNYOMÁS MEGHATÁROZÁSA INTERVALLUM-SEBESSÉGEK FELHASZNÁLÁSÁVAL

Az utóbbi években a reflexiós szeizmikus kutatásban egyre nagyobb teret hódítanak a litológiai vizsgálatok. Ezek közé tartozik az ún. túlnyomásos zónák előrejelzése sebességvizsgálatok alapján.

A litológiai vizsgálatok megbízható sebességadatokat igényelnek. Ez csak úgy érhető el, ha a sebességvizsgálatokat nagy tömegben tudjuk végezni.

A cikkben bemutatunk egy reflexiódetektáláson alapuló sebességmeghatározási módszert, melynek gépidőigénye kb. tizedrésze a szokásos összegzéses sebességmeghatározási eljárások gépidejének. Ez lehetővé teszi a módszer nagy tömegű alkalmazását.

A cikk második részében bemutatunk egy példát a túlnyomásos zónák kimutatására, az ismertetett sebességmeghatározás alkalmazásával.

П. ЖЕЛЛЕР

ОПРЕДЕЛЕНИЕ ПЛАСТОВОГО ДАВЛЕНИЯ С ИСПОЛЬЗОВАНИЕМ ИНТЕРВАЛЬНЫХ СКОРОСТЕЙ

За последние годы в сейсморазведочных работах МОВ все большее значение приобретают литологические исследования. Сюда входит и предсказание так называемых зон передавления по анализу скоростей.

Литологические исследования требуют наличия достоверных данных о скоростях. Это может достигаться только при массовом проведении анализов скоростей.

В настоящей работе описывается метод определения скоростей, основывающийся на прослеживании отражений, потребность которого в машинном времени прибл. в десять раз меньше по сравнению с машинным временем, требующимся для стандартных методов определения скоростей по способу суммирования. Это позволяет использовать метод для массового определения скоростей.

Во второй части работы приводится пример выделения зон передавления с использованием предлагаемого метода.

Magyar Állami Eötvös Loránd Geofizikai Intézet
GEOFIZIKAI KÖZLEMÉNYEK
25

SOME NOTES ON A PROBLEM OF TREITEL AND WANG

G. KORVIN*

In a recent paper TREITEL and WANG (1976) call attention to the fact that the autocorrelation matrices, used for the time-domain design of deconvolution filters, are in certain cases ill-conditioned. They also present an interesting example, where the solution to such an ill-conditioned system of equations leads to rather different filter points, on different computers.

To measure the condition-number of autocorrelation matrices they use the ratio

$$P = \frac{|\lambda_{\max}|}{|\lambda_{\min}|}, \tag{1}$$

where $\lambda_{\max}$ and $\lambda_{\min}$ are the largest and smallest eigenvalues of the autocorrelation matrix (see e.g. WESTLAKE, 1968).

On p. 318 of their paper the authors are posing the question, whether there is a simple geological-geophysical explanation for the ill-conditioned behaviour of the autocorrelation matrices.

In what follows it will be shown that, in case of autocorrelation matrices, the condition-number (1) has a simple physical meaning.

If we denote by x_n the sampled values of a seismic trace, the autocorrelation matrix, corresponding to this trace is

$$R = \begin{bmatrix} r_0 & r_1 & \dots & r_m \\ r_1 & r_0 & \dots & r_{m-1} \\ \vdots & & & \\ r_m & r_{m-1} & \dots & r_0 \end{bmatrix}$$

where r_k is defined by the expectation

$$r_k = \langle x_n x_{n+k} \rangle.$$

Let us first observe, that for any stationary time-series x_n the matrix R is *positive semi-definite*, i.e. for an arbitrary vector

$$(u_0, u_1, u_2, \dots, u_m); \qquad \sum_{i=0}^{m} u_i^2 \neq 0$$

we have

$$\sum_{k=0}^{m} \sum_{l=0}^{m} r_{k-l} u_k u_l \geqq 0. \tag{2}$$

* Hungarian Geophysical Institute 'Roland Eötvös', Budapest
Manuscript received 21. 8. 1978

Indeed, let us consider the vector $(u_0, u_1, \ldots, u_m)$ as a digital filter and apply it to the series of data x_n. The mean energy E of the resulting time-series y_n can be expressed as

$$E = \langle y_n^2 \rangle = \left\langle \left(\sum_{k=0}^{m} u_k x_{n-k} \right)^2 \right\rangle = \left\langle \sum_{k=0}^{m} \sum_{l=0}^{m} u_k u_l x_{n-k} x_{n-l} \right\rangle =$$

$$= \sum_{k=0}^{m} \sum_{l=0}^{m} u_k u_l \langle x_{n-k} x_{n-l} \rangle = \sum_{k=0}^{m} \sum_{l=0}^{m} r_{k-l} u_k u_l$$

which, since the expected energy is obviously non-negative, proves the positive semi-definiteness of matrix R. The formula

$$\langle y_n^2 \rangle = \sum_{k=0}^{m} \sum_{l=0}^{m} r_{k-l} u_k u_l \tag{3}$$

expressing the expected energy of a filtered trace will also be referred to later.

Let us now recall that the *smallest* and *largest* eigenvalues of an arbitrary positive semidefinite matrix $A = (a_{ij})_0^m$ can be characterized as smallest and largest values assumed on the $(m+1)$-dimensional unit sphere by the quadratic form

$$\sum_{i=0}^{m} \sum_{j=0}^{m} a_{ij} x_i x_j$$

i.e.:

$$\lambda_{\min} = \min_{\sum_{i=0}^{m} x_i^2 = 1} \sum_{i=0}^{m} \sum_{j=0}^{m} a_{ij} x_i x_j \tag{4}$$

$$\lambda_{\max} = \max_{\sum_{i=0}^{m} x_i^2 = 1} \sum_{i=0}^{m} \sum_{j=0}^{m} a_{ij} x_i x_j \tag{5}$$

(this characterization is due to Courant and Fischer, see BELLMAN 1960, Section 7; or BECKENBACH and BELLMAN 1961, Section II.)

In what follows we will show that large enough values of m the smallest and largest eigenvalues of the autocorrelation matrix R are "approximately" equal to the minimal and maximal values of the power spectrum of the time series x_n.

Theorem. Let us denote by x and X, respectively, the smallest and largest values of the power spectrum of the time series x_n; and by $\lambda_{\min}$ and $\lambda_{\max}$ the extreme eigenvalues of the autocorrelation matrix $(r_{ij})_0^m$. Then

$$x \leqq \lambda_{\min} \leqq (1 + |\varepsilon_1|)^2 x + O\left(\frac{1}{m}\right) \tag{6}$$

$$X \geqq \lambda_{\max} \geqq (1 - |\varepsilon_2|)^2 X + O\left(\frac{1}{m}\right) \tag{7}$$

where ε_1, ε_2 are constants of small magnitude:

$$|\varepsilon_1| \leqq 0.09; \quad |\varepsilon_2| \leqq 0.09. \tag{8}$$

Proof. Let us first consider the smallest eigenvalue. Denoting by $X(z)$ the z-transform of the time-series x_n, the z-transform of its autocorrelation function will be $|X(z)|^2$ and—by

the inversion formula of z-transforms (KULHANEK 1976, p. 25)—the k-th value of the autocorrelation function is given by

$$r_k = \frac{1}{2\pi j} \int_{\Gamma} \frac{|X(z)|^2}{z} z^k dz, \tag{9}$$

where $j = \sqrt{-1}$ and the path of integration Γ should be taken counter-clock-wise along the unit circle.

As a particular case of Eq. (9), for $k=0$ and for an arbitrary finite z-polynomial

$$u_0 + u_1 z + \ldots + u_m z^m; \quad \sum_{i=0}^{m} u_i^2 = 1 \tag{10}$$

we have

$$r_0 = \sum_{i=0}^{m} u_i^2 = 1 = \frac{1}{2\pi j} \int_{\Gamma} \frac{\left| \sum_{k=0}^{m} u_k z^k \right|^2}{z} dz. \tag{11}$$

By writing out Eq. (9) for the index $(k-l)$, multiplying both sides by $u_k u_l$, and summing with respect to k, l from 0 to m, we obtain:

$$\sum_{k=0}^{m} \sum_{l=0}^{m} r_{k-l} u_k u_l = \frac{1}{2\pi j} \int_{\Gamma} \frac{|X(z)|^2}{z} \sum_{k=0}^{m} \sum_{l=0}^{m} z^k z^{-l} u_k u_l dz =$$

$$= \frac{1}{2\pi j} \int_{\Gamma} \frac{|X(z)|^2}{z} \cdot \left| \sum_{k=0}^{m} u_k z^k \right|^2 dz \geqq$$

$$\geqq \frac{x}{2\pi j} \int_{\Gamma} \frac{1}{z} \left| \sum_{k=0}^{m} u_k z^k \right|^2 dz = x, \tag{12}$$

where we have made use of Eq. (11) and of the fact, that along the unit circle

$$|X(z)|^2 \geqq \min_{|z|=1} |X(z)|^2 = x.$$

From inequality (12), on the strength of the minimal property (4) of the smallest eigenvalue,

$$x \leqq \lambda_{\min} \tag{13}$$

and, by a similar reasoning,

$$\lambda_{\max} \leqq X. \tag{14}$$

On the other hand, suppose that the minimal value of the power spectrum belongs to the frequency f_0. The energy ΔE corresponding to the spectral band $\left(f_0 - \frac{\Delta f}{2}, f_0 + \frac{\Delta f}{2}\right)$ is, for a small enough Δf:

$$\Delta E \approx x \cdot \Delta f. \qquad \text{(see Fig. 1).}$$

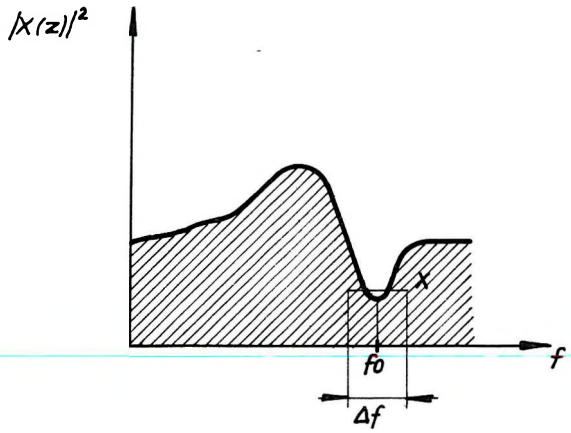

Fig. 1. Power spectrum of the time series x_n
1. ábra. Az x_n idősor teljesítményspektruma
Рис. 1. Спекрт сощности ряда времени X_y

By denoting the Fourier coefficient corresponding to the frequency f_0 by c, we have, by the Wiener-Khintschine theorem

$$|c|^2 = x$$

Let us now construct a digital convolution filter

$$\sigma_0, \sigma_1, \sigma_2, \ldots, \sigma_m$$

corresponding to the amplitude transfer function

$$|A(f)| = \begin{cases} \dfrac{1}{\sqrt{\Delta f}} & \text{if} \quad f_0 - \dfrac{\Delta f}{2} \leqq f \leqq f_0 + \dfrac{\Delta f}{2} \\ 0 & \text{otherwise} \end{cases}$$

(see Fig. 2.) Since, in the frequency domain, the total energy of filter $A(f)$ is 1, we have, by the over-all error estimations of MEYERHOFF (1968)

$$\sum_{i=0}^{m} \sigma_i^2 = 1 + O\left(\frac{1}{m}\right) \tag{15}$$

if m is sufficiently large.

The *actual* transfer factor of the digitally realized filter $(\sigma_0, \sigma_1, \ldots, \sigma_m)$ will be, for the frequency f_0:

$$\frac{1}{\sqrt{\Delta f}}(1 + \varepsilon_1),$$

where ε_1 is some small (less than 9%) overshoot or oscillation due to the Gibbs phenomenon.

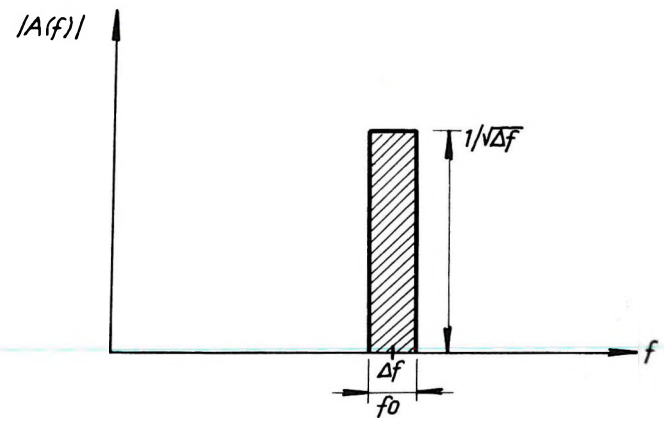

Fig. 2. Amplitude characteristics of the filter $A(f)$
2. ábra. Az $A(f)$ szűrő amplitúdó-karakterisztikája
Рис. 2. Характеристика амплитуд фильтра $A(f)$

By applying the filter to the time series x_n, the output energy will be

$$\Delta E_{\text{filt}} \approx \left[\frac{1}{\sqrt{\Delta f}}(1+\varepsilon_1)\right]^2 \cdot |c|^2 \cdot \Delta f + \mathrm{O}\left(\frac{1}{m}\right) = \\ = x(1+\varepsilon_1)^2 + \mathrm{O}\left(\frac{1}{m}\right) \tag{16}$$

On the other hand, by Eq. (3)

$$\Delta E_{\text{filt}} = \sum_{k=0}^{m} \sum_{l=0}^{m} r_{k-l}\sigma_k\sigma_l$$

i.e. by Eqs. (15), (16) and (4):

$$\lambda_{\min} \leqq x(1+|\varepsilon_1|)^2 + \mathrm{O}\left(\frac{1}{m}\right) \tag{17}$$

which, together with (13), proves statement (6). Inequality (7) can be similarly proved.

Finally, it should be noted that the distribution of the eigenvalues of the *infinite* matrix $T = (c_{\nu-\mu})$, where the indices ν and μ range from $-\infty$ to $+\infty$, has been first studied by TOEPLITZ (1911). Assuming that the Laurent series $\sum_{n=-\infty}^{\infty} c_n z^n$ is convergent in a ring $r_1 < |z| < r_2$ $(0 < r_1 < 1 < r_2)$ around the unit circle, Toeplitz proved that the set of these eigenvalues coincides with the set of the values the Laurent series assumes on the unit circle $|z| = 1$. The treatment of the asymptotic distribution of the eigenvalues of *finite* Toeplitz matrices requires rather deep mathematical techniques (GRENANDER and SZEGŐ, 1958; EKSTROM, 1973). The above, elementary proof of inequalities (6) and (7), based on digital filtering theory, seems to be new.

REFERENCES

BECKENBACH, E. F.–BELLMAN, R., 1961: Inequalities. Springer, Berlin–Göttingen–Heidelberg

BELLMAN, R., 1960: Introduction to Matrix Analysis. McGraw-Hill Book Co., New York

EKSTROM, M. P., 1973: A spectral characterization of the ill-conditioning in numerical deconvolution. IEEE Trans. Audio Electroacoustics AU–21, No. 4

GRENANDER, U.–SZEGÖ, G., 1958: Toeplitz Forms and their Applications. Univ. of Calif. Press, Berkeley and Los Angeles

KULHANEK, O., 1976: Introduction to Digital Filtering in Geophysics. Elsevier Publ. Co., Amsterdam–Oxford–New York

MEYERHOFF, H. J., 1968: Realization of sharp cut-off frequency characteristics on digital computers. Part III. Geoph. Prosp. Vol. XVI. No. 4

TOEPLITZ, O., 1911: Zur Theorie der quadratischen und bilinearischen Formen von unendlich vielen Veränderlichen. I. Teil: Theorie der L–Formen. Math. Annalen, Vol. 70. pp. 351–376

TREITEL, S.–WANG, R. J., 1976: The determination of digital Wiener filters from an ill-conditioned system of normal equations. Geoph. Prosp. Vol. XXIV. No. 2

WESTLAKE, J. R., 1968: A Handbook of Numerical Inversion and Solution of Linear Equations. John Wiley and Sons, Inc. New York–London

KORVIN GÁBOR

MEGJEGYZÉSEK TREITEL ÉS WANG EGY PROBLÉMÁJÁRÓL

TREITEL és WANG 1976-os dolgozatukban megmutatták, hogy a dekonvolúciós szűrő tervezéséhez használt autokorrelációs mátrix esetenként gyengén kondicionált, olyannyira, hogy a feladat megoldása különböző számítógépeken lényegesen eltérő szűrőket eredményez.

A kondíciószám mérésére a

$$P = \frac{|\lambda_{\max}|}{|\lambda_{\min}|}$$

mennyiséget használják. Felvetik a kérdést, mi lehet az autokorrelációs mátrixok gyengén kondicionáltságának geológiai-geofizikai magyarázata.

A dolgozatban, a digitális szűrőelmélet módszereivel bebizonyítom, hogy a P kondíciószámnak egyszerű értelmezés adható: körülbelül megegyezik a szeizmikus csatorna teljesítményspektruma legnagyobb és legkisebb értékének hányadosával.

Pontosabban, legyen $\lambda_{\min}$ és $\lambda_{\max}$ az $(r_{i-j})_0^m$ autokorrelációs mátrix legkisebb, ill. legnagyobb sajátértéke, x és X a teljesítményspektrum legkisebb, ill. legnagyobb értéke. Ekkor, ha m elég nagy

$$x \leqq \lambda_{\min} \leqq (1+|\varepsilon_1|)^2 x + \mathrm{O}\left(\frac{1}{m}\right);$$

$$X \geqq \lambda_{\max} \geqq (1-|\varepsilon_2|)^2 X + \mathrm{O}\left(\frac{1}{m}\right),$$

ahol ε_1 és ε_2 kis abszolútértékű konstansok ($|\varepsilon_1| \leqq 0{,}09$; $|\varepsilon_2| \leqq 0{,}09$).

Г. КОРВИН

ЗАМЕЧАНИЯ К ОДНОЙ ИЗ ПРОБЛЕМ ТРЕИТЕЛЯ И ВАНГА

В своей работе от 1976 г. Треител и Ванг показали, что в отдельных случаях матрица автокорреляции, используемая для проектирования фильтра обратной свертки, слабо кондиционирована, так что при решении задачи на различных ЭВМ, получаются существенно различающиеся между собой фильтры.

Для определения числа кондиционирования применяется соотношение

$$P = \frac{|\lambda_{\text{макс}}|}{|\lambda_{\text{мин}}|}.$$

Ставится вопрос, в чем заключается геолого-геофизическое объяснение слабой кондиционированности автокорреляционных матриц.

В настоящей работе, исходя из теории цифровых фильтров показано, что числа кондиционирования P можно придать простое истолкование: оно приблизительно совпадает с отношением макцимальной и минимальной величин спектра мощности сейсмического канала.

Точнее, пусть будут $\lambda_{\text{мин}}$ и $\lambda_{\text{макс}}$ наименьшая и наибольшая собственные величины автокорреляционной матрицы, а x и X – наименьшая и наибольшая величины спектра мощности, соответственно. Тогда, при довольно высоком значении m:

$$x \leqq \lambda_{\text{мин}} \leqq (1+|\varepsilon_1|)^2 x + 0\left(\frac{1}{m}\right);$$
$$X \geqq \lambda_{\text{макс}} \geqq (1-|\varepsilon_2|)^2 X + 0\left(\frac{1}{m}\right),$$

где ε_1 и ε_2 – постоянные с низкой абсолютной величиной ($|\varepsilon_1| \leqq 0{,}09$; $|\varepsilon_2| \leqq 0{,}09$).

Magyar Állami Eötvös Loránd Geofizikai Intézet
GEOFIZIKAI KÖZLEMÉNYEK
25

MEASUREMENT AND INTERPRETATION OF THE DYNAMIC CHARACTERISTICS OF INDUCED POLARIZATION DECAY CURVES*

A. ERKEL–P. SIMON–L. VERŐ**

1. The time function of the induced polarization decay curves

The majority of IP measurements, at present, provide only the variation of one, instrument-dependent parameter along profiles or on contour maps. The parameters are different in time domain and frequency domain measurements but even within these two techniques there are several parameters of quite different definitions. The definitions are mainly based on instrumental parameters because of lack of exact theory.

To meet the increasing requirements in induced polarization measurements, other quantities, possibly independent of the measuring technique, are to be determined. This requires in time domain to know the time function, that is, the dynamic characteristics of the decay.

As early as in 1959, WAIT described the time function as

$$\frac{e(t)}{E_0} \approx \sum_{n=1,\,2,\,3} A_n \exp(-\alpha_n t). \tag{1}$$

In 1962 Roussel processed his laboratory measurements on the basis of a similar assumption. For HUNTEC's M–3 type instruments HUTCHINS (1971) suggests the approximation with exponentials as a processing method. KELLER (1967) determines the time constants with density function instead of discrete exponentials:

$$E(t) = E_0 \int_0^\infty G(u) e^{-ut}\, du. \tag{2}$$

An even more complicated relation was found by DAMASKIN and SHEINMANN (private information, 1976)

$$F(T) = 1 - \exp(x \operatorname{erfc} \sqrt{x}),$$
$$x = \frac{T}{T_0 \sqrt{\pi}} \tag{3}$$

but the form of the function is also exponential.

DANKHÁZI (1973) provides the function for a very simple, elementary model:

$$\Phi(r, t) = \frac{I \varrho_0 \varkappa}{4\pi r \varepsilon} e^{-\frac{t}{\varrho_0 \varkappa}} \tag{4}$$

* Presented at the 39th EAEG Meeting, 1977. Zagreb
** Hungarian Geophysical Institute 'Roland Eötvös', Budapest
Manuscript received 17. 1. 1978

Both theoretically and empirically it seems to have been proved that the induced polarization decay curve can be approximated with sufficient accuracy by the sum of exponential factors. This alone does not provide further information on the basis of physical-chemical principles, neither does it contain any restrictions, it is purely a mathematical approximation of the recorded curve shape.

2. First step of factoring

In our processing method we also started from this approximation using the well-known factoring:

$$U_{IP}(t) = \sum_{i=1}^{n} A_i \exp(-t/\tau_i) + \text{corr}, \tag{5}$$

where

$U_{IP}(t)$	complex decay function;
i	serial number of exponentials;
A_i	coefficient of the ith exponential;
τ_i	time constant of the ith exponential;
t	time after the current is turned off;
corr	sum of supposed non-exponential components.

In the course of processing with different methods of the several hundred analogue field curves recorded under different geological conditions, it was found that n in Eq. (5) in most of the cases is 3, and the τ values are in the order of 10^{-1}, 1 and 10. Unfortunately the method of processing also affects the distribution of τ since factoring is only suitable for separating time constants in the ratio of about 5. The extreme values are restricted by the recording interval (0.2–80 sec in our case).

The first step in factoring is to eliminate the assumed non-exponential components. Not even a recording of 100 sec is enough for complete depolarization after long-time charging. The simplest procedure to eliminate this potential difference is to correct the complete decay curve with the potential difference obtained at the end of the measuring cycle. This method is applied for instruments operating with short charging and measuring times. The records show, and it is highly probable, that although the change of potential difference becomes very slow in time, it cannot be considered as constant. If, however, a potential value belonging to a given point in time is used for correction, an instrument-dependent parameter must be introduced, what we would like to avoid.

In the first processing method we assumed that the disturbing effects could be described in one measuring cycle with a function consisting of a remanent potential (U_R) and a linear member (dy). With the proper number of samples taken at equal intervals from the final portion of the decay curve, consisting of the component with the largest time constant and the above factors only, the linear and the constant components can also be determined from the following expressions:

$$dy = \frac{1}{\Delta t} \frac{(U_{s-5} - U_{s-4})(U_{s-1} - U_s) - (U_{s-3} - U_{s-2})^2}{2(U_{s-3} - U_{s-2}) - [(U_{s-5} - U_{s-4}) + (U_{s-1} - U_s)]}, \tag{6}$$

$$U_R = \frac{(U_{s-5}U_{s-3} - U_{s-4}^2) - dy^2 \Delta t^2 - dy(U_{s-5}t_{s-3} + U_{s-3}t_{s-5} - 2U_{s-4}t_{s-4})}{U_{s-5} + U_{s-3} - 2U_{s-4}}, \tag{7}$$

where

dy	linear component;
U_R	residual potential;
$U_s, \ldots, U_{s-5}$	last 6 samples;
$t_s, \ldots, t_{s-5}$	sampling times;
Δt	sampling interval.

The results of the numerous tests for determining the reliability of U_R and dy values show, that with one or two exceptions both U_R and dy are of the same sign in the records. That was not what we expected, as we had mainly reckoned with random effects, such as electrode polarization, telluric currents, instrument drift, SP compensation error etc. Besides, as it was systematic, it could be considered as a very slowly decreasing IP component rather than a correction.

The data necessary for determining U_R and dy were read off the record without any correction, namely, off the last portion of the curve with a poor signal to noise ratio. Therefore, scatter of the values determined on the basis of the same record was quite large but having recognized that their sign was always the same, we changed over to another method of determination. A tangent straight could be drawn to the last portion of the decay curve either by graphical adjustment in a linear time scale or by another smoothing method. The records were processed with this latter method as well, and it was found that the value of the last component at the time $t=0$ was of highly random nature, but about at (extrapolated) 250 sec it descreased to zero. This corroborates our assumption that it is some long-time depolarization resulting from charging. Thus, it might as well be considered as an exponential component, since in a relatively short time interval an exponential of a large time constant can be well approximated with a linear function. If, in the above interval, the values of U_R and dy are available, the approximate values of the assumed exponential are easy to determine. At small values of t, however, the correction with an exponential of large time constant differs from the linear correction, but it is impossible to have the choice of the different methods of correction on theoretical basis. Even in practice, the result hardly differ from each other.

For the sake of uniform plotting the U_R and dy values were converted into exponential parameters A_0 and τ_0 and the amplitudes were normalized. Thus the function describing the complete decay curve is the following:

$$\sum_{i=0}^{3} W_i \exp(-t/\tau_i) \tag{8}$$

of which only the values of W_0 and τ_0 have been discussed so far. W means the amplitude normalized to the primary voltage.

3. Recording time and sampling rate

The next step is to choose the most suitable sampling rate. But this, unfortunately, depends on the data themselves, that is, on the time constants and amplitudes. So the two, probably most effective time series of sampling can be chosen with an assumed distribution of the time constants and amplitudes, consequently, they are inadequate for considerably different distributions.

For determining a component, two moments should be taken into consideration, which depend on the time constants:

t_{M_i} the moment up to which a component of a given time constant can be recorded reliably. If this limit is set at 5 per cent of the original amplitude, the value is:

$$t_{M_i} \sim 3\tau_i; \tag{9}$$

t_{m_i} the moment, when the amplitude of the component with the smaller time constant decreases to 1 per cent of that with the larger time constant in a two-component curve:

$$t_{m_i} = \frac{\tau_i \tau_{i+1}}{\tau_i - \tau_{i+1}} \left[\ln \left(100 \frac{W_{i+1}}{W_i} \right) \right]. \tag{10}$$

As a first approximation it can be assumed that the amplitudes are almost equal and the ratio of the time constants is about 5, in which case

$$t_{m_i} \sim 5.8\tau_{i+1} \sim 1.2\tau_i. \tag{11}$$

So the recording time of a two-component decay curve should be:

$$t_{M_i} - t_{m_i} \sim 2\tau_i. \tag{12}$$

One of the sampling methods is to sample at equal intervals in sections. The number of samples taken for determining the components is to be chosen so, that the data for the estimation of scatter due to the measuring errors, should be sufficient, on the one hand, and the difference between the successive samples should not be too small on the other hand, otherwise they would be obscured by noise.

With the supposed amplitude and time constant distribution these two conditions could be fulfilled if 10 samples were taken from each component, that is, if the sampling interval was

$$\Delta t_i \sim 0.2\tau_i. \tag{13}$$

At the same time, to determine U_R and dy as well, the time series of Fig. 1 was used for the sampling.

But in some cases is was found that too many samples fell on certain components and too few on others (see Fig. 2). To determine the fourth component we had only four samples. Moreover, during the processing by a programmable calculator, it often caused problems that these time series could not be specified with a simple mathematical formula.

In the other sampling method, the interval varied and the time series was easy to describe mathematically:

$$t_k = t_1 b^k, \tag{14}$$

in which t_1 time of the first sample,

b factor determining the sampling rate. By using the powers of 2

$$t_1 = 2^x \qquad b = 2^y. \tag{15}$$

If the recording time is 125 msec–64 sec, then $x = -3$, $y = 0.2$, $0 \leqq k \leqq 45$.

It is clear that the selection of x and y determines the time of the first sampling and the sampling rate. For instance with the above values the number of samples is 45, almost the same as it was in case of equal sampling intervals but their distribution is better, so the condition of determining all the components from nearly the same number of samples is easier to fulfil. Therefore this method of sampling, was selected for practical applications.

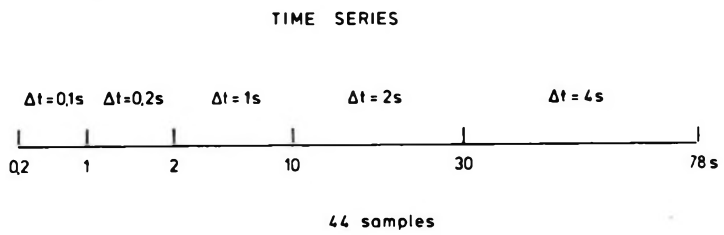

Fig. 1 Time series of sampling with different sampling rates

1. ábra. Változó mintavételi sűrűséget biztosító idősор

Рис. 1. Временный ряд, обеспечивающий переменную плотность выборок

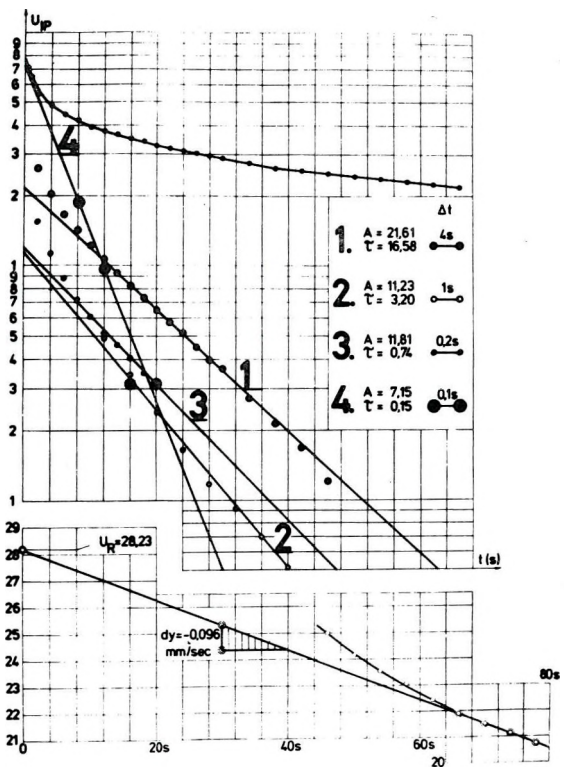

Fig. 2 Factoring of a four-component decay curve

2. ábra. Egy négykomponenses lecsengési görbe tényezőkre bontása

Рис. 2. Разложение четырехкомпонентных кривых затухания

4. Determination of the time constants and amplitudes

Field records as well as computed (synthetic) decay curves have been examined in order to find the most suitable method.

It requires relatively little calculation to determine the differences:

$$\Delta U(t_k) = U_k - U_{k-1}. \tag{16}$$

A_i and τ_i can be determined from the differential curve.

But methods independent of sampling have been found more efficient. From two subsequent samples a time constant can always be determined, what may be called apparent time constant—if the samples consist of the sum of more exponentials. Plotting these apparent time constants versus sampling time, a curve is obtained, the right-hand side asymptote of which provides the values of the largest time constant (τ_1 in Fig. 3). The asymptote can be determined by adjustment.

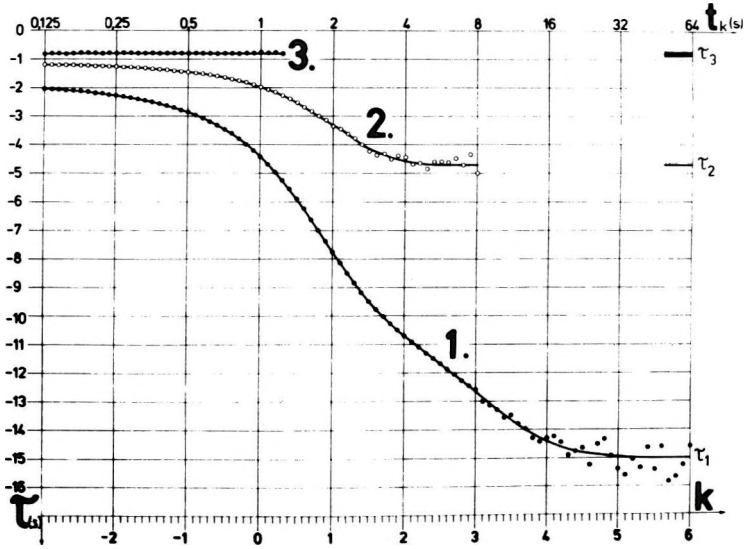

Fig. 3 Apparent time constant versus sampling time function of a three-component decay curve

3. ábra. Egy háromkomponenses lecsengési görbe látszólagos időállandó — mintavételi-idő függvénye

Рис. 3. Функция кажущихся постоянных времен и времени выборок для трехкомпонентных кривых затухания

A similar method can be used to obtain the amplitudes (Fig. 4). The formulas for time constants and amplitudes for the above two sampling methods are given below:

$$\tau_{app}(t_k) = \frac{\Delta t}{\ln\left(\frac{U_k}{U_{k+1}}\right)} \tag{17}$$

$$A_{app}(t_k) = \exp\left[\ln\sqrt{U_k U_{k+1}} + \frac{1}{\tau}\left(\frac{t_k + t_{k+1}}{2}\right)\right] \tag{18}$$

$$\tau_{app}(t_k) = \exp\left[(x+ky)\ln 2 - \ln\ln\frac{U_k}{U_{k+1}} + \ln(2^y - 1)\right] \tag{19}$$

$$A_{app}(t_k) = U_k\left(\frac{U_k}{U_{k+1}}\right)^{\frac{1}{2^y-1}} \tag{20}$$

Thus the values of A_1 and τ_1 can only be considered as approximate. The second approximation can be obtained by the following procedure:

First the approximate values of the first component for each sampling time are computed and these values are subtracted from the recorded decay curve. From the remainders—using the factoring—the approximate parameters of the second component are calculated. Subtracting the approximate value of the second component from the original samples, the data obtained contain only the first and the third components, which are more suitable for the exact determination of the first component. This multistep factoring is particularly necessary when the time constants are closer to each other than assumed and the time intervals suitable for their determination overlap one another.

In the majority of the cases it has been found that after having subtracted the third exponential member, what remains generally falls into the level of noise, thus making the determination of any further component impossible.

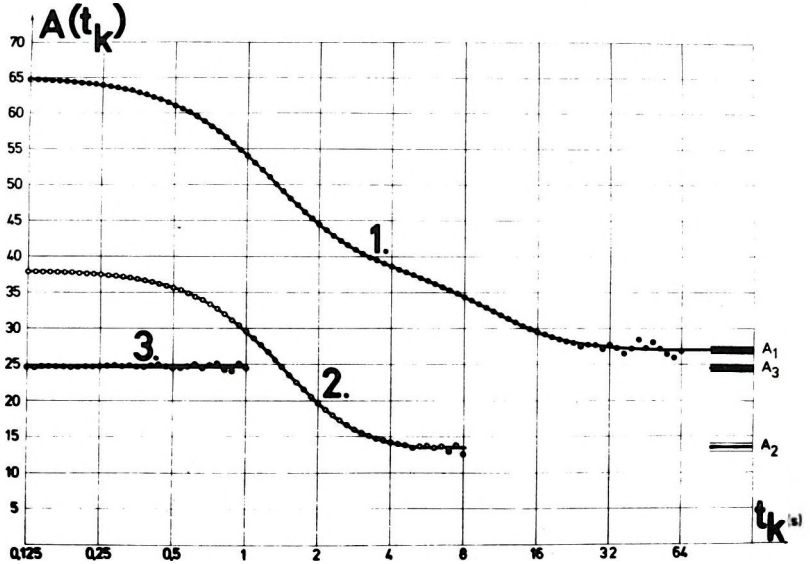

Fig. 4 Apparent amplitude versus sampling time function of a three-component decay curve

4. ábra. Egy háromkomponenses lecsengési görbe látszólagos amplitúdó — mintavételi-idő függvénye

Рис. 4. Функция кажущихся амплитуд и времени выборок для трехкомпонентной кривой затухания

5. The trend of development

A common feature of the new TD instruments (Huntec M–3, Scintrex IPR–8, Elliot R–10A, or the microprocessor controlled Soquem-Scintrex SWP–1, Z.E.R.O. IP–12) is their suitability for curve shape analysis. But the sudden improvement of the measuring technique is more important than the introduction of parameters supplying more information. It seems that in this field greater progress has been made in FD measurements (complex resistivity measurements, phase-angle—PFE correlation, correction methods), but at the same time it is also highly required to extend the frequency range of the measurements (ZONGE and WYNN, 1975; MILLER et al. 1975). In case of TD, an equivalent requirement is to examine the decay curve in the widest possible time range in order to have more components. More components give more $W_i - \tau_i$ pairs, and more data allow an easier detection of the differences and similarities between the dynamic characteristics connected to the different IP sources.

The coefficients obtained during processing are plotted in the form of $W_i - \tau_i$ diagrams. The normalized amplitude is the ordinate of linear scale and the time constant is the abscissa of logarithmic scale. As only the relative values of the secondary amplitudes are of interest, each amplitude is normalized to the sum of the secondary amplitudes. BERTIN and LOEB (1974) interpret their results of factoring in a similar way and consider the ratio of the amplitudes of exponentials as the most suitable for interpretation. In the diagrams the points defined by $W_i - \tau_i$ values have a physical meaning only, the connecting lines just indicate that they belong to the same measurement.

6. Field results

For practical applications first the necessary charging time was investigated. As shown in Fig. 5 the charging time (T_G) must be chosen so as to exceed the largest time constant of the survey area, otherwise U_R or A_0 calculated from it considerably depend on the charging time.

The curves of Fig. 6 have been obtained above mineralizations of different types. On measuring points Nb–10, Nb–7 and P–8 the host rock consists of young volcanic pyroclastics (mainly andesite), subvolcanic instrusions, lava beds and so on. On point Nb–10, disseminated high grade sulfides have been found in two depths (20–40 m, 148–180 m). In the vicinity of the ore formations, even further away, the pyrite content was predominant (>10 per cent). In bore-hole Nb–7 only disseminated pyrite of 0.5–10 per cent has been found. In the area of P–7 the pyrite content is 1–2 per cent on the average and is only enriched to 6 per cent in some sections. Pyrite occurs as disseminations and in veinlets. On point P–8 only sporadic, slight pyrite dissemination occurs (<1 per cent).

The $W-\tau$ diagrams show considerable differences. The P–8 curve is completely flat without extreme values. Nb–7 and P–7 are quite similar although the apparent chargeability anomalies are different. The amplitude of W_0—derived from U_R—is 2.5–3 times as large as that of the other. On point Nb–10 the amplitude of W_0 is about 5 times as large as that of the other components.

On sites Sz–3 and Y–6 the host rock consist of Mesozoic carbonaceous formations and dark-grey shales. No concrete data reffering to mineralization are available but it has been observed that in this area some of the IP anomalies result from ores, others from graphitic enrichment in the shale. These two latter curves considerably differ from the others both in form and extreme values.

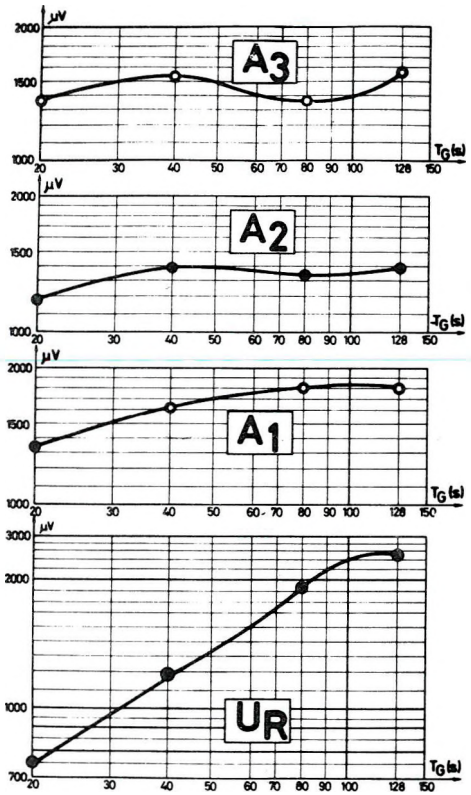

Fig. 5 Effect of charging time on amplitudes
5. ábra. A gerjesztési idő hatása az amplitúdókra
Рис. 5. Влияние времени возбуждения на амплитуды

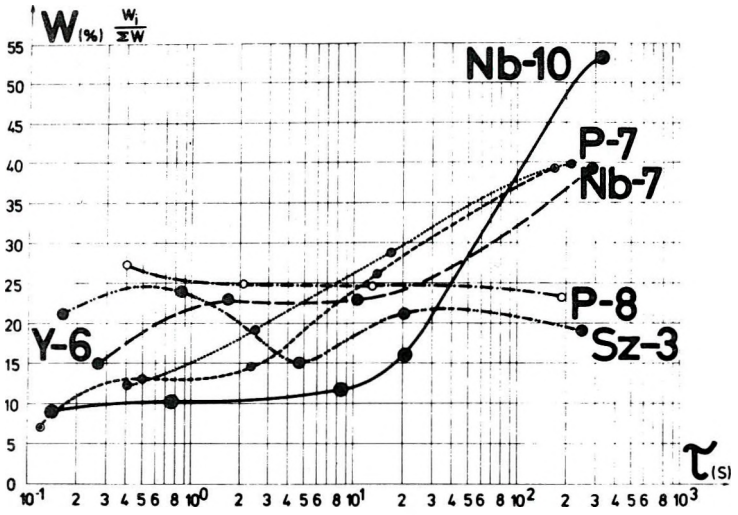

Fig. 6 $W-\tau$ curves obtained above mineralizations of different types
6. ábra. Különböző típusú ércesedések felett mért $W-\tau$ diagramok
Рис. 6. Графики $W-\tau$, полученные над различными типами оруденения

7. Equipments and development of new instruments

The results presented have been obtained with three different equipments: the bulk of the measurements was taken by an analogue recorder in the time interval of 0.2–80 sec, a few with two different types of DIAPIR time domain automatic digital potential, induced polarization and resistivity measuring instrument developed in the Hungarian Geophysical Institute 'Roland Eötvös'.

DIAPIR 4005 operates with the time series according to Eq. (14). For processing Eqs. (19) and (20) have been applied. DIAPIR 4010–N operates with three sampling intervals shown in Fig. 7, for processing Eqs. (6), (7), (17) and (18) have been applied. The apparent resistivity and polarizability values are measured automatically and the results appear on a three-digit display. To improve signal to noise ratio both in resistivity and in IP measurements different electronic solutions (summing, changing of the interval of integration) have been applied. For data processing programmable pocket-size scientific calculators have been used.

The paper has presented the results and shortcomings of the method for determining the dynamic characteristics of IP decay curves as well as the possibilities of improvement. The determination of $W-\tau$ diagrams involves considerable increase in the measuring and processing time and in the present instrument technique the depth of investigation is also limited. To increase efficiency the development of a new, sophisticated, multichannel digital equipment was just launched. At present the interpretation of the $W-\tau$ diagrams is performed empirically, with comparative methods. Since the values of amplitudes and time constants are affected in addition to the quality of ore by several factors, for example grain size, specific resistivity conditions, ore structure and so on, the methods can only be expected to solve some basic problems.

We are well aware that we have contributed to the method of curve shape analysis with only a few concepts so far and we are far from being able to tackle even the essential problems. We hope, however, to succeed in determining the most important data of the ore and the host rock with ground IP measurements and to solve the problems involved in increasing depth of penetration.

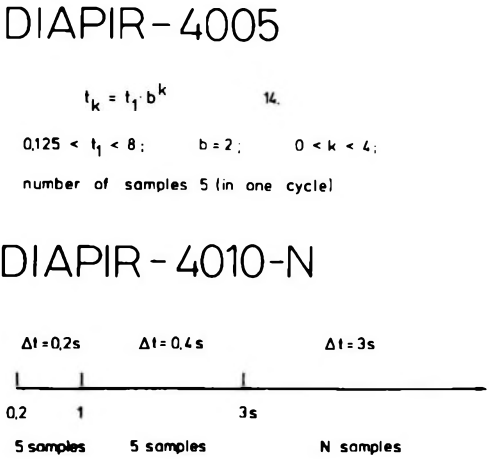

Fig. 7 Time series of DIAPIR equipments
7. ábra. A DIAPIR műszerek mintavételi idősora
Рис. 7. Серия времен выборок для аппаратуры типа ДИАПИР

REFERENCES

BERTIN, J.–LOEB, J., 1974: Traitement "à la main" sur ordinateur des transitoires en polarisation provoque. Geophysical Prospecting, Vol. XXII. No. 1.

DANKHÁZI, GY., 1973: Theoretical aspects of the induced polarization method. Geofizikai Közlemények, Vol. XXI. No. 1–4.

HUTCHINS, R. W., 1971: A new induced polarization instrument. Huntec publication

KELLER, G. V., 1967: Induced polarization well-logging. 8th Annual Logging Symposium. Transactions, SWPLA

MILLER, D.–CHAPMAN, W.–DUNSTER, D., 1975: Mark II—a multichannel IP system with minicomputer control and processing. SEG Annual Meeting

ROUSSEL, J., 1962: Etude sur modèles reduits des phenomènes de polarisation provoque. Annales de Géophysique, Vol. 18. No. 4.

ST. AMANT, M.–GAUCHER, E., 1978: A commercial IP receiver controlled by a microcomputer; the Soquem-Scintrex SWP–1. SEG Annual Meeting

WAIT, J. R., 1959: Overvoltage research and geophysical applications. Pergamon Press, London

ZONGE, K. L.–WYNN, J. C., 1975: Recent advances and applications in complex resistivity measurement. Geophysics, Vol. XL. No. 5.

ERKEL ANDRÁS–SIMON PÁL–VERŐ LÁSZLÓ

GERJESZTETT POTENCIÁL LECSENGÉSI GÖRBÉK DINAMIKUS JELLEMZŐINEK MÉRÉSE ÉS ÉRTELMEZÉSE

Feltevés szerint a gerjesztett potenciál lecsengési görbék jó közelítéssel leírhatók exponenciális tagok összegeként. A legegyszerűbb modellek esetén ez az exponenciális időfüggés elméletileg is igazolható. A terepen mért lecsengési görbék tényezőkre bontásával az exponenciálisok paraméterei meghatározhatók és ezen paraméterek segítségével különbséget lehet tenni érces és nem érces hatótól származó anomáliák között.

Az utóbbi években jelentek meg azok a műszerek, amelyek lehetővé tették a lecsengési görbék alakjának vizsgálatát, de ezek szinte kizárólag rövid gerjesztési és mérési idővel dolgoznak. Ugyanakkor a váltóáram GP-mérések értelmezésénél egyre inkább arra a következtetésre jutnak, hogy a frekvenciatartományt legalább néhány dekádnyira ki kell terjeszteni. Az egyenáramú méréseknél ezzel egyenértékű a lecsengési görbe minél szélesebb idő-intervallumban való vizsgálata. Csak így várható, hogy műszer-paraméterektől független adatokat kapunk.

Feldolgozási módszereinkkel az exponenciális tagok amplitúdóit és időállandóit határozzuk meg, a földtani értelmezést a normált amplitúdó—időállandó diagramok alapján kíséreljük meg. A feldolgozási módszerek megszabják a mintavételezés módját is. A műszerfejlesztésnél ezeket a szempontokat figyelembe vettük. Az így kialakított DIAPIR-műszercsalád alkalmas mind a cikkben ismertetett módszerhez szükséges adatok mérésére, mind a gyorsabb, de kevesebb információt adó hagyományos GP-mérésekre.

A mérési és feldolgozási tapasztalatok szerint ipari zajos területeken feltétlenül szükséges a digitális jelrögzítés és számítógépes feldolgozás. A műszerfejlesztés ebben az irányban is megindult.

А. ЭРКЕЛ–П. ШИМОН–Л. ВЕРЁ

ПОЛУЧЕНИЕ И ИНТЕРПРЕТАЦИЯ ДИНАМИЧЕСКИХ ХАРАКТЕРИСТИК КРИВЫХ ЗАТУХАНИЯ ВОЗБУЖДЕННОЙ ПОЛЯРИЗАЦИИ

Предполагается, что кривые затухания вызванной поляризации с хорошим приближением описываются как сумма экспоненциальных членов. Для простейших моделей такая экспоненциальная зависимость от времени теоретически подтверждается. При разложении наблюденных полевых кривых на факторы, можно определить параметры экспоненциальных членов, и при помощи этих параметров можно различать между собой аномалии, обусловленные рудными и нерудными возмущающими телами.

За последние годы появились приборы, позволяющие изучать форму кривых затухания, но они работают, почти без исключения, с короткими временами возбуждения и измерения. В то же время, при интерпретации данных метода ВП переменного тока, все чаще делается вывод о том, что диапазон частот необходимо расширить по крайне мере на несколько декад. При наблюдениях с постоянным током, это соответствует изучению кривой в как можно более широком интервале времен. Только таким образом можно ожидать получение данных, независимых от параметров прибора.

При помощи методов обработки данных определяются амплитуды и постоянные времени экспоненциальных членов, причем геологическая интерпретация осуществляется по палеткам нормированных амплитуд и постоянных времени. Методами обработки определяется также способ получения выборок. При разработке аппаратуры нами были учтены эти аспекты. Созданная таким образом серия аппаратуры типа ДИАПИР предназначена как для получения данных, необходимых для предлагаемого в настоящей работе метода, так и для проведения наблюдений по стандартному методу ВП, который оказывается хотя и более быстрым, но дает меньше информации.

Накопленный опыт проведения наблюдений и обработки данных показывает, что в районах с промышленными помехами необходимо проименять цифровую запись данных и обработку их на ЭВМ. Начаты работы по усовершенствованию аппаратуры и в этом направлении.

Magyar Állami Eötvös Loránd Geofizikai Intézet
GEOFIZIKAI KÖZLEMÉNYEK
25

METHODOLOGICAL BASIS OF A ϱ PROCESSOR FOR THE DIRECT DETERMINATION OF DENSITIES IN BORE-HOLES

L. ANDRÁSSY*

Introduction

In well-logging practice gamma-gamma logs are generally interpreted by using charts, graphically constructed from model measurements. To replace the rather time-consuming, tiresome manual interpretation procedure, there are two obvious possibilities:

1. Digitalisation of the logs, computer processing and automatic plotting of the resulting ϱ values,

2. Application of an analogue ϱ processor ensuring the direct registration of the density log.

The present paper is devoted to the basic theory underlying the construction of ϱ processors, including a mathematical approximation of the interpretation charts. Mud cake correction will also be approximated mathematically.

1. Basic Equation of the Two Detector Gamma-Gamma Method

The theoretical basis of the method is expressed by the equation describing the primary Compton scattering of gamma photons. We shall need two separate equations, for short and long probes:

$$N_s = K_s \varrho e^{-Q_s} \tag{1.1}$$

$$N_l = K_l \varrho e^{-Q_l}. \tag{1.2}$$

Taking the ratio of these equations we get

$$\frac{N_s}{N_l} = \frac{K_s}{K_l} e^{-(Q_s - Q_l)}, \tag{1.3}$$

which is the basic equation of the gamma-gamma method. In the above formulae:

N_s and N_l — counts of short and long probes, respectively;

K_s and K_l — constans depending on source strength N_0, solid angle $d\Omega$ and on the KLEIN–NISHINA–TAM differential scattering cross section $\sigma(\vartheta, \Phi)$;

* Hungarian Geophysical Institute 'Roland Eötvös', Budapest
Manuscript received 28. 6. 1978

Q_s and Q_l depend:
- on the path of the primary and scattered rays in the rock (x_{s_1}, x_{l_1} and x_{s_2}, x_{l_2}) (see Fig. 1);
- on the density (ϱ) of the rock;
- on the average mass absorption coefficient of the rock (μ_{m_1}; μ_{m_2});
- on the thickness and density of the mud cake (t_{mc}, ϱ_{mc});
- on the average mass absorption coefficient of the mud cake (μ_{mc_1}; μ_{mc_2}).

(Index *1* refers to the primary, index *2* to the scattered ray).

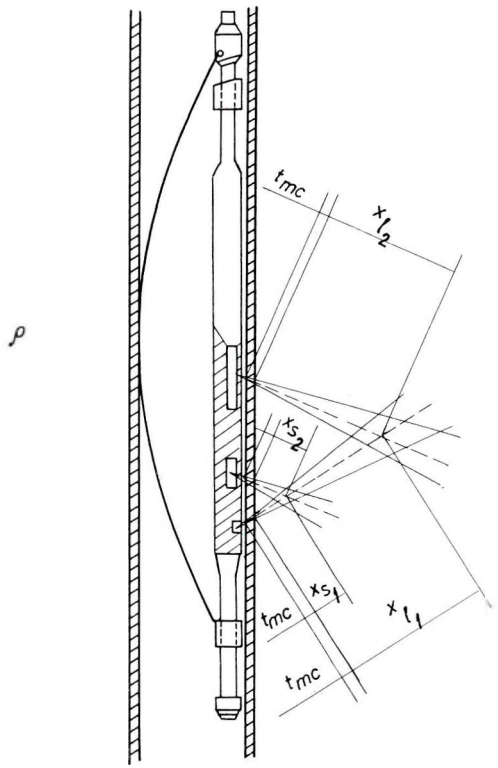

Fig. 1. Sketch of primary gamma scattering processes in bore-holes

1. ábra. A fúrólyukakban lejátszódó egyszeres gamma szórási folyamatok sematikus rajza

Рис. 1. Схематическое представление процессов однократного гамма-рассеяния, происходящих в скважинах

Let us write, in a general form,

$$Q = [(x_1 - t_{mc})\mu_{m_1} + (x_2 - t_{mc})\mu_{m_2}]\varrho + \\ + (\mu_{mc_1} + \mu_{mc_2})t_{mc}\varrho_{mc}. \tag{1.4}$$

In the absence of the mud cake Eq. (1.4) reduces to

$$Q = (x_1 \cdot \mu_{m_1} + x_2\mu_{m_2})\varrho. \tag{1.5}$$

Introducing

$$C = x_1\mu_{m_1} + x_2\mu_{m_2} \tag{1.6}$$

and using indices s and l to short and long probes respectively, we get:

$$-(Q_s - Q_l) = -(C_s - C_l)\varrho \tag{1.7}$$

i.e.

$$\frac{N_s}{N_l} = \frac{K_s}{K_l} e^{-(C_s - C_l)\varrho} \tag{1.8}$$

2. One-Variable Linear Regression for the Approximation of the Base Line of the Interpretation Chart

Figure 2 shows the interpretation chart for the KRGG–2–120–60sY type radioactive probe. The chart consists of two parts:

a) The "base line" and the branching lines for mud cake correction (central part); *b)* a nomogram for direct read-out of the ϱ values (on the right).

Individual points of the base line are determined by the values of counts (N_s and N_l) measured by the short and long probes, respectively normalized to water, and by the density values (ϱ).

Let us try to fit an empirical formula to the base line. We start out from the general equation

$$N = K\varrho e^{-C\varrho}, \tag{2.1}$$

where: N — registered counts;
ϱ — density of the rock;
K, C — appropriate constants.

Writing Eq. (2.1) for an arbitrary ϱ and for $\varrho = 1$ (water), and taking the logarithm of their quotient we obtain the equation of the base line:

$$Y = \ln x - c(x - 1) \tag{2.2}$$

with

$Y = \ln \dfrac{N}{N_w}$ — logarithm of the counts normalized to water.

Eq. 2.2 of course, cannot be used for direct regression because of the non-linearity of the function $\ln x$.

If, in a given interval (a, b) the function $\ln x$ is approximated by a straight line $\Phi(x) = Dx + \zeta$, D and ζ parameters can be determined by the least mean squares principles minimizing the integral

$$S = \int_a^b \{\ln x - (Dx + \zeta)\}^2 \, dx. \tag{2.3}$$

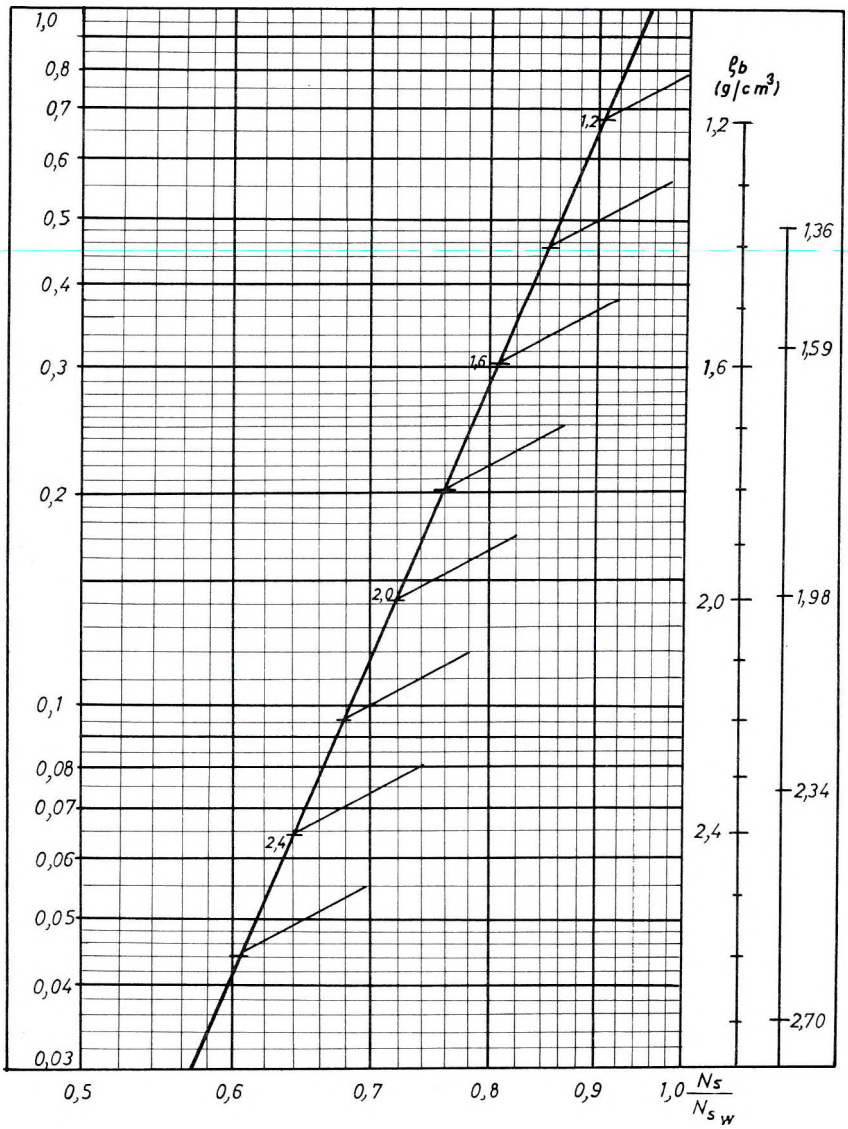

Fig. 2. Interpretation chart for the KRGG–2–120–60sY type radioactive logging equipment

2. ábra. KRGG–2–120–60sY típusú rádióaktív szonda kiértékelő diagramja

Рис. 2. Палетка для интерпретации данных, получаемых зондом РК типа KRGG–2–120–60sY

Substituting back the approximate relationship $\ln x \approx Dx+\zeta$ to Eq. (2.2) and regrouping the terms:

$$Y = \underbrace{(D-C)x}_{m} + \underbrace{(\zeta+C)}_{b} \tag{2.4}$$

we find that m and b can be obtained directly by linear regression. Indeed,

$$Y = \underbrace{\left(r\cdot\frac{S_y}{S_x}\right)x}_{m} + \underbrace{\left[\bar{Y}+\bar{x}r\frac{S_y}{S_x}\right]}_{b} \tag{2.5}$$

where:

$\bar{Y}$ and $\bar{x}$ are mean values of the dependent and independent variables;
S_y and S_x are the corresponding standard deviations;
r is the correlation coefficient.

Table I. contains the results of the linear regression for the KRGG–2–120–60sY probe. Calculations have been performed for two different diameters ($d_1 = 86$ mm and $d_2 = 214$ mm). The correlation coefficients obtained for the short and long probes show that there is a very strong connection between the values of counts normalized to water and the densities (ϱ). This, at the same time, proves the accuracy of the approximation of the base line, and the validity of the basic equation.

Table I

No.	$\varrho_i = x_i$	$d_1 = 86$ mm				$\varrho_i = x_i$	$d_2 = 214$ mm			
		$a_s = 13$ cm		$a_1 = 38$ cm			$a_s = 13$ cm		$a_1 = 38$ cm	
		$\frac{N_s}{N_{s_w}}$	Y_{s_i}	$\frac{N_l}{N_{l_w}}$	Y_{l_i}		$\frac{N_s}{N_{s_w}}$	Y_{s_i}	$\frac{N_l}{N_{l_w}}$	Y_{l_i}
1	1.00	1.0000	0.0000	1.0000	0.0000	1.0000	1.0000	0.0000	1.0000	0.0000
2	1.36	0.8485	−0.1642	0.4849	−0.7238	1.46	0.8989	−0.1086	0.4188	−0.8704
3	1.59	0.7839	−0.2435	0.3249	−1.1242	2.15	0.7633	−0.2701	0.1322	−2.0234
4	1.98	0.7558	−0.2799	0.1432	−1.9435	2.34	0.7576	−0.2776	0.1071	−2.2340
5	2.34	0.6580	−0.4186	0.0736	−2.6091	2.50	0.7010	−0.3552	0.0750	−2.5903
6	2.70	0.5896	−0.5283	0.0353	−3.3439	2.70	0.6253	−0.4695	0.0545	−2.9095
Mean value	1.8283		−0.2724		−1.6241	2.0233		−0.2465		−1.7713
S.D.	0.6336		0.1864		1.2432	0.6568		0.1693		1.1129
r			−0.9747		−0.9998			−0.9807		−0.9991
m			−0.2872		−1.9627			−0.2524		−1.6894
b			0.2538		1.9632			0.2645		1.6498

Finally, writing Eq. (2.4) obtained by linear regression for both short and long probes

$$Y_s = m_s x + b_s, \tag{2.6}$$

$$Y_l = m_l x + b_l \tag{2.7}$$

the equation of the base line will be:

$$Y_s - Y_l = (m_s - m_l)x + (b_s - b_l) \tag{2.8}$$

or with the original notations:

$$\ln \frac{N_s}{N_{s_w}} - \ln \frac{N_l}{N_{l_w}} = (m_s - m_l)\varrho + (b_s - b_l). \tag{2.9}$$

3.An Approximate Mathematical Solution for Mud-Cake Correction

One among the factors influencing gamma-gamma measurements in bore-holes is the presence of mud-cake. As an effect of mud-cake, points to be interpreted do not lie exactly on the base line but somewhat displaced, upwards to the right, or downwards to the left. (This latter case occurs for mud-cakes of high density).

In what follows we derive an approximate mathematical solution for the continuous determination of the mud-cake correction ($\Delta\varrho$). The basic ideas of the method can be understood from the sketch of Fig. 3.

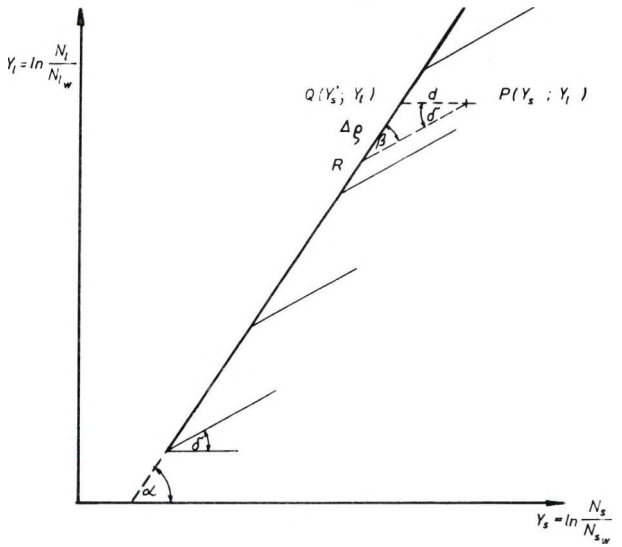

Fig. 3. Principle of the mathematical approximation of continuous mud-cake correction

3. ábra. Szemléltető rajz a folyamatos iszaplepény-korrekció közelítő matematikai módszerének megértéséhez

Рис. 3. Схема для иллюстрации приближенного математического метода непрерывного ввода поправок за глинистую корку

Consider the triangle PQR. By the sine theorem the mud-cake correction ($\Delta\varrho$) is given by

$$\Delta\varrho = d\frac{\sin\delta}{\sin\beta}, \tag{3.1}$$

where

$$d = Y_s - Y_s',$$
$$\beta = \alpha - \delta. \tag{3.2}$$

The sign of the correction $\Delta\varrho$ is either positive or negative, depending on whether the measured point ϱ lies on the right-hand side ($Y_s > Y_s'$) or left-hand side ($Y_s - Y_s'$) of the base line.

Of course, this approximation has definite limitations. If the measured point happens to be too far off the base line ($t_{mc} > 1 - 1{,}5$ cm) we are not justified by projecting it back along a straight line. In such cases approximations based on higher-order polynomials should be certainly better. This, however, is outside the scope of an analogue ϱ processor, because of the complicated circuitry required. Problems of this kind should be dealt with digital processing.

4. Methodological principles for constructing a ϱ Processor

The mathematical formulae derived in previous sections are simple enough to be realized by an analogue circuitry. The main task of this instrument is to register a continuous apparent density (ϱ_{app}) curve and mud-cake correction ($\Delta\varrho$) curve. Real density values are the sum of these curves:

$$\varrho = \varrho_{app} \pm \Delta\varrho. \tag{4.1}$$

Equation (4.1) is, methodologically, the basic equation of the ϱ processor.

By substituting $x = \varrho_{app}$ into Eq. (2.7), and making some rearrangements:

$$\varrho_{app} = m_l^* Y_l + b_l^*, \tag{4.2}$$

where

$$m_l^* = \frac{1}{m_l}; \qquad b_l^* = -\frac{b_l}{m_l}.$$

The parameters m_l and b_l have to be determined by linear regression.

Mud-cake correction is computed by Eq. (3.1). The angles δ and β can be determined from the interpretation charts. The value of d comes from Eq. (3.2), Y_s' term can be determined by putting Y_l = const. into Eq. (2.8), i.e.:

$$Y_s' = M\varrho + B + Y_{l\text{const}}, \tag{4.3}$$

where

$$M = m_s - m_l,$$
$$B = b_s - b_l.$$

From Eq. (4.3):

$$d = Y_s - (M\varrho + B + Y_{l\text{const}}). \tag{4.4}$$

Introducing the notation

$$K = \frac{\sin \delta}{\sin \beta}.$$

Eqs. (4.2)–(4.3) together yield the basic equation of the ϱ processor:

$$\varrho_{\text{real}} = (m_l^* Y_l + b_l^*) + K\{Y_s - [(M\varrho_{\text{app}} + B) + Y_l]\}. \tag{4.5}$$

In the absence of mud-cake Y_s, $\Delta g = 0$, i.e. the counts measured by the long probe yield real density values.

5. Field Experiments with the KRGG–2–120–60sY type Probe and ACD–75 Type ϱ Processor

The aim of these experiments was to record continous density logs in situ, to check the reliability and limitations of the ϱ processor. Two wells: Cs–220 (Csordakút) and Na–221 (Nagyegyháza), were used for the experiments.

In well Cs–220 continuous density logging was performed from 120 to 172 m, logging repeated between 120–150 m for statistical reliability checks.

For statistical analysis 24 corresponding ϱ samples were used from each log and their deviations were classified into four intervals.

The percentage distribution of deviations is given in Table II.

Table II

Deviation intervals (g/cm^3)	No. of samples	%
0.00–0.05	18	75
0.05–0.07	5	21
0.07–0.1	0	0
greater than 0.1	1	4

As Table II shows, 75% of the deviations are within the accuracy limit of density determination.

In well Na–221 gamma-gamma and continous density logs were taken between 24–100 m, with repeated measurement from 25 to 75 m. Logs are presented in Fig. 4. The density values obtained by the ϱ processor were compared to those calculated manually using the chart of Fig. 2, for altogether 18 layers (Table III). It can be stated that—except for a few samples—there is a fair agreement between the two sets of ϱ values.

As already mentioned, the distance (d) of the measured point off the base line sets a natural limit to the accuracy of the ϱ values determined by the ϱ processor. In case of a high d value the projection along a straight line back to the base yields unrealistically high $\Delta\varrho$ correction. We realize that in such cases a projection along second—or higher—order curves would yield better results.

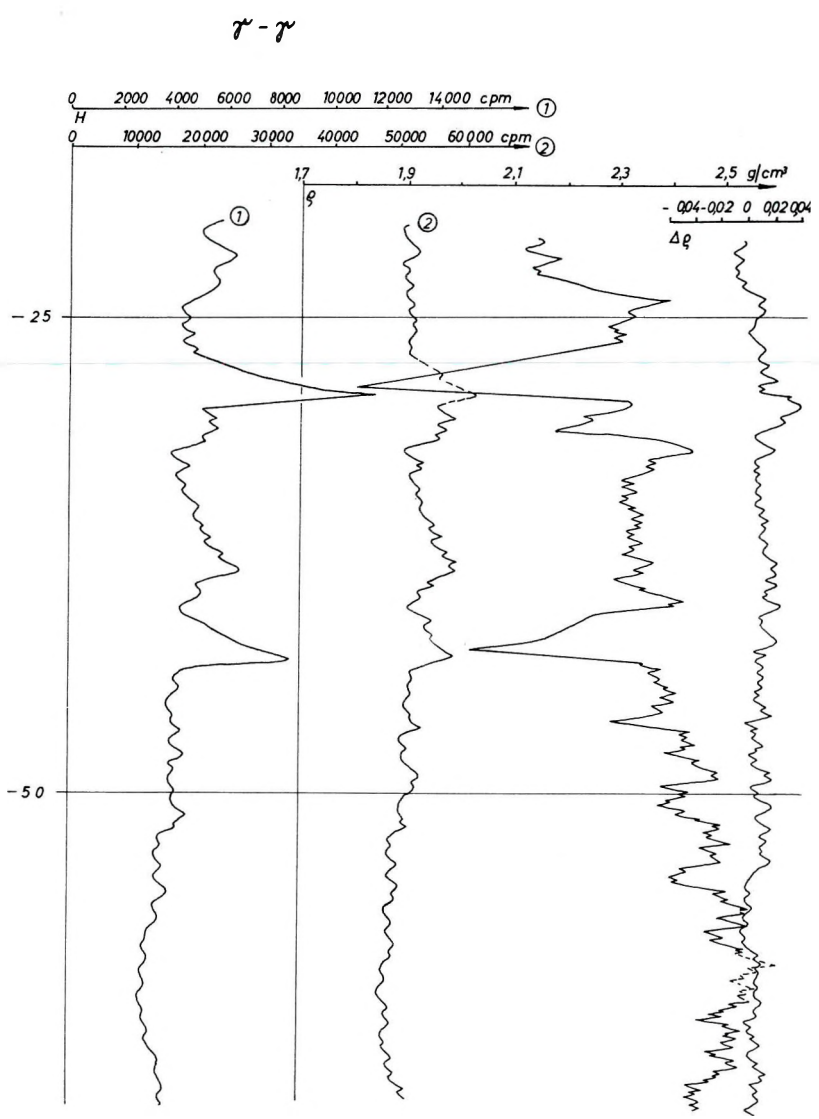

Fig. 4. Gamma-gamma logs, continuous density log (ϱ) and $\Delta\varrho$ log for the Na–221 bore-hole
1) long probe 2) short probe

4. ábra. Nagyegyháza–221 számú fúrásban felvett gamma-gamma, folyamatos sűrűség (ϱ) és $\Delta\varrho$ szelvények
1) hosszú csatorna; 2) rövid csatorna

Рис. 4. Кривые непрерывной плотности ГГК ϱ и кривые $\Delta\varrho$, полученные в скважине Надьэдьхаза–221
1 – длинный канал; 2 – короткий канал

In the next years, we should further refine the theoretical principles of the ϱ processor by developing the basic equation of primary scattering and introducing a correction term for secondary scattering effects. Theoretical calculations and model experiments will be performed to incorporate bore-hole diameter corrections into the basic equation of the ϱ processor. All these research works will be reported in forthcoming papers.

Table III

Probe type: KRGG–2–120–60 sY
Probe No: 7636
Isotope: Cs^{137} 14.9 mCi

Bore-hole Na–221.

N°	Depth [m]	$a_s = 13$ cm		$a_1 = 38$ cm			ACD–75 ϱ_b [g/cm³]	manual ϱ_b [g/cm³]
		N_s [cpm]	$\frac{N_s}{N_{s_w}}$	N_l [cpm]	$\pm\sigma_l$ [cpm]	$\frac{N_l}{N_{l_w}}$		
1	2	3	4	5	6	7	8	9
1	25.0	53 142	0.646	4 286	104	0.0701	2.34	2.33
2	26.0	51 429	0.625	4 429	105	0.0725	2.32	2.31
3	28.7	62 857	0.764	11 429	169	0.1871	1.86	1.80
4	29.5	57 143	0.695	5 000	112	0.0819	2.31	2.33
5	31.0	58 286	0.708	5 571	118	0.0912	2.23	2.19
6	32.0	53 142	0.646	3 857	98	0.0631	2.43	2.45
7	33.0	53 142	0.646	4 000	100	0.0655	2.37	2.37
8	35.0	54 286	0.660	4 857	110	0.0795	2.28	2.32
9	38.0	59 429	0.723	6 429	127	0.1053	2.20	2.37
10	40.0	52 571	0.639	4 286	104	0.0702	2.34	2.47
11	42.5	58 857	0.715	8 143	143	0.1330	2.03	2.04
12	45.0	52 000	0.632	3 857	98	0.0631	2.39	2.39
13	46.2	54 286	0.660	4 143	102	0.0678	2.39	2.28
14	48.0	51 429	0.625	4 286	104	0.0702	2.30	2.40
15	49.0	52 286	0.635	4 000	100	0.0655	2.38	2.50
16	54.5	48 571	0.591	3 429	93	0.0561	2.40	2.42
17	59.0	48 000	0.583	2 857	85	0.0468	2.53	2.60
18	62.0	48 000	0.589	2 786	83	0.0456	2.54	2.46

BIBLIOGRAPHY

HEARST, J. R.–CARLSON, R. C., 1969: The RIDS: a density logger for rough holes, GEOPHYSICS. Vol. XXXIV. No. 2.

WAHL, J. S.–TITTMAN, J.–JOHNSTONE, C. W.–ALGER, R. P., 1964: The Dual-Spacing Formation Density Log, Journal of Petr. Techn. Vol. XVI. pp. 1411–1416.

ANDRÁSSY LÁSZLÓ

"ϱ" PROCESSZOR MÓDSZERTANI ALAPJAI A TÉRFOGATSÚLYÉRTÉKEK FÚRÓLYUKBAN TÖRTÉNŐ KÖZVETLEN MEGHATÁROZÁSÁRA

A kétdetektoros gamma-gamma mérőrendszerek és a „ϱ" processzor együttes alkalmazása fúrólyukakban közvetlenül iszaplepényre korrigált valódi térfogatsúlygörbe mérését és analóg formában történő regisztrálását teszi lehetővé.

A gamma-fotonok Compton szórását leíró egyszeres szórás alapegyenletéből kiindulva meghatároztuk a kétdetektoros gamma-gamma eljárás alapegyenletét. Következésképpen az említett egyenletek ismeretében — iszaplepénymentes feltételekre — logaritmizálás és egyszerű matematikai műveletek elvégzése után lineáris regresszió segítségével meghatároztuk a bázis egyenes egyenletét. Bemutatjuk a KRGG–2–120–60 sY típusú kétdetektoros gamma-gamma mérőrendszer bázis egyenesének egyenletét.

A méréseket befolyásoló iszaplepénykorrekció kiszámítására egy közelítő matematikai megoldást mutatunk, amely segítségével iszaplepényre korrigált valódi térfogatsúlyértékek határozhatók meg. Az eljárás $t_{mc} = 1 - 1{,}5$ cm-nél kisebb iszaplepényvastagságokra alkalmazható. Cs–220 fúrás szelvényanyagából elemző feldolgozást végeztünk a térfogatsúlygörbe és ismétlésének összehasonlítására. A Na–221 fúrás szelvényanyagából elvégeztük a kiértékelő diagram segítségével kézi úton és ACD–75 processzorral kapott térfogatsúlyadatok összehasonlítását.

Л. АНДРАШИ

МЕТОДИЧЕСКИЕ ОСНОВЫ ПРОЦЕССОРА «ϱ» ДЛЯ ПРЯМОГО ОПРЕДЕЛЕНИЯ ВЕЛИЧИН ОБЪЕМНОГО ВЕСА В СКВАЖИНАХ

Совместное использование двухдетекторного зонда ГГК и процессора «ϱ» дает возможность получать и записывать в аналоговой форме кривые эффективного объемного веса, исправленные за глинистую корку непосредственно в скважинах.

Исходя из основного уравнения однократного рассеяния, описывающего комптоновское рассеяния гамма-фотонов, можно определить основное уравнение для метода двухдетекторного ГГК. Зная указанные уравнения, после логаритмирования и проведения простых математических процедур, для условий без глинистой корки – было определено уравнение основной прямой. В работе приводится уравнение основной прямой двухдетекторного зонда ГГК типа KRGG–2–120–60 sY.

Для вычисления поправок за глинистую корку, влияющую на результаты наблюдений, приводится приближенное математическое решение, позволяющее определить эффективные величины объемного веса, исправленные за глинистую корку. Данный метод может применяться при толщинах глинистой корки меньших $t_{mc} = 1 - 1{,}5$ cm.

Каротажные данные скважины Cs–220 были подвергнуты обработке и анализу для сопоставления кривой объемного веса с кривой повторных измерений. По каротажным данным скважины Na–221, с использованием палетки были сопоставлены данные об объемном весе, полученные в результате ручной интерпретации и обработки процессором типа ACD–75.

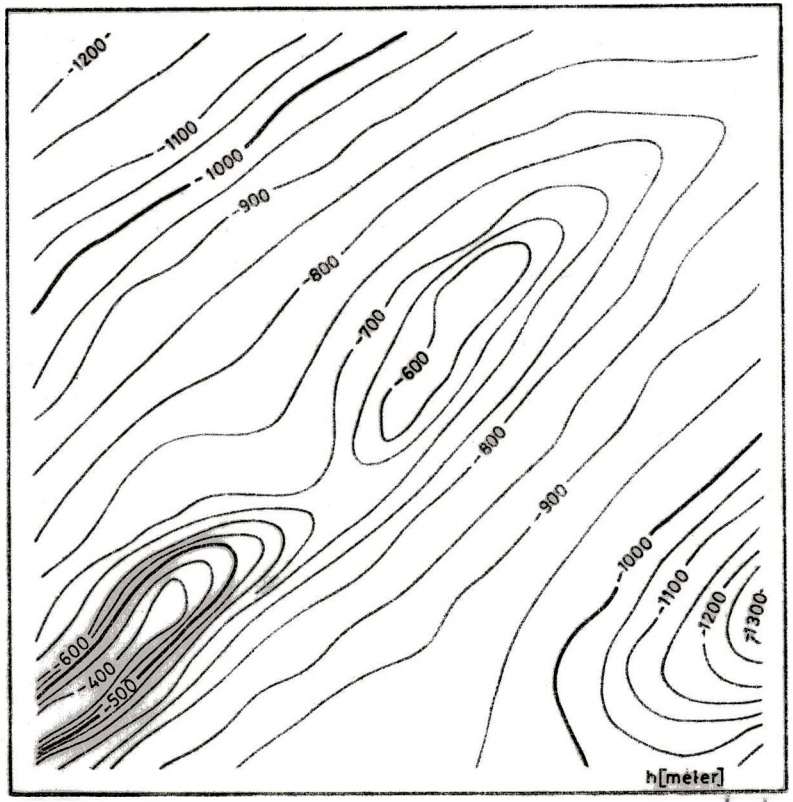
-1200-
-1100
-1000
-900
-800
-700
-600
-800
-900
-1000
-1100
-1200
-1300-
-600
-400
-500
h[meter]

4/1

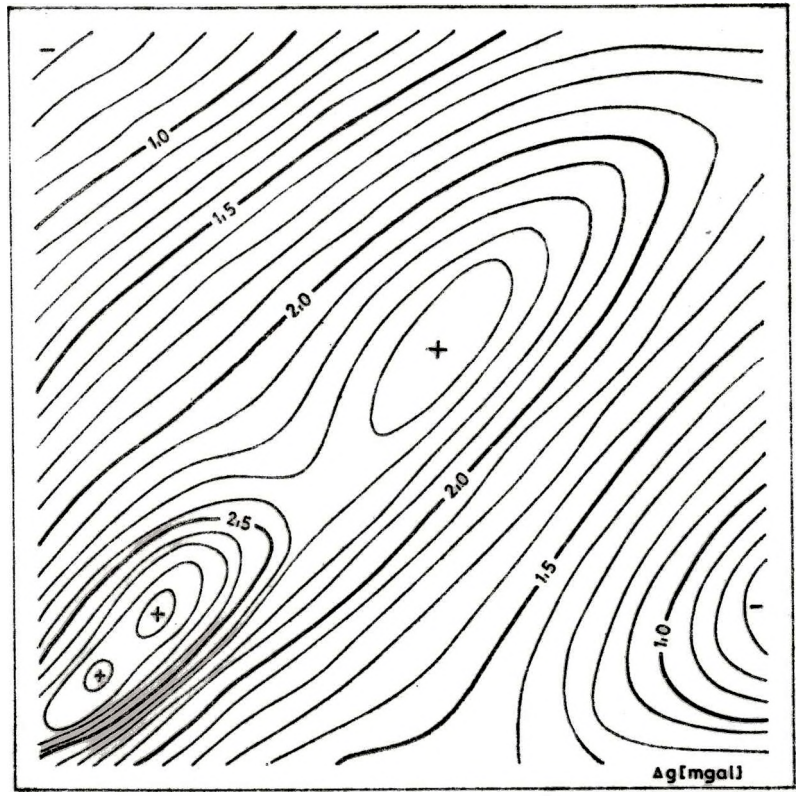
-
1,0
1,5
2,0
+
2,5
2,0
1,5
1,0
-
Δg[mgal]

4/2

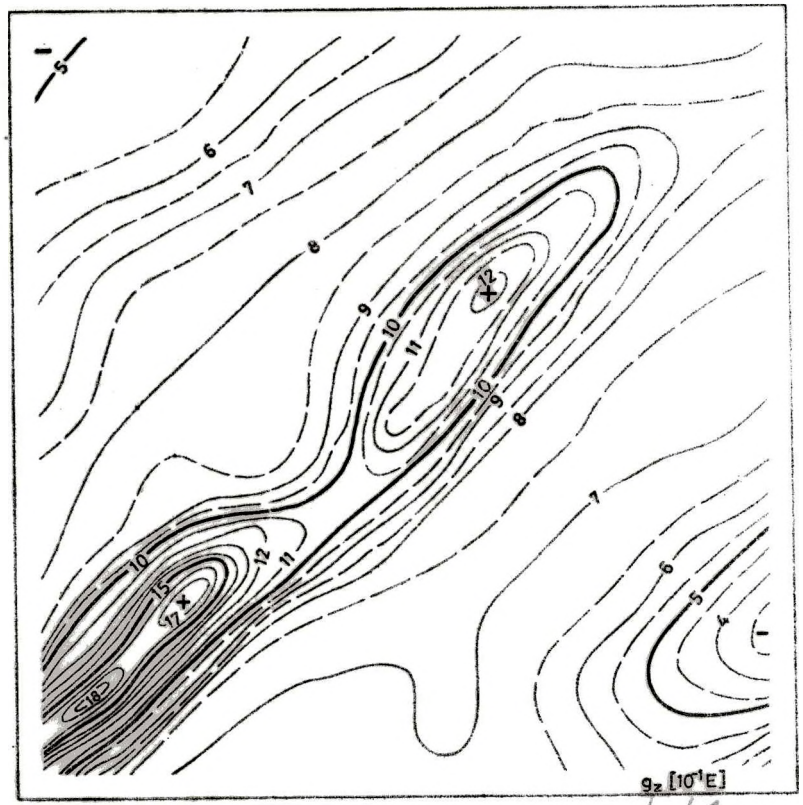

4/3

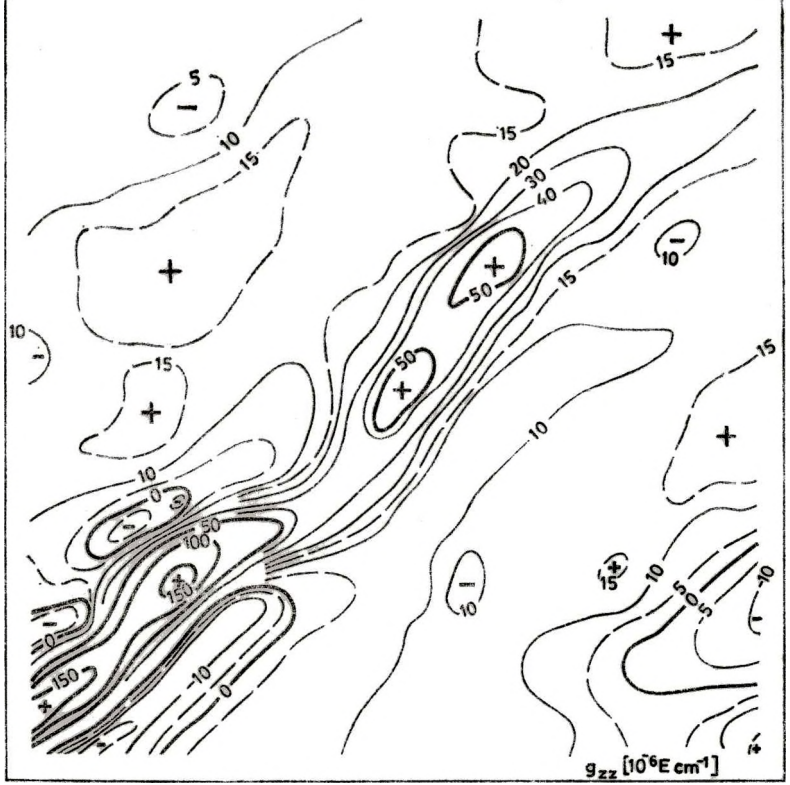

4/4


m(500, 3) [10⁻¹ mgal]

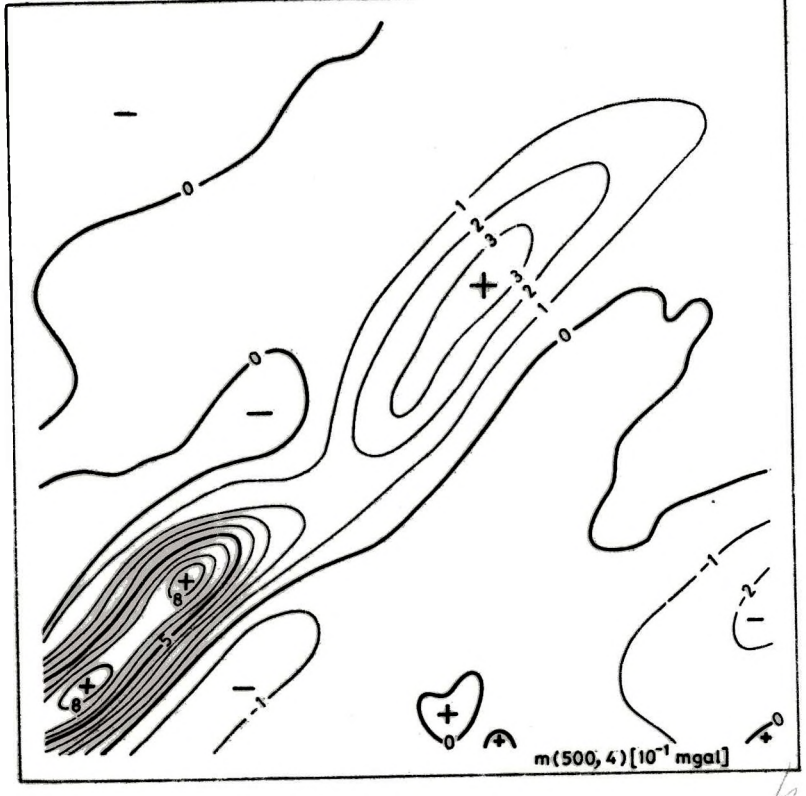
m(500, 4) [10⁻¹ mgal]

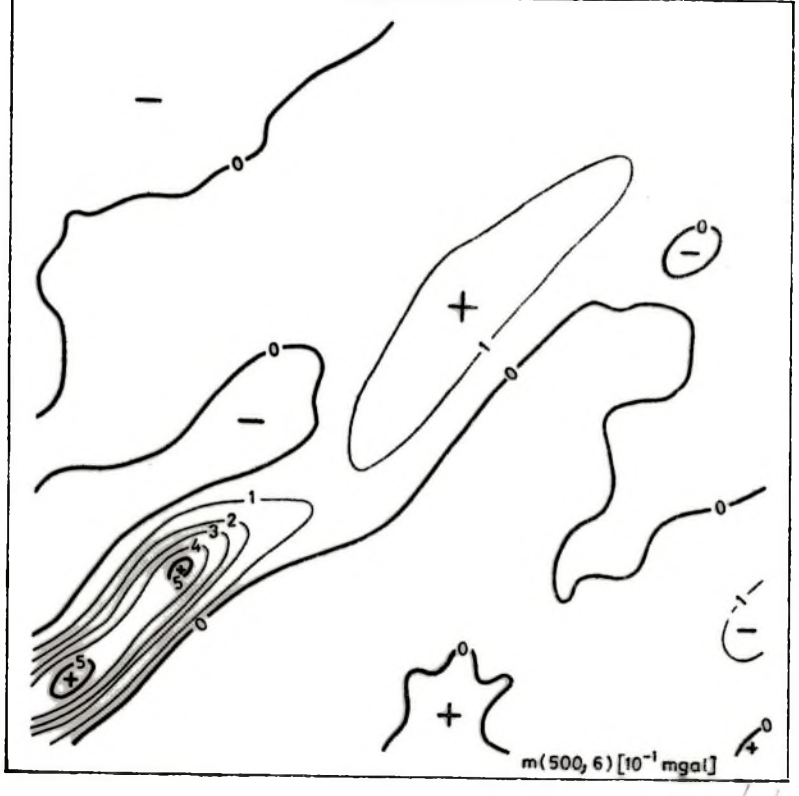

4/7

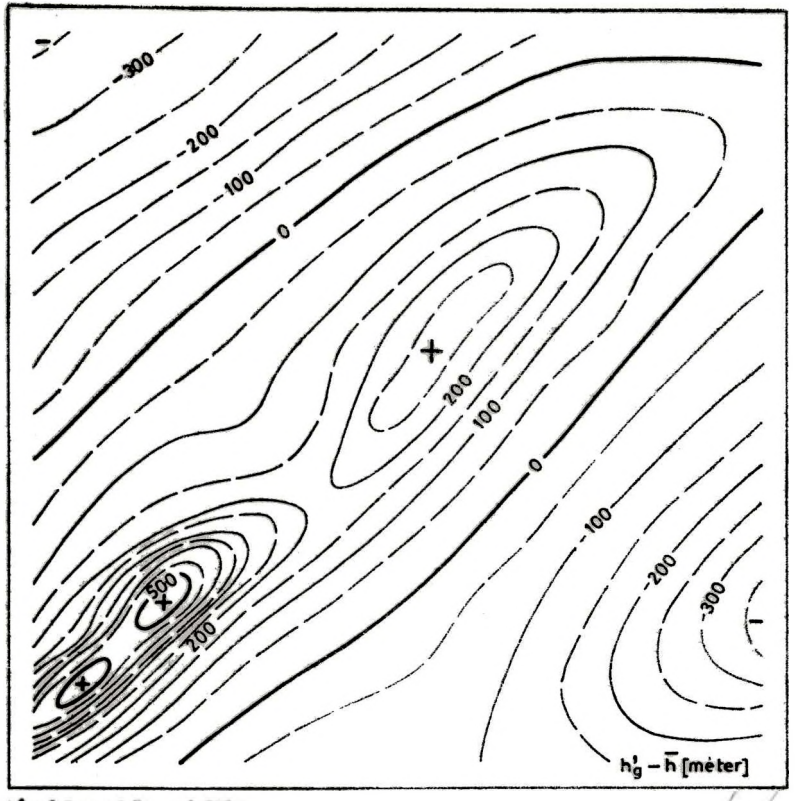

$h'_g = 2{,}5\Delta g + 1{,}7g_z + 0{,}019g_{zz}$.
$\bar{h} = -860$

4/8

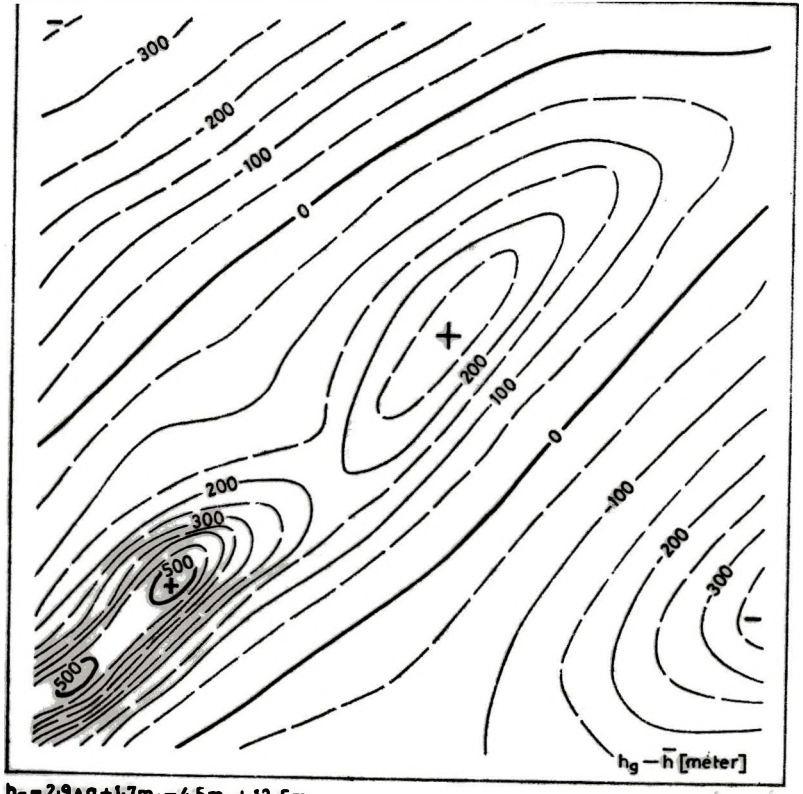

$h_g = 2.9\Delta g + 1.7m_3 - 4.5m_4 + 12.5m_6$

$\bar{h} = -860$

$\Delta h' = h_g' - h$

Δh = hd − h